Design and Development of Structures, Installation Tools, Installation Procedures, and Models for the Vertical Drift Detector of the Deep Underground Neutrino Experiment

By

Yannis Pandiscas

A thesis submitted in partial fulfillment of

the requirements for the degree of

Master of Science

Mechanical Engineering

at the

UNIVERSITY OF WISCONSIN-MADISON

2025

Date of final oral examination: 05/02/2025

The thesis is approved by the following members of the Master's Thesis Oral Committee:

Franklin K. Miller, Associate Professor, Mechanical Engineering

Gregory F. Nellis, Professor, Mechanical Engineering

Brian Rebel, Professor, Physics

ACKNOWLEDGEMENTS

I would like to thank my partner for her advice and support throughout my studies and research. I truly would not have been able to perform this work without her continued patience and support. Similarly, I would like to say thank you to my parents for supporting me throughout my education, even today. Words cannot describe the help, advice, and patience that they have displayed through this process despite having their own significant challenges.

I would like to thank all my colleagues within the Solar Energy Lab, both current and former, for their unending support, and for making me want to come to work every day. There is a small group that I would like to acknowledge specifically. First, Ian Jentz, your help throughout this project has been immeasurable in both quantity and quality, I would not have gotten half of this work without your help and advice. Joshua Truchon, who was the master's student on this project, and whom I worked for as an undergraduate, served as a mentor in his own right, and much of the work in chapter two was performed while he was still here at the SEL.

Last but not least I would like to thank all my committee members, Franklin Miller, Gregory Nellis and Brian Rebel. You three have been incredible mentors throughout my time on this project and more broadly at UW. I will never forget how welcoming and helpful you all were when I first started working on this project. You have all contributed significantly to my learning and this work.

Contents

LIST OF TABLES

LIST OF FIGURES:

ABSTRACT

The Deep Underground Neutrino Experiment's (DUNE) goal is to measure the oscillation of neutrinos between their three flavor states. The measurement is performed by generating, selecting, and measuring a known flavor of neutrinos using a particle accelerator and a near detector. The measurement is performed using electronic sensors submerged in liquid argon. The neutrinos will continue along their path until they enter the far detector, where they will be measured again. These measurements are conducted using devices known as Charge Readout Planes (CRP), which are housed within a cryostat measuring 16m x 15m x 66m, which is filled with liquid argon. These electronics will be installed within the cryostat once the construction of the cryostat is finished.

160 CRPs will comprise one of these detectors with 80 being suspended from the ceiling, and the remaining 80 will rest on the floor of the cryostat. This thesis focuses on these CRP on the floor. Installing and supporting these CRP is challenging due to the cryostat's construction. This thesis presents two ways that these CRP can be installed. The first section focuses on installing entire CRPs in the cryostat by constructing a temporary, moveable raised support structure for technicians to work underneath without the risk of the CRP falling. The structure was designed to be assembled in situ by a team of two people and then retrieved remotely. This thesis documents the design and validation process of the structure and retrieval system, including any custom components.

The DUNE Consortium was interested in the possibility of installing the bottom level of CRPs by breaking them into their two sub-assemblies called Charge Readout Units (CRU). As the structure for these devices was designed for the two to be joined, further design and analysis was required. This thesis shows the development and results of a Finite Element Model (FEM) which simulates the load cases that the CRU will experience when it is installed in the cryostat.

1. Background

1.1. Neutrino Mass

In 2015 Takaaki Kajita and Arthur B. McDonald received the Nobel Prize in Physics "for the discovery of neutrino oscillations, which shows that neutrinos have mass". [1] This discovery motivated scientists to design experiments to measure this oscillation of neutrinos between three flavor states; tau, muon, and electron states. One such experiment is the Deep Underground Neutrino Experiment (DUNE). The same measurement will be performed with antineutrinos to determine if there is a difference in oscillation behavior between neutrinos and anti-neutrinos. If the behavior is different enough for antineutrinos and neutrinos, it could explain the charge-parity violation observed in the universe.

1.2. DUNE

DUNE will use the Long Baseline Neutrino Facility (LBNF) particle accelerator at Fermi National Accelerator Laboratory (Fermilab) in Batavia, IL to generate neutrinos. The process of generating neutrinos begins with accelerating protons using PIP-II and a chain of other accelerators ending with LBNF at the laboratory, with protons exiting the chain with more than 120 billion electronvolts of energy. The protons are directed at a target made of pure graphite.

Upon interacting with this target, pions and kaons will be generated. Magnetic fields are then used to select desired energy levels and guide the particles towards Sanford Underground Research Facility (SURF). The selected pions and kaons then decay into neutrinos to be measured [2]. The neutrinos will continue along the same trajectory as the pions and kaons which created them due to the conservation of momentum and very small mass associated with neutrinos [3]. A near detector will be used to study the composition of the neutrino beam. This with the far detector can be used to measure the parameters that govern neutrino oscillations.

The far detector is located approximately 1300km away. The neutrinos will travel through the Earth due to their extremely small interaction cross-section. This distance has been selected along with the neutrino energies to ensure that oscillations occur between the near and far detectors. Once at the far detector, the neutrinos will interact with the liquid argon creating particles that can ionize individual argon atoms, allowing for measurement of the neutrino's energy and flavor [4], [5].

1.3. Detector

The far detector can be imagined as a combination of two enormous detectors, one vertical drift and one horizontal drift. The work detailed in this thesis specifically pertains to the vertical drift detector. The vertical drift detector itself is made up of two levels, one suspended from the roof of the cryostat, and the other located just above the membrane floor of the cryostat. The scope of work performed is further focused on this bottom layer of the vertical drift detector. Each layer of the detector is composed of 80 Charge Readout Planes (CRP). Which are electronic devices 3.4m in length and 3m in width, have printed circuit boards on 5 of the 6 faces, and whose structure is mostly comprised of woven glass-epoxy composites. Each CRP has an estimated mass of 255kg. For transport each of these CRP can be disassembled into two Charge Readout Units (CRU) about a centerline.

These two planes of CRP are going to be submerged in a bath of liquid argon, within a cryostat which measures 66 m in length by 16 m wide, and 16 m tall. The size and shape of the cryostat, and its surrounding superstructure has already been developed and the design considered fixed. Thus, this superstructure is a constraint for engineering problems regarding the installation and construction of this detector.

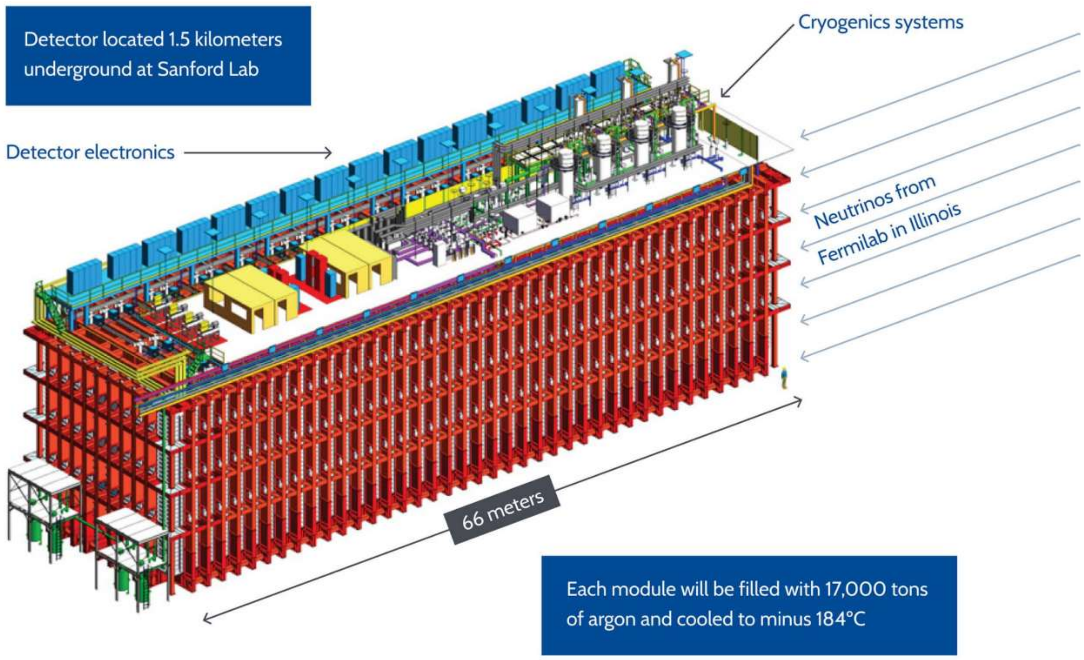

Figure 1: View of the Detector, the red beams make up the superstructure of the detector. [6]

Between the liquid argon and the superstructure exists a series of materials designed to insulate the argon so that heat leak from the outside is minimized. The very top layer of this stack, which any equipment within the detector will rest on, is a corrugated membrane of stainless steel. [6] The membrane is designed to manage the effects of thermal contraction as the cryostat cools from a temperature above 300K to the boiling point of liquid argon at 87K. The center to center spacing of each membrane section is designed to remain constant. The unique shape of the membrane creates challenges during installation of the detector. The task assigned to our research group is to determine a process to install the CRP and CRU within the detector, selecting or designing required equipment to complete the task.

Figure 2: Shape of one square section of cryostat membrane floor.

2. Installation of CRP in the Vertical Drift Detector

2.1. ProtoDUNE Installation

Before any CRPs are to be installed in the Vertical Drift Detector, a test of the CRP and supporting systems was performed at CERN. This process required the installation of four prototype CRPs, which provided an opportunity to develop and evaluate methods for installing a CRP in a low-stakes environment. The cryostat at CERN is like that of the detector at SURF, but it differs enough to necessitate unique design requirements.

2.1.1. ProtoDUNE Design Requirements

The design of the CRP requires that cables be connected to the underside of the device. Since the device is large, measuring 3.4 m by 3 m, and heavy, with a mass of 255 kg, it is considered unsafe to work underneath it without a static support structure to ensure stability. This support structure must be easy to install without damaging the membrane floor or generating metal particulates.

Due to the layout of the membrane floor, different cryostat locations require the CRP to be supported in different positions. The support structure must accommodate all these varying CRP hardpoint positions. Additionally, the edges of the CRP must be precisely aligned relative to one another in the vertical direction, with a tolerance of ±1 mm. To achieve this, the feet of the CRP are adjustable, and this adjustment must be performed while the CRP is supported by the structure. However, the deformation of the floor when under load must be accounted for. Therefore, the support structure must transmit the CRP's weight to the floor as rigidly as possible while allowing for precise alignment and leveling without requiring the CRP to be lifted off the structure.

The cryostat at CERN allows access to the CRP from all four edges, but the small entryway prevents the use of additional large equipment for setting up and retrieving the truss. Consequently, two additional design requirements emerge: the system must be modular, and each modular component must be lightweight enough to be moved by a single person. To minimize the risk of damage to the false floor, reduce setup time, and improve ergonomics, the modular connections must also be toolless.

Lastly, the design must be error-proof, ensuring that the components seamlessly assemble without the need for further adjustments when performed correctly. The joints must be designed so that they cannot be assembled incorrectly. Any misalignment or error during assembly should be immediately apparent to the user.

2.1.2. Modular Installation Truss Development and Testing

One of the key functions of the truss system is to aid in leveling the CRP by preloading the floor with the CRP's mass. This assumes that the weight of the CRP is enough to compress any non-uniformity in the membrane floor. To achieve this, the truss columns are positioned directly below the CRP's feet. The feet interface with the structure through a spring-loaded centering mechanism, which consists of a machined circular pocket and a corresponding plate that extends slightly above the column. The plate is slightly smaller than the pocket, allowing for controlled movement.

The centering mechanism ensures proper alignment by providing immediate feedback when the CRP is out of tolerance. If misaligned, the bottom plate tilts, indicating that one spring is compressing while the others remain at their free length. This system reliably aligns the CRP's center of mass with that of the installation truss in both the x and y directions.

This allows us to model the load as a vertical load on each of the columns which is exactly the mass of the CRP divided by the number of feet, which is four. Knowing that the mass of a CRP is 255 kg, and that there will also be cables attached to the CRP, the calculations use a designed load value on each column of 75 kg, which allows for there to be an extra 45 kg supported by the structure. The columns are linked together by spans of cross-members that increase the stability of the structure, making it more resistant to tipping.

Figure 3: Spring loaded centering mechanism guiding the foot of the CRP to rest on top of the truss.

With these requirements in mind, material selection for the columns can continue. Since the columns are the primary load-bearing members, a column was needed that could support 75 kg, while remaining lightweight, easy to modify for the modularity feature, capable of fitting within the membrane floor sections without interference and is readily available in several lengths to accommodate the various spans required by the membrane floor and CRP orientation.

Based on these requirements the ModTruss TR 6" Aluminum Truss series of products was selected. The product is a 6in-by-6in square of aluminum plates with a thickness of 0.125". Each 6in long section has a repeated hole pattern on all four vertical sides to allow a user to mechanically fasten items to the truss. In addition, each 6in section has a significant amount of material removed to reduce weight. This leads to a linear weight of approximately 3.90 lb./ft. This small size and lightweight makes each section easy to carry.

As part of the selection process, it was validated that the ModTruss sections would be capable of supporting the design load. The columns were assumed to carry all the load due to their location directly under the CRP feet. Knowing that the primary failure mode for a long slender member like the columns of the structure is buckling, the critical load needed to induce buckling in the 4-foot-long column was examined.

Buckling strength values are provided by ModTruss as 12,420 lbf at a length of 10 feet and using an effective length value of 1.0. [7] Buckling is analytically described by the Euler buckling equation which gives the critical load at which buckling occurs in a long slender column. The values in the equation are E, the material's modulus of elasticity, I the beam moment of inertia, L the length of the column, and K the effective length value which is a value which accounts for the boundary conditions at the end of the beam. [8]

$$\frac{\pi^2 EI}{(KL)^2} \tag{1}$$

To determine the rating for the application, the length value was scaled to match the length of the columns, and the effective length value was adjusted to suit the loading conditions. The effective length value takes on a value of 2, as our column has fixed-free end loading conditions. To scale the rating using the effective length value, the rating, initially given with an effective length value of 1.0, was divided by the new value. To adjust for the shorter span, the rating was multiplied by the ratio of the long length squared over the short length squared. Performing these calculations, it was determined that the critical buckling load for the column is 17,600kg, which is over 200 times the designed load.

Knowing that the column is safe from buckling, it was checked that the stress within the structure is lower than the yield stress of the material. The columns are manufactured from Aluminum Association 5052-H32 aluminum which has a yield strength of 28,000 psi. The stress experienced by a material loaded axially is simply the force exerted over the area of material supporting it. To calculate the area, the minimum area supporting the load through the column was used. This is where the punchout in the sheet is at its widest. The width of the punch-out was subtracted from the nominal side length and the bend radius of both corners was subtracted as well. This gives a length of 1.93 inches of aluminum oriented along the direction of the load, multiplying by the thickness of the material, the minimum loaded area is 0.2413 in^2 per side of the column. Since there are 4 sides of the column the total loaded area is 0.965in^2. Applying the design load to this area gives a stress of 171.3 psi. This gives a simple safety factor of 163.4, which does not account for any stress concentration due to the various changes in geometry. This is acceptable as there is no applicable stress concentration factor that would be great enough to risk yielding the material.

Another load consideration for the truss is the stability of the structure and CRP system. As technicians will need to work under and around the CRP it is important to consider the forces it would take to move the truss and CRP out of position. There are two ways that the system can move, it can either translate or rotate. If the truss and CRP were to translate due to a disturbing force, it would affect the alignment of the CRP, and it would need to be repositioned, but does not risk the safety of personnel. If the truss were to start rotating as if to tip, this could not only move the CRP out of position but potentially cause damage and could harm people working under and around the CRP.

Starting with the tipping stability analysis, the worst-case scenario was investigated. This is the truss with the smallest footprint, which is also the lightest, supporting a CRP and with the tipping force being applied to at the top of the columns, where the CRP rests. From the design of the truss the center of mass of the truss and the CRP are aligned. The distance between the supporting sides of the truss in this configuration is 2.16m, and the distance to the center of gravity is 1.08m from the point of rotation. Solving the force and moment balance gives a required disturbing force of 3256 N to be applied to the top of a column to start the truss tipping. The truss would not actually tip until the center of gravity is directly over the point of rotation on the edge of one side of feet. It is highly unlikely that a human would be able to exert a large enough force to tip the truss on accident.

To determine the force required to translate the truss depends on the friction force of each foot. The friction force is a combination of the normal force exerted by each foot and the coefficient of friction between the interface materials. Each foot is coated with nitrile rubber, and the floor is made of stainless steel. From available literature this value is typically between 0.6 and 0.7. [9] A value of 0.65 was used in the calculations. The normal force is just the weight of the CRP and truss system divided by the number of feet which is four. Solving for values gives a required force of 2352 N. This is 27.8% lower than the force required to start tipping, which provides a reasonable level of confidence that the truss would translate before it tips, which is safer than the inverse. It is also unlikely that a human would be able to exert this force.

With the strength and stability of the structure established, the design of the joints that hold the modular sections was then addressed. The location of the columns was the driving parameter that determined the position and orientation of the truss. It was decided that the columns would carry the fixed hardware, with the cross braces only including the components needed to interact with the columns. As mentioned before, the goal was for the truss to assemble quickly, easily, and without risk of damage to the membrane floor. To meet all these conditions simultaneously, a toolless design was pursued, eliminating the risk of dropping tools onto the floor and reducing the burden on the technicians. Rather than carrying both the structural pieces and any tools, they only need to carry the pieces.

To achieve this toolless design, two pieces of aluminum tube are carried by the column at a set distance from the center of the column. This is achieved by using 0.25” thick 6061 aluminum plates, which are easily laser cut. The plates have clearance holes for the tube, which are then prevented from sliding by snap rings on either end. Two sliders made of carbon steel are also positioned between the two plates, capturing the tubes. These steel sliders are tapped so that a fastener can secure the joint together. The fastener is a cam handle, which can be tightened by hand and then locked in place, much like a standard bicycle seat-post clamp.

Figure 4: Installation Truss modular joint on the column end.

The mating features on the crossbeams are also plates laser cut from 0.25” thick 6061 aluminum, which have radii that match that of the tube, which have an arc measure of just under 180 degrees. At the termination of the arc is a tangent line which extends ½ an inch. The purpose of the angled tangent edge is to allow for the user to have some margin of error when placing the crossbeam onto the column, and so that the slope of the interface guides the pieces together so that the tubes and the radii are concentric. This allows for the distance between the two columns spanned by the cross-brace to be more consistent.

Figure 5: Modular truss joint on the cross-brace end interacting with the column. Note the hooks and the guiding edges.

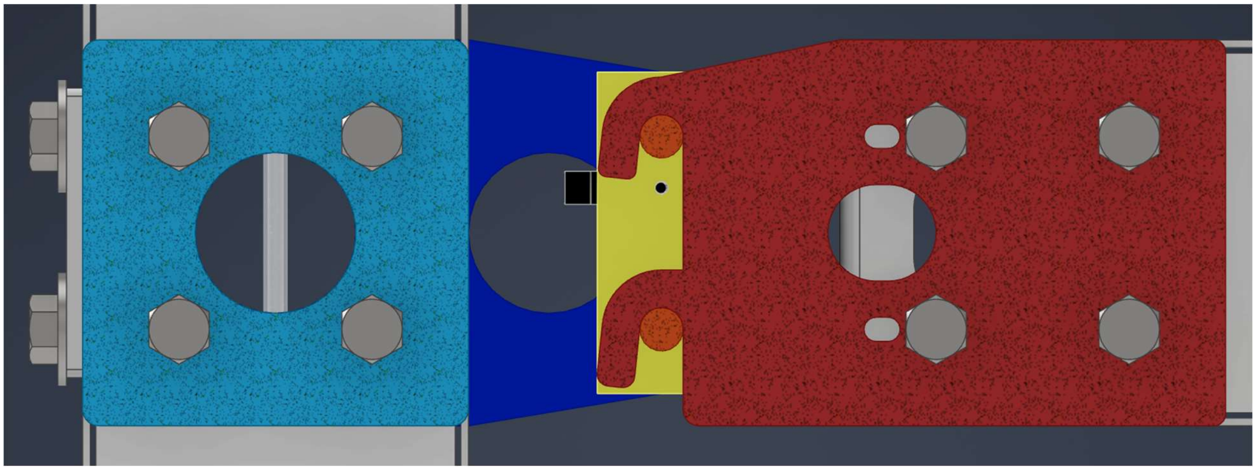

Figure 6: Color coded 3D model section view showing a section view of the column and cross-brace joined together. The red piece is the column hook plate, with the blue pieces representing the column hanger plates. The yellow is the slider.

Lastly, the various crossbeam lengths required for installation at all locations in SURF were determined. As mentioned, due to the membrane floor there are an integer number of valid positions for the feet of the CRP, and the truss columns are located directly underneath the feet of the CRP. This creates a situation where there are three different spans for the crossbeam that are needed. Each cross-member is assigned a letter based on the number of floor sections it needs to span. For example, a section that spans four sections would be assigned D, five sections E, and so on. The entire cryostat was modeled using AutoCAD to determine which spans are needed to install any CRP.

Each floor section is 34 cm from center to center, and ModTruss products are sold in 6” length increments. Due to the difference between the floor spacing interval and the stock material length interval, the longest cross-member was chosen without being too long, and the position of the hook radii on the hook plate was varied to make up the remaining distance.

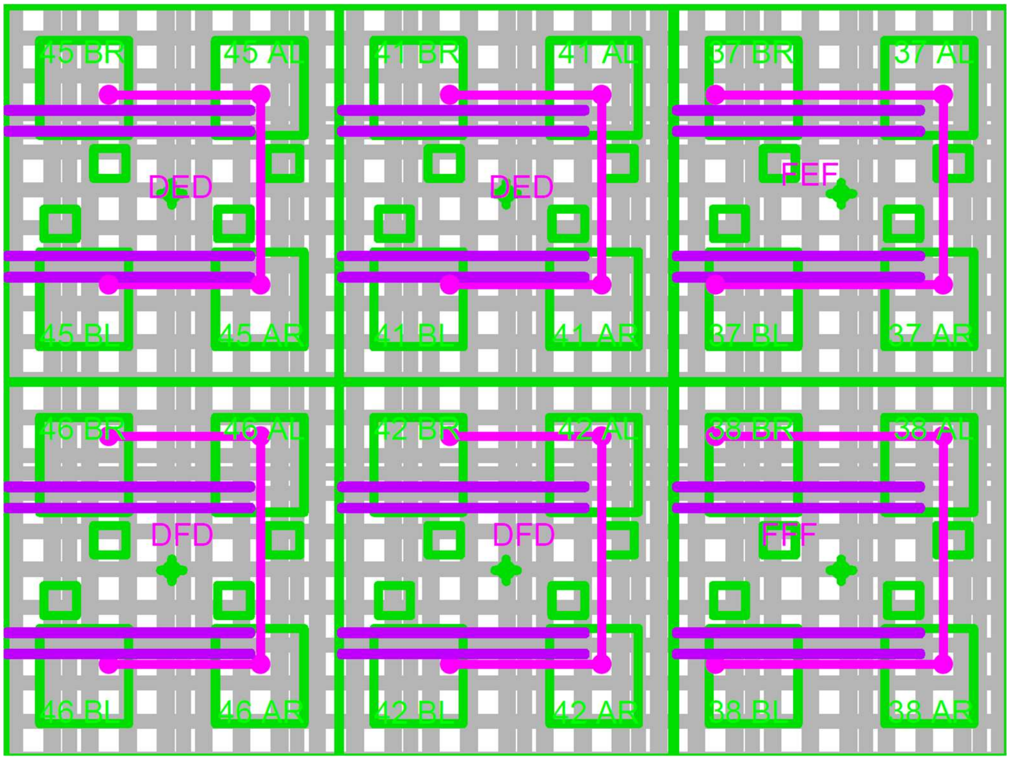

Figure 7: Portion of cryostat floor, CRP with foot positions, and truss system 2D model.

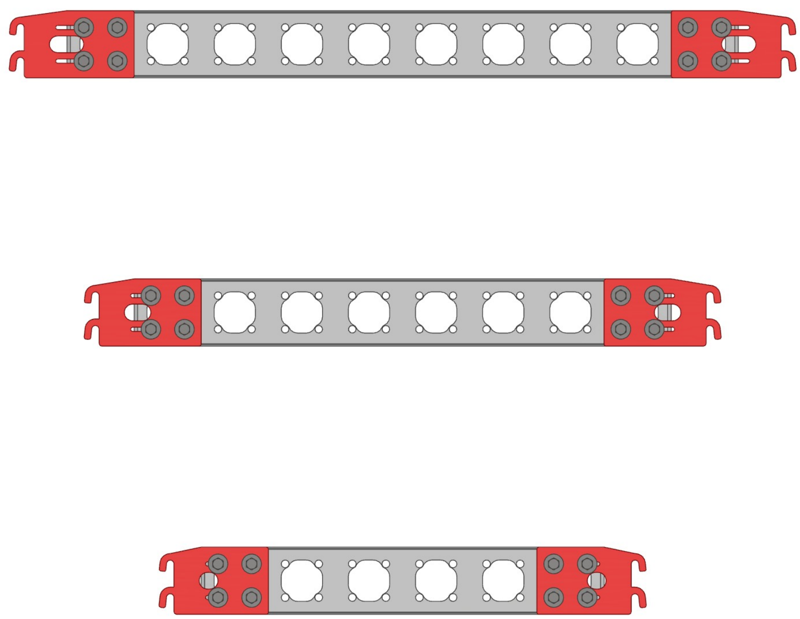

Figure 8: All types of cross-members from top to bottom; F, E, and D. Note the different hook plates for each.

Before shipping the system to CERN for use in ProtoDUNE, the system was tested using a mock CRP, which is of the same size, mass and has a similar mass distribution to a real CRP. The test validated that the truss system can withstand 150% the weight of the CRP, confirmed that the system was easy to set-up with two people, and tested the mechanism which aligns the CRP feet to the top of the truss. To increase the supported load to 150% of the design load, masses were added at each corner to increase the mass to 450 kg. This also provided an opportunity to practice assembling the truss system and assess the ergonomics.

It was found that the truss system was easy to assemble with two people. The process begins with placing two of the four columns in position, in line with each other. At this point one of the cross-members can be brought in and can be hooked to one of the columns. From this point, it can be pivoted into position to hook to the opposite column. Once this is done, the joint can be completed by tightening the cam handle, which presses the slider against the hook plate and eliminates any play. At this point, the first joint is complete. This process is then repeated twice more to complete the truss system. The truss makes a U-shape which allows for easy access and egress from the side of the truss that doesn't have a cross-member. A full procedure, including the load and stability analysis from above is available in Appendix A.

Figure 9: Image of the truss system being tested at UW.

The results of our testing were found to be satisfactory. The truss system easily supported 450kg with enough stability to provide a sense of confidence. It was also found that the alignment of the CRP feet with the truss columns worked as intended, including the centering mechanism. However, ensuring that the columns were appropriately plumb was more challenging than anticipated, would be an aspect targeted for improvement. Lastly, it was found that with little practice, the truss system could be assembled from its components in 5-10 minutes by just two people. Satisfied with these results, the prototype system was sent to CERN to be used to install a CRP into a cryostat for ProtoDUNE.

ProtoDUNE provided an opportunity to assess the performance of the truss system prototype in a live situation and with individuals not intensely involved with the design and manufacture of the system. Specifically, it allowed us to determine if the system was too cumbersome to work with on the membrane floor and understand how it interacted with the cabling process of the CRP. Note that all the cables must be inserted on the underside of the CRP, in the same area that a technician would be while underneath the truss system. Installing the cables is a long and delicate process, so the truss needs to be as little of a hinderance as possible. Fortunately, feedback from technicians was positive and the truss felt stable and secure to work underneath, while allowing ample room to perform the cabling. It even allowed the technician to sit in a chair while performing the work.

From an environmental health and safety (ES&H) perspective, the truss was well liked. However, the feedback showed that a method would need to be developed to retrieve the truss without a person being underneath the CRP while it is suspended by the crane. The design used at ProtoDUNE required that once the CRP is lifted off the truss, then two people would disassemble the truss, following the inverse of the procedure described above and attached in Appendix A and carry the members away from the CRP. To provide protection for the people who would perform this task at ProtoDUNE metal bars that ran across the length of the CRP and are then supported on each end were placed underneath the CRP. These would catch the CRP if the crane were to fail and drop the CRP. Due to the space constraints in the vertical drift detector at SURF, this method would not be workable.

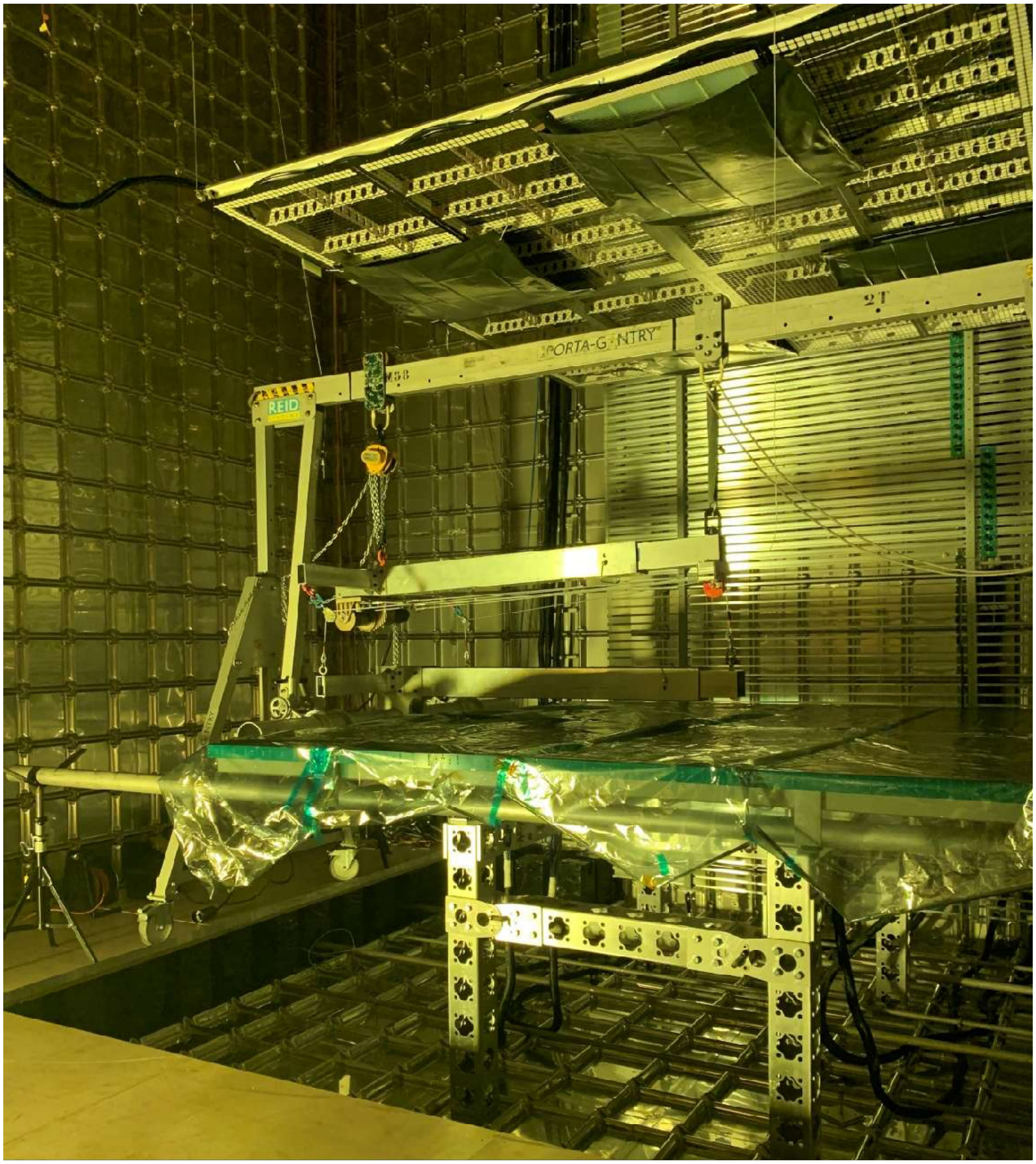

Figure 10: The Installation Truss System in use at ProtoDUNE. Note the catch bars to protect users during removal.

2.2. Improvements Required from ProtoDUNE to Vertical Drift Detector Installation

As mentioned, after using the system at ProtoDUNE, it was clear that two aspects of the Installation Truss System required refinement. One of these is that it was difficult to ensure that the columns were plumb during installation. They would have to be measured, then adjusted or readjusted, then measured again in an iterative and tedious manner. The second is that the truss system needs to be removable from the CRP installation site without people removing members. Both need to be addressed in a manner that can be deployed at SURF.

The cryostat at SURF is similar in structure to the one used at CERN during ProtoDUNE, but is much larger, and many more CRP need to be installed. Also, there is much less access to CRP from the edges. So, when installing CRP in the cryostat at SURF, there are situations where all equipment and persons must be directly ahead of one edge of the CRP, as it is constricted by neighboring CRP or the walls in all directions. For setting up the truss, this is not an issue, however during retrieval this is essential to consider. Because of these space limitations catch bars like those used in ProtoDUNE cannot be used, and the truss must move in a single direction throughout the process of retrieving it.

2.3. Truss Retrieval System

From testing at ProtoDUNE it was clear that there needs to be a way to retrieve the Installation Truss without disassembling it while underneath the slung CRP. To achieve this the truss needs to become mobile once the cabling is complete and the CRP is lifted. The simplest solution would be to move the truss straight back to the false floor. The false floor is a wooden surface located approximately 5” above the flat surface of the membrane floor, supported by pedestals. Because the truss is designed to transmit the load of the CRP to the membrane floor, it must rest on the membrane floor during cabling. Therefore, for the truss to reach the level of the false floor, it must be lifted.

2.3.1. Truss Lifting System Design

To lift the Installation Truss, several mechanisms were considered. One of which was linear actuators. Linear actuators are electromechanical devices which use electric motors, and a power screw produce linear motion. These devices have several advantages and disadvantages. The first major advantage is that they can be programmed to move to any position within their range, and the speed can be controlled. Another advantage is that there is already going to be electronic control for the lifting mechanism so it could be possible to use the same controller. However, the disadvantages outweigh these advantages as linear actuators are expensive compared to other options, are larger and heavier compared to other options, and introduce an electrical discharge potential near to the CRP after it has already been tested.

Another option would be to use hydraulic cylinders which eliminate the discharge potential and are lighter and smaller than linear actuators. However, hydraulic systems operate at exceedingly high pressures, and require additional pumps and reservoirs, which make them expensive, and require space outside the footprint of the CRP. They also introduce the possibility of hydraulic oil leaks, which would need to be cleaned up, and risk contaminating the liquid argon environment. Due to these concerns, hydraulics were not selected.

The lifting mechanisms that were selected are pneumatic cylinders, which operate similarly to hydraulic cylinders but use compressed air as the working fluid. This eliminates the risk of contaminating the liquid argon environment. Additionally, pneumatic cylinders and their supporting equipment such as air compressors, hoses, and fittings are less expensive than hydraulic cylinders and their supporting equipment.

After pneumatics were selected, the pneumatic system design was then carried out. The system must be able to lift the truss but not the CRP, therefore each cylinder must support one quarter of the estimated mass of the truss. In the largest configuration, with pneumatics and other hardware for retrieval fitted, the truss was estimated to weigh 250 lbs. Therefore, each cylinder would need to provide 62.5 lbs. of force to keep the system statically stable. The smallest practical pneumatic cylinder bore was 2 in. This sets the required pressure at 19.9 psig. This allows for the use of polymer fittings which are lighter and less expensive. The pressure is controlled by a pressure regulator. The regulator vents any excess pressure to be ambient and sets the pressure of everything downstream.

The pneumatic cylinder is double acting, meaning that it has two ports, one on each side of the piston. Each chamber can be pressurized or vented to ambient pressure independently. The difference in pressure between the two chambers is what drives the piston. To control the position of the cylinder a directional control valve is used. The directional control valve has 5 ports and can be in one of two positions. One of the 5 ports is the pressure supply, which is directly connected to the output of the pressure regulator. On the same side as the pressure supply, there are two exhaust ports, which evacuate the top or bottom chamber of the cylinder. On the opposite side, there are the two ports which supply air to either the top or bottom chamber. To alter the routing of air, there is a lever on the side of the directional control valve. The lever has a spring detent which keeps the lever in a default position unless a user holds the lever in the other position.

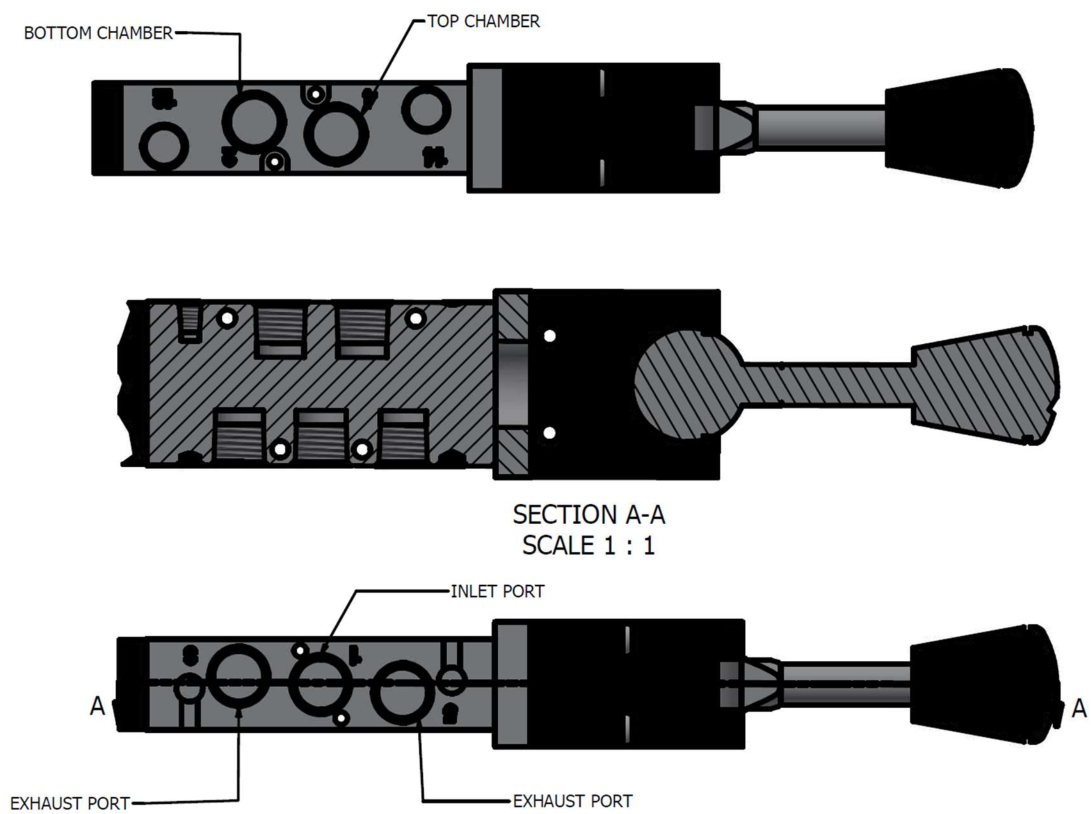

Figure 11: Diagram of the air paths through the directional control valve.

The default path for air passing through the valve was configured so that the default position routes air to the bottom chamber of the pneumatic cylinders, while the top chamber is connected to an exhaust. Remember that attached to the pneumatic cylinders are the feet of the installation truss, so this default position keeps the feet retracted. Therefore, when the truss is stationary, the default lever position ensures that the truss is on the floor. This default position also ensures that the feet stay retracted when the truss is in its travel position and does not interfere with the membrane floor.

2.3.2. Truss Rail Indexing Method

The platform must be as close to the height of the false floor as possible, so that the the truss can easily be moved onto the false floor without lifting it, or allowing it to drop a significant distance. The platform must be rigid enough to support the weight of the truss and any additional retrieval equipment. Additionally, the platform must be easy to locate into the correct position, and not damage the false floor. The platform must be as light as possible, as it will need to be placed and removed by people, while being long enough to span the truss and the distance to the false floor. Lastly, the platform must be either large enough to provide ample space to retrieve the truss, or provide a captive or guiding element that keeps the truss on course throughout the retrieval process.

The easiest way to locate the truss retrieval platform is to reference existing geometry that is at every CRP install location. A constant feature throughout the cryostat is the ridges and knuckles of the membrane floor as seen in Figure 2. These occur at regular intervales of 34 cm from the center of each square to the next. There are two types of ridges with different heights and profiles, which run in perpendicular directions. Due to some unique install locations, notably the corners, there will be occasions where the retrieval sysem needs to pass over both, and index off both. However, as mentioned above the exact shape of the profiles of the membrane floor are unknown to us, as the company that designed and installs the membrane floor does not provide them. Therefore, during the design process, the profiles had to be either determined by us or a solution had to be engineered that does not require exact knowledge of the shape.

The initial approach was to attempt to determine the profile of the ridges and then design the mating surface to match it exactly. The first method attempted was the use of a 3D laser scanner to capture the geometry of the flat panel of floor. This required the piece to be covered in talc powder so that the polished surfaces would not interfere with the measurement. This worked, but the resulting model was not accurate enough to be able to develop a match. The next attempt involved tracing the profile, then laser cutting acrylic templates, comparing the fit, and revising. After dozens of iterations, several templates were produced that fit, but the fit seemed to vary with each attempt. At this point, one template was placed where it fit the best, then slid along the ridge. It was observed that the fit changed along the length of the ridge, which was visible to the human eye and could be felt tactiley. Therefore, the profile was found to be inconsistent along the length of the ridge, which led to an investigation of whether the two ridges of the same type were symmetrical. It was discovered that they were also not symmetrical.

At this point, it was determined that the ridges were not manufactured consistently enough to allow for the use of a singular profile for each type of ridge. Therefore, the approach had to be changed, and a solution had to be developed that did not rely on using the exact profile of the ridges. To do so, triangular templates shaped like 45-45-90 triangles were used, with the hypotenuse being made to contact the membrane ridge, and the contact point was marked with a paint marker. More templates were then laser cut with this contact point designed in, and a few adjustments were made to achieve a good fit. This method was more reliable as it prevented overconstraint, and reduced the play in the fit.

To compensate for the variance in the profile of the membrane, the cutout on the template was offset by 1/16", allowing for a layer of 1/8" compressible foam to be placed along the contacting surface. The foam would take up any tolerance in the geometry and provide a soft surface to contact the membrane floor, preventing damage to it.

Figure 12: Example of the finished design showing on a support index designed for the short membrane ridge.

2.3.3. Truss Rail Design and Integration with Indices

Since remaining lightweight was a primary consideration, the lightest Aluminum Association standard channel, AA CS 2 x 0.557, was chosen. This channel has a weight per linear foot of 0.557 lb/ft, making it the lightest option available [10]. As the goal was to integrate with the false floor as seamlessly as possible, the bottom of the channel was designed to be coplanar with the top surface of the false floor, which is at a height of 128.3mm. Since the channel would span the length of the truss and bridge the distance to the false floor, which approaches 1m in some rows, it was decided to support the channel every 34cm, or once per membrane grid section.

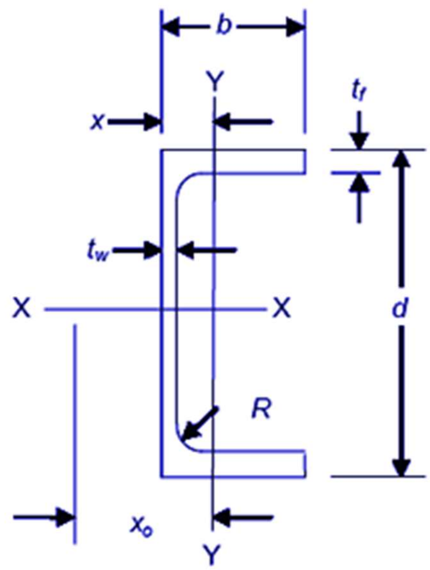

Designation CS	Depth d in.	Width b in.	Flange Thickness t_f in.	Web Thickness t_w in.	Fillet Radius R in.	Area A in^2	x_o in.	C_w in^6	J in^4	r_0 in.
2 x 0.577	2.000	1.000	0.130	0.130	0.100	0.490	0.626	0.0324	0.00274	1.03

Figure 13: Figure showing the dimensions and mass properties of the chosen section. [10]

The design of the indices is completed with the section width of the rail, and the the height of the false floor which is 128.3 mm. There are two different supports, one for each type of ridge on the membrane floor. Because may of these components will be needed they need to be easy to manufacture in large quantities. In addition each support needs to be as light as possible so that the completed rail assembly remains manageable for technicians to manipulate. To meet both of these criteria, high-density polyethylene was selected as the material, as it is inexpensive, easy to machine, available in a wide variety of stock material shapes, and lightweight.

The first component designed was the support which interfaces with the membrane floor. The design uses the 45-degree tangent line from the method mentioned above and includes feet that contact the flat portion of the membrane floor, along with a flat top surface that contacts the bottom of the rails. To reduce the mass of the part, a siginificant amount of material is milled out of the part between the top surface and the crest of the cut out for the ridge. A secondary purpose of this gap is that it provides a location to use M5 nuts to secure the supports to the rails which have a countersinks for M5 bolts. The supports which interact with the large membrane are similar in design to those just described, but the feet which rest on the flat of the membrane are taller.

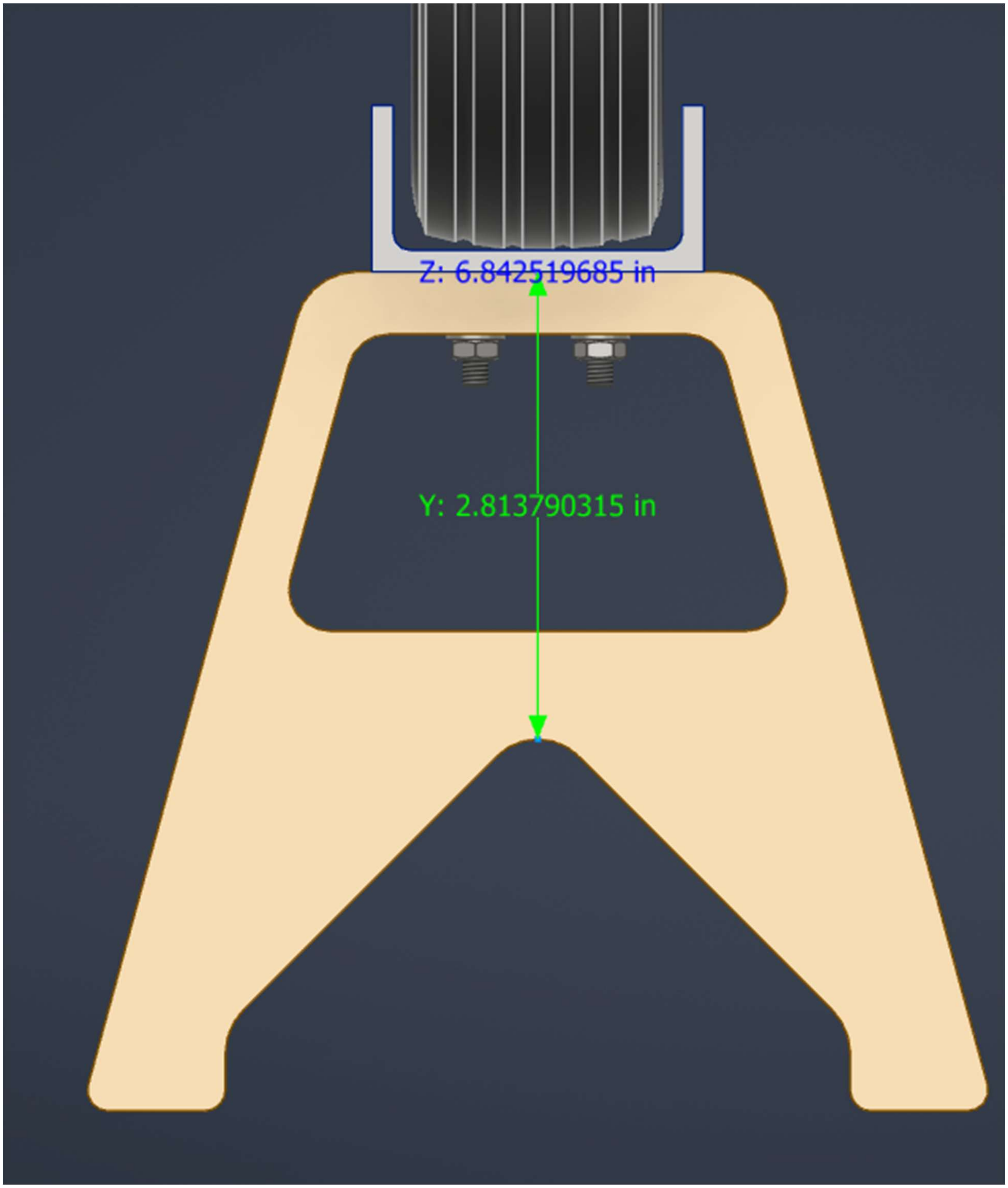

Figure 14: Tall membrane block showing assembly with the rail.

Due to the softness of HDPE, these blocks can be easily manufactured using a CNC router, rather than a vertical mill, which allows many pieces to be produced by a single program without having to set up a new piece of stock. This saves time during the machining process and elimnates the need to cut down large sheets of stock into smaller pieces more similar in size to the final product, and that would fit in a typical mill, this also saves material. To set the pieces up, several small holes are drilled into the stock material along the centerline and near the corners, so that it can be secured to the table of the router. The program is then loaded to cut the pockets and profiles necessary to produce the part.

2.3.4. Design Analysis of Truss Rail Indices

To ensure that the designed system is safe, a mechanical stress analysis on the system was performed using the commerical analysis software package ANSYS. According to the supplier the HDPE is extruded by King Plastic Corporation and is King Performance Commodity HDPE. According to the manufacturer specifications this material has a tensile modulus of elasticty of 255 ksi. It is assumed that the compressive modulus of the polymer is equivalent to the tensile modulus. Additionally, the manufacturer claims a yield stress of 4100 psi. [11] For our model a von Mises Stress equal to 4100 psi is considered to be the failure criterion. Lastly, an estimate of the Poisson's ratio of the material was required, but it was not provided by the extruder. To determine an appropriate design value of the Poisson ratio, literature was consulted, where it was found that, according to the Plastics Pipe Institute, the recommended design value is 0.45. [12]

To ensure that the model is accurate boundary conditions and loads must be considered carefully. The load applied is the weight of 1/8 of the installation truss as there are two spacer blocks per column on the truss plus ¼ of the mass of the retrieval cart system, approximately 17.75 kg. As the alumminum channel is expected to be much stiffer than the plastic supports, it is then assumed that the load will be distributed evenly across the top face of the support. This leads to a calculated applied presssure of 18 psi to the model. The boundary conditions chosen are that the node which is located at the intersection of the axes of symmetry in the XY and XZ plane are not allowed to displace in the X or Z direction. This is effectively a symmetry boundary condition which forces the model to displace symmetrically about the logical axes of symmetry, and prevent rigid body translation and rotation within the body. The final boundary condition is that the edges at the bottom of the arch are not allowed to displace in the Y direction.

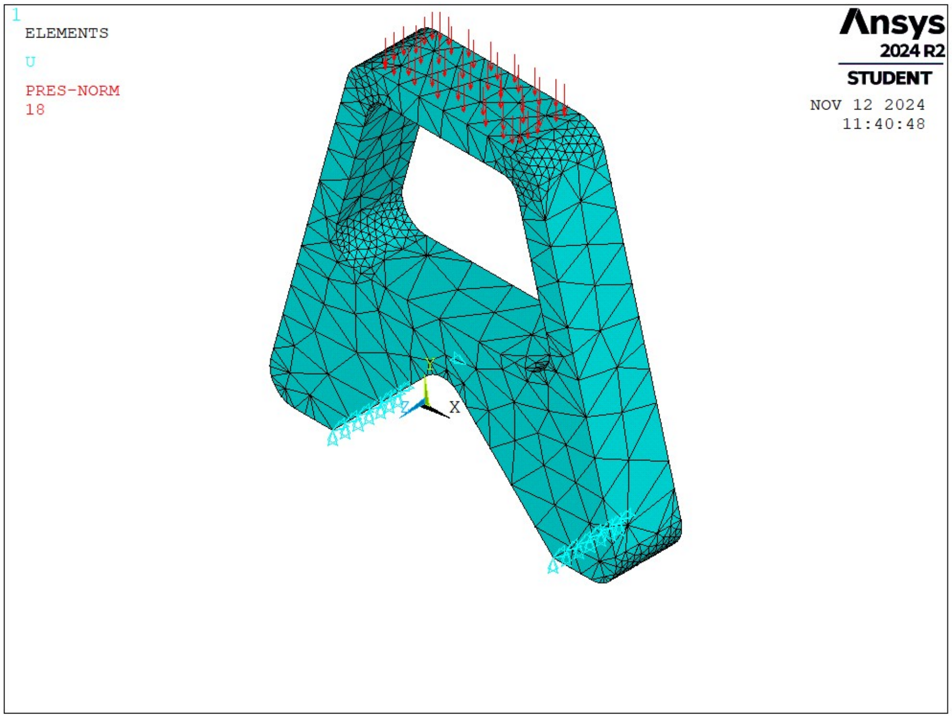

Figure 15: Figure showing the boundary conditions and loads of the rail spacer support block.

To analyze the results the functional requirements of the component must be identified, and they are listed here. Firstly, it must support the weight without yielding, which is evaluated using the von Mises strain energy failure criterion. Second, the top must not deform to the point that there is a risk of the foot of the truss striking the false floor edge. Lastly, the contact surfaces on the arch which center the block with respect to the membrane corrugation must not displace more than the foam can comply.

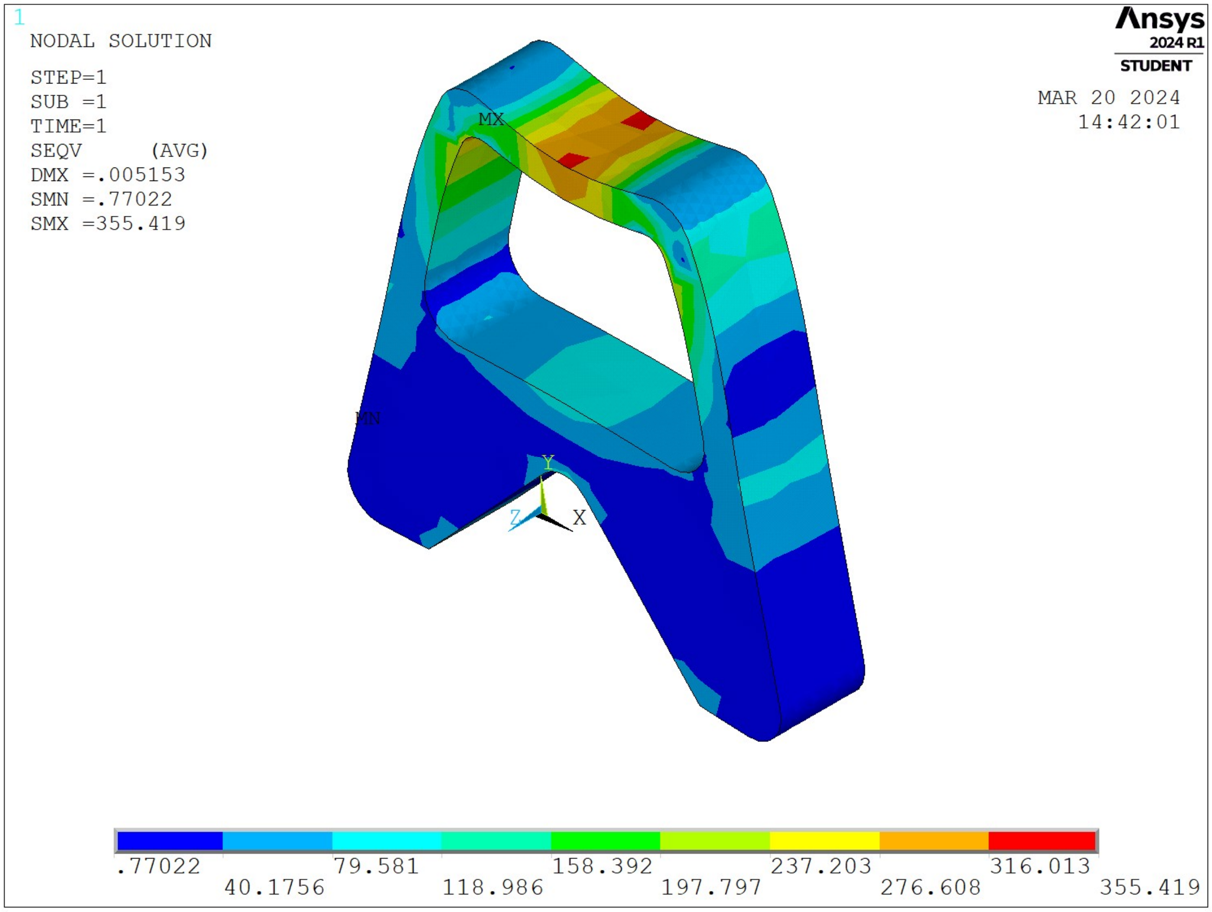

Figure 16: von Mises Equivalent Stress in the rail spacer support block.

The resulting von Mises equivalent stress is plotted in Figure 16 which shows colored contours corresponding to different levels of stress in psi. The maximum von Mises stress of 355.4 psi, corresponding to a safety factor of 11.53, occurs at the expected location—along the middle edge of the top surface, where it is furthest from support and closest to a potential stress concentration. This high safety factor shows that the design does fulfill the first requirement and that the components will not experience yielding.

The second design requirement stipulates that the top surface of the rail support block cannot displace so much that the foot of the truss could strike the false floor edge during retrieval. This value is equal to the thickness of the channel rail, as the bottom face of this rail is coincident with the top face of the false floor. This thickness as provided by the aluminum association standards is 0.130," so this is the maximum allowable y-displacement of the top face. Figure 17 shows top face has a maximum displacement of 0.0051” downwards, which is significantly less than the thickness of the rail, so this requirement is fulfilled.

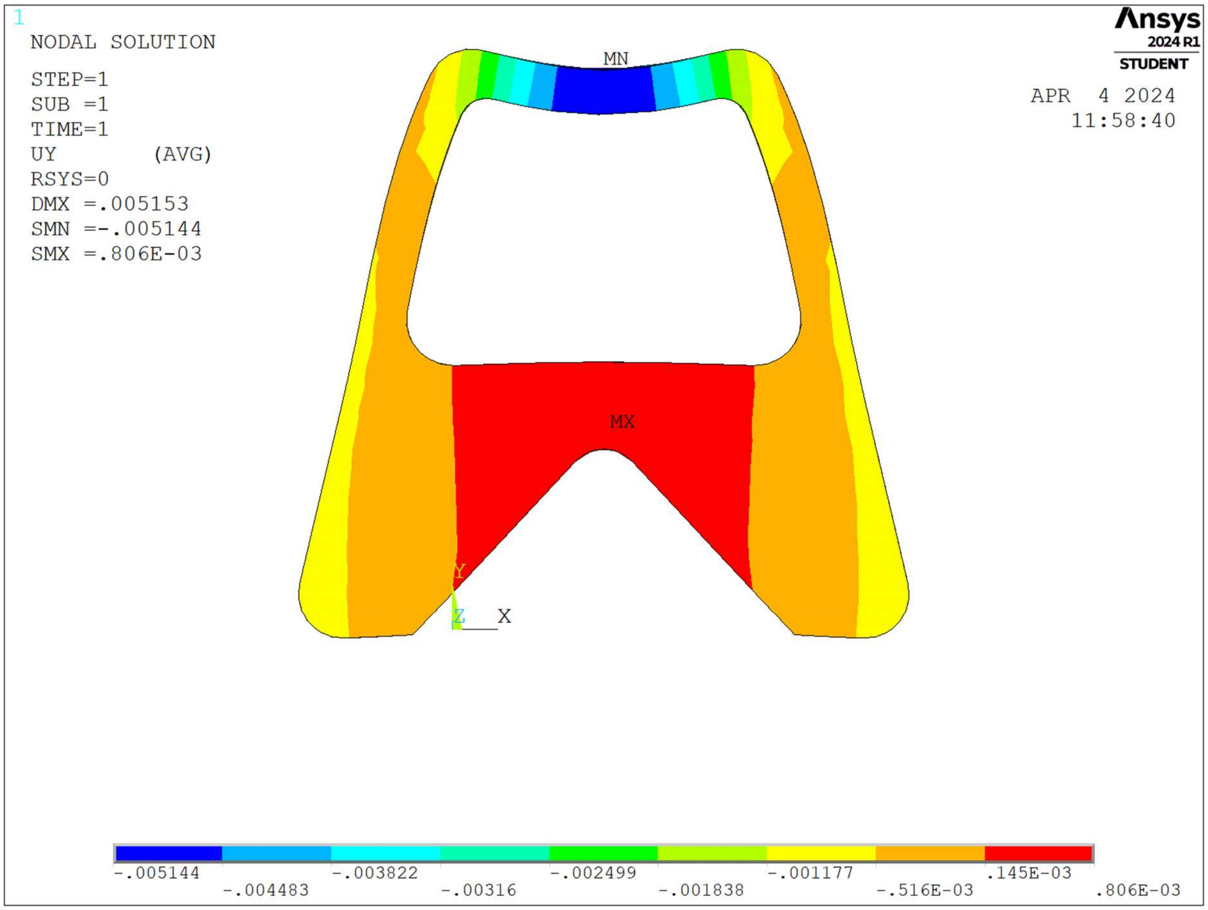

Figure 17: Contour plot of y-displacement in the rail spacer support block in inches.

The final requirement is that the resulting deformation in the indexing surfaces that align the rails with the membrane floor corrugations do not displace so much that contact is lost. This occurs when the displacement magnitude is greater than the amount of displacement remaining in the foam. The foam is 1/8” in thickness, and the offset of the arch from its tangent path is 1/16”, therefore the maximum displacement is 1/16”. From Figure 18 it is shown that the maximum value of displacement along that edge can be 0.0018” which is much smaller than 1/16”, so this functional requirement is also fulfilled.

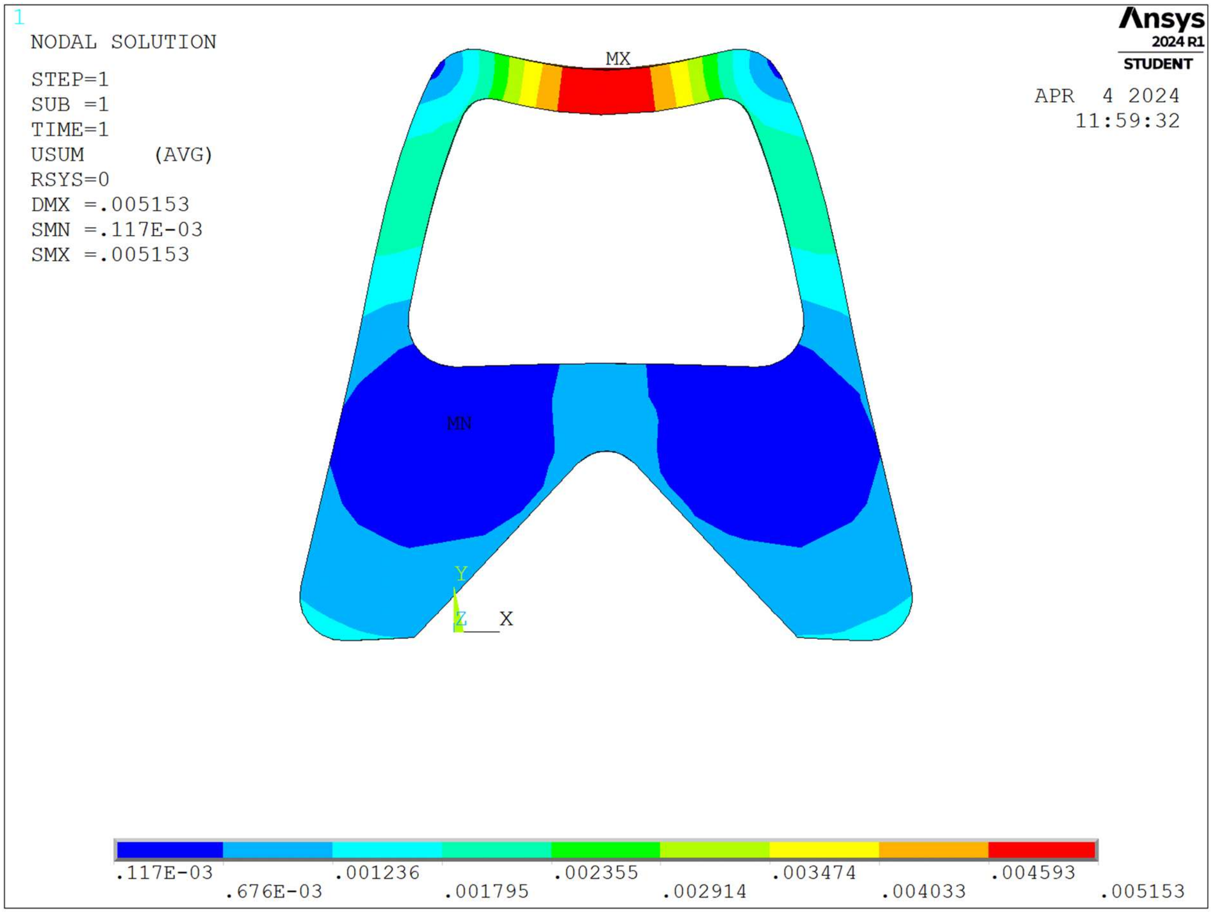

Figure 18: Plot of the vector sum of displacement within the rail spacer support block.

Due to the difficult nature of the geometry, these results are difficult to validate using simple hand calculations, so the results were validated by conducting real world testing. The testing was a simple compression test performed by placing the material on a rigid bed made of steel, and then using a crosshead equipped with compression platens to apply a load. The applied load is measured by a load cell in the bed plate. The crosshead displaces at a constant velocity of 0.0847 mm/s and data is sampled at 10 Hz.

Typically, the data acquired from the machine would be post-processed to turn the crosshead displacement into a non-dimensional strain using the equation $\varepsilon = \Delta L_{crosshead}/L_{char}$ where L_{char} is a characteristic length representing the length of the element/structure that being tested. For example, in a beam this would be the length of the beam. For this geometry, no obvious or convenient characteristic length is present, so the data is left in terms of the crosshead displacement. These data are plotted in Figure 19 along with a linear extrapolation of the linear portion of the data.

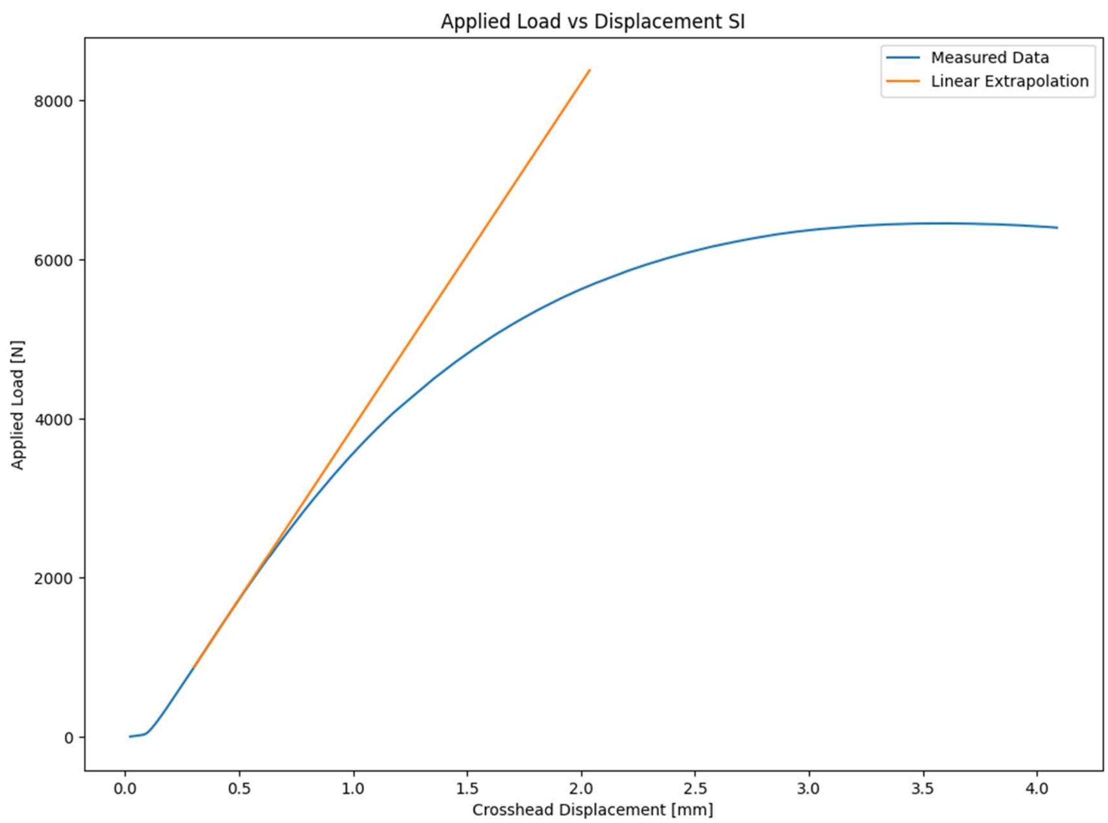

Figure 19: Applied load vs crosshead displacement.

The data shows a small tail at the front where the applied load barely responds to crosshead displacement, this is from the portion of the test where the compression platens are coming into contact with the test sample. From the end of that point until approximately 0.8 mm of displacement the load is related linearly to displacement, where the material is within its elastic region. Beyond this transition point, the relationship is non-linear representing the plastic deformation region. The linear extrapolation aids in determining the point at which plastic deformation begins to occur. From the plot above alone, it can be estimated that yielding begins to occur somewhere between 2000N and 2400N, and the ultimate strength is located at 6450N. To capture the point where yielding begins, the value of the measured data is compared more accurately to a linear extrapolation from the elastic region of the data. The expected linear load is subtracted from the observed load, then divided by the expected linear load, and multiplied by 100. The equation below shows this mathematically. The point of yielding is when this deviation reaches 2%, corresponding to an observed load of 2260 N (508 lbf). To be conservative, a load rating of 450 lbf is assigned to the spacer blocks.

$$\delta = \left| \frac{(P_{observed} - P_{linear})}{P_{linear}} \right| * 100 \tag{2}$$

Symbol	Quantity	Units
$P_{observed}$	Observed Supported Load	lbf
P_{linear}	Hypothetical Supported Load if Material is Perfectly Elastic	lbf
δ	Percent Deviation from Linear Behavior	%

More detailed methods, results, and discussion of this model, as well as structural mechanical models for other components of the truss retrieval system are in Appendix B. The rest of the components will not be covered in as much detail in the main body as the rail spacer blocks as the model as those models are much simpler and less interesting, but the full detail is available in the appendix.

2.3.5. Gusset Plate Design

The gusset plate serves to support the weight of the truss while it is riding the truss retrieval carts. The load is modelled as a uniform distributed force along a contact area which is the thickness of the plate, and the length is the width of the truss retrieval cart. The centroid of this area is located on the gusset plate where the center of the membrane corrugation is. The model is a symmetry model, where one half of the gusset plate is modelled and all the nodes along the axis of symmetry are fixed. This provides us with the results seen below. The design must not experience any yielding, and the y-displacement of the contact area must not be so large that the foot of the truss strikes the edge of the false floor. Figure 20 shows that the maximum stress is 1458 psi. When compared to 6061 aluminum's yield stress of 40,000 psi, as reported by the online materials database Matweb, a resulting safety factor of 27.43 is obtained, providing confidence that no yielding will occur. [13] The plot of y-displacement in Figure 21 shows that the maximum displacement occurs at the centroid of the contact surface, and this magnitude is 0.82 thousandths of an inch, which is negligible. Therefore, the gusset plate fulfills its designed purpose.

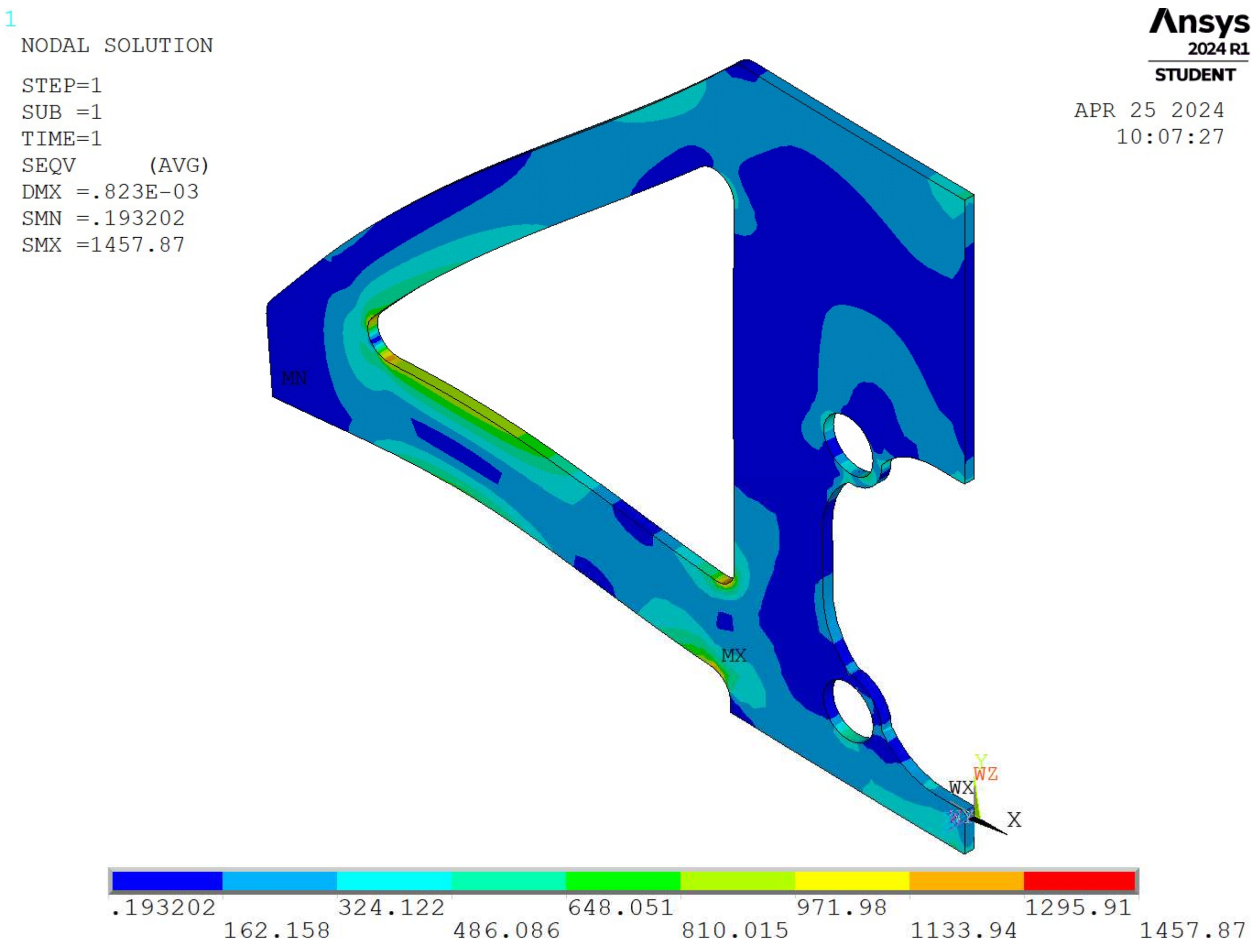

Figure 20: Contour Plot of the von Mises stress within the gusset plate.

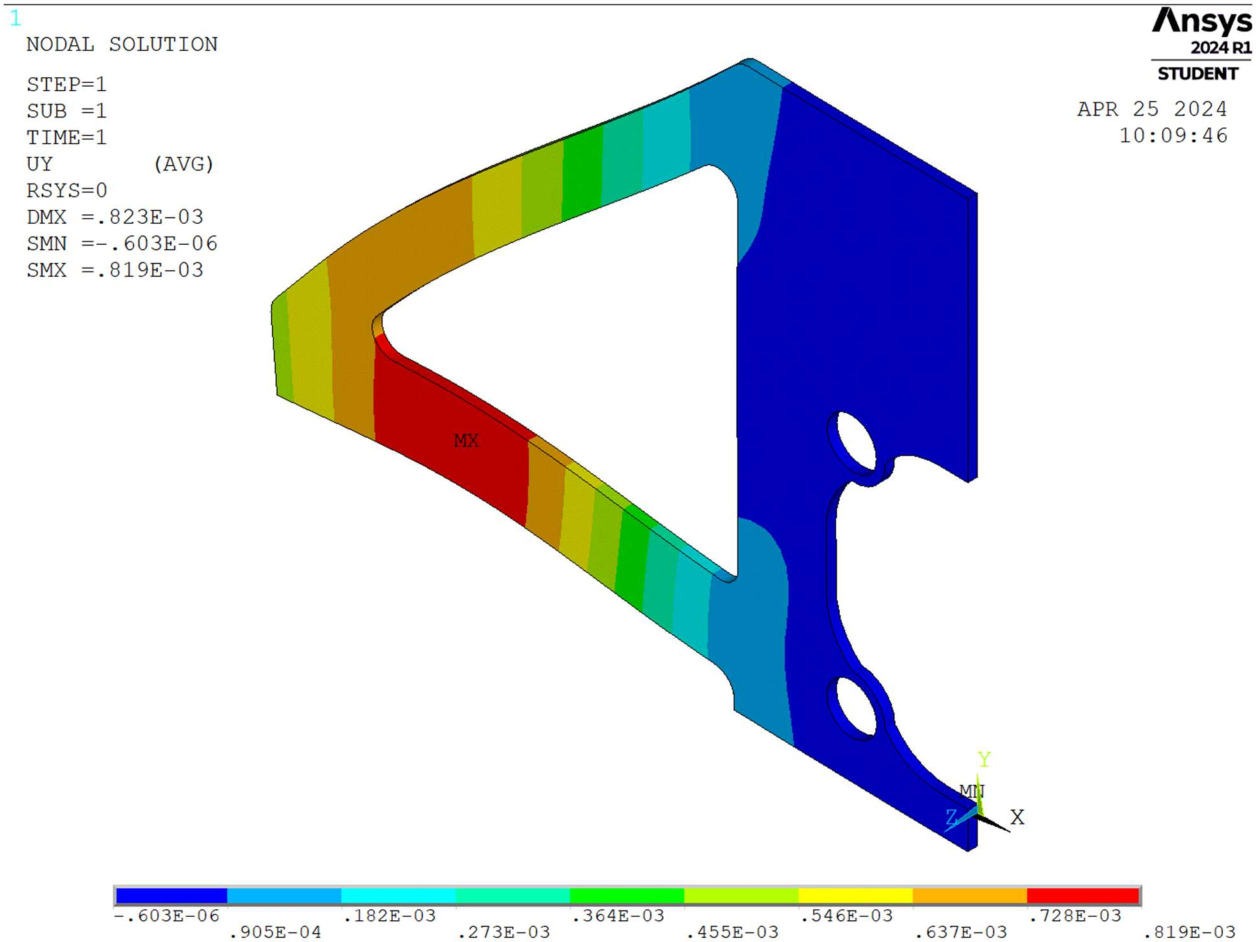

Figure 21: Y-displacement in the Gusset Plate

2.3.6. Truss Retrieval Cart Design and Design Analysis

The last component of the retrieval system is the carts. The carts are what will allow the truss to roll along the rails. The carts need to be linked together on each side of the truss. This is accomplished using clevis ends on a tie bar. This comes in different lengths to accommodate the various stances of the truss. The clevis ends are secured to the carts using a quick release pin. This attachment is done on a piece of aluminum C-channel which also serves as a bump stop. The bump stop is used as a method to provide feedback to the user that they are in the correct position. Once the user feels the channel touch off on the gusset plate, they know that the carts are in the correct position. This is because the channel face position is intentionally designed such that once it contacts the gusset plate, the gusset plate is centered over a set of plates which create a channel for the gusset plate to rest in.

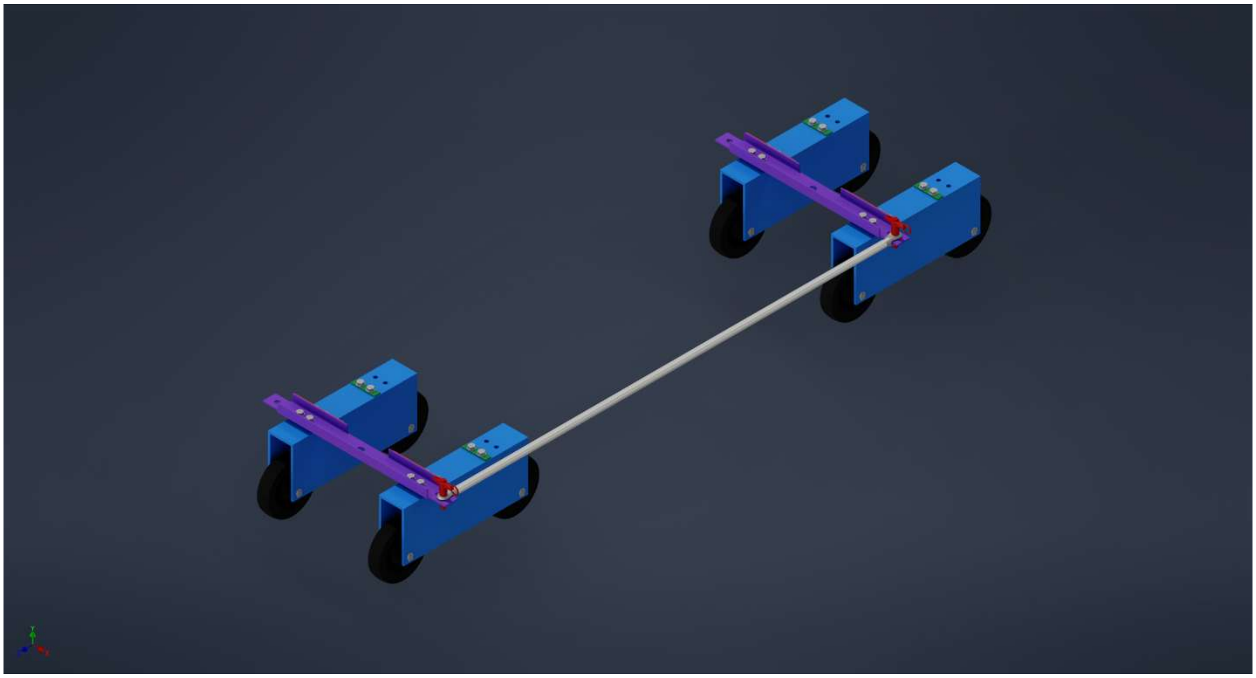

Figure 22: CAD Model of Truss Retrieval System Carts

In Figure 22 the various components are color coded. The cart body is shown in cyan; this component is the structure of the cart and provides the hardware mounting features and locations. The purple component is the C-channel bump stop and is what engages with the triangular face of the gusset plate. The tie rod is shown in silver, where you can see a quick release pin in red. The green plate is one of the catches that keep a gusset plate from moving.

The truss retrieval cart is made from a rectangle structural tube section which has dimensions 6” x 3” x 0.1875”. The material is 6061 aluminum and uses the same material properties as the gusset plate. The load is modelled as uniform pressure over the area of the gusset plate in contact with the cart, this is a good approximation as the gusset plate has negligible deformation in this area from that model. The model is constrained by taking advantage of symmetry. Nodes located in the YZ of the tube are prevented from displacing in the x-direction, and nodes located at the XY plane are prevented from displacing in the z-direction. The nodes along the contact surface with the axles are not permitted to displace in the y-direction. These boundary conditions and loads are shown in Figure 23.

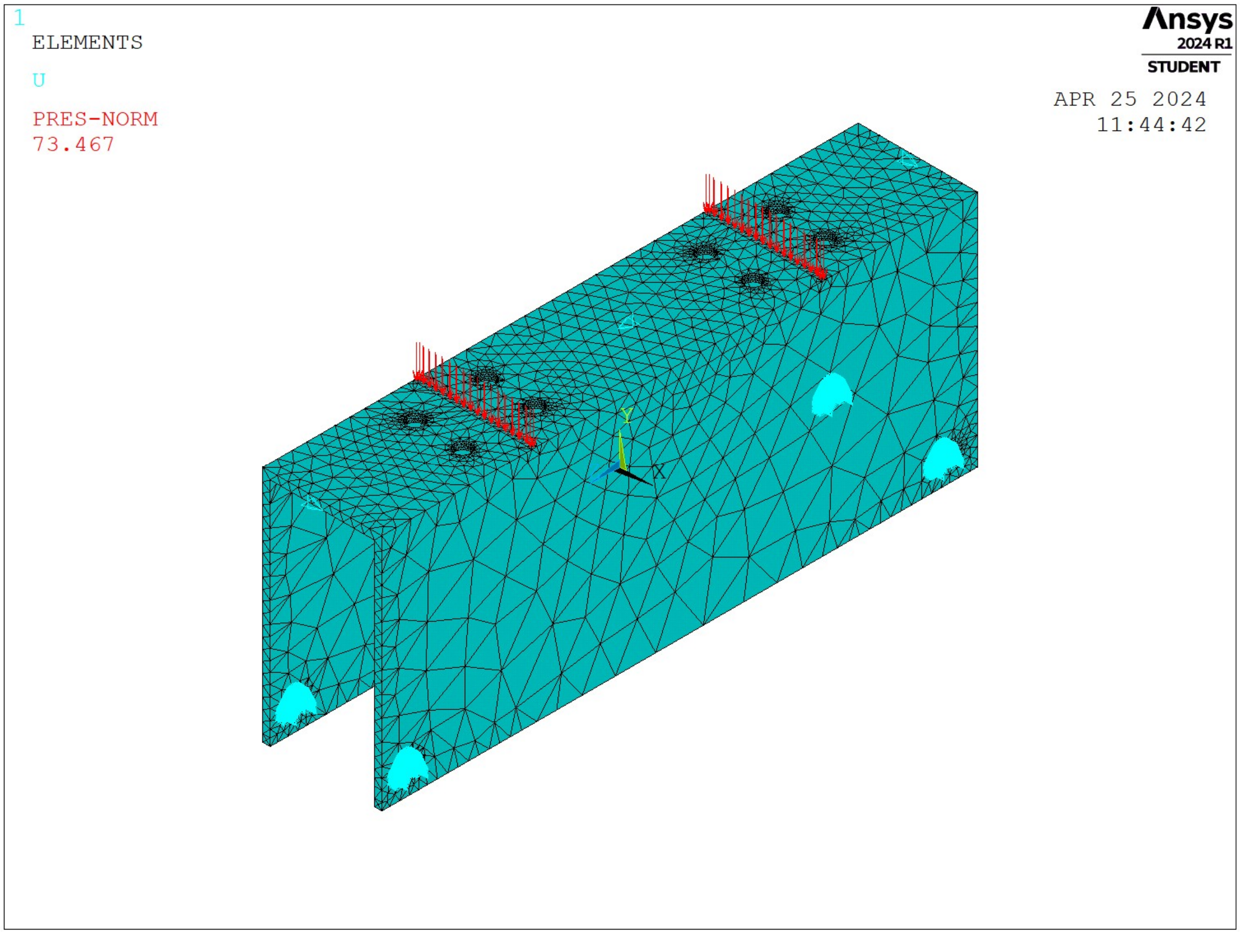

Figure 23: Boundary conditions and loads on the truss retrieval cart body.

There are two parameters that the model is used to calculate, the maximum von Mises stress, and the deflection of the contact surface. The maximum von Mises stress of 649.7 psi occurs at the surface where the body meets the axle as shown by Figure 24. Compared to the yield strength of the alloy, which is 40,000 psi, the safety factor is 61. The deformation of the contact surface is 2.6 thousandths of an inch and is shown in Figure 25, where the deformation in the y-direction is plotted over the body.

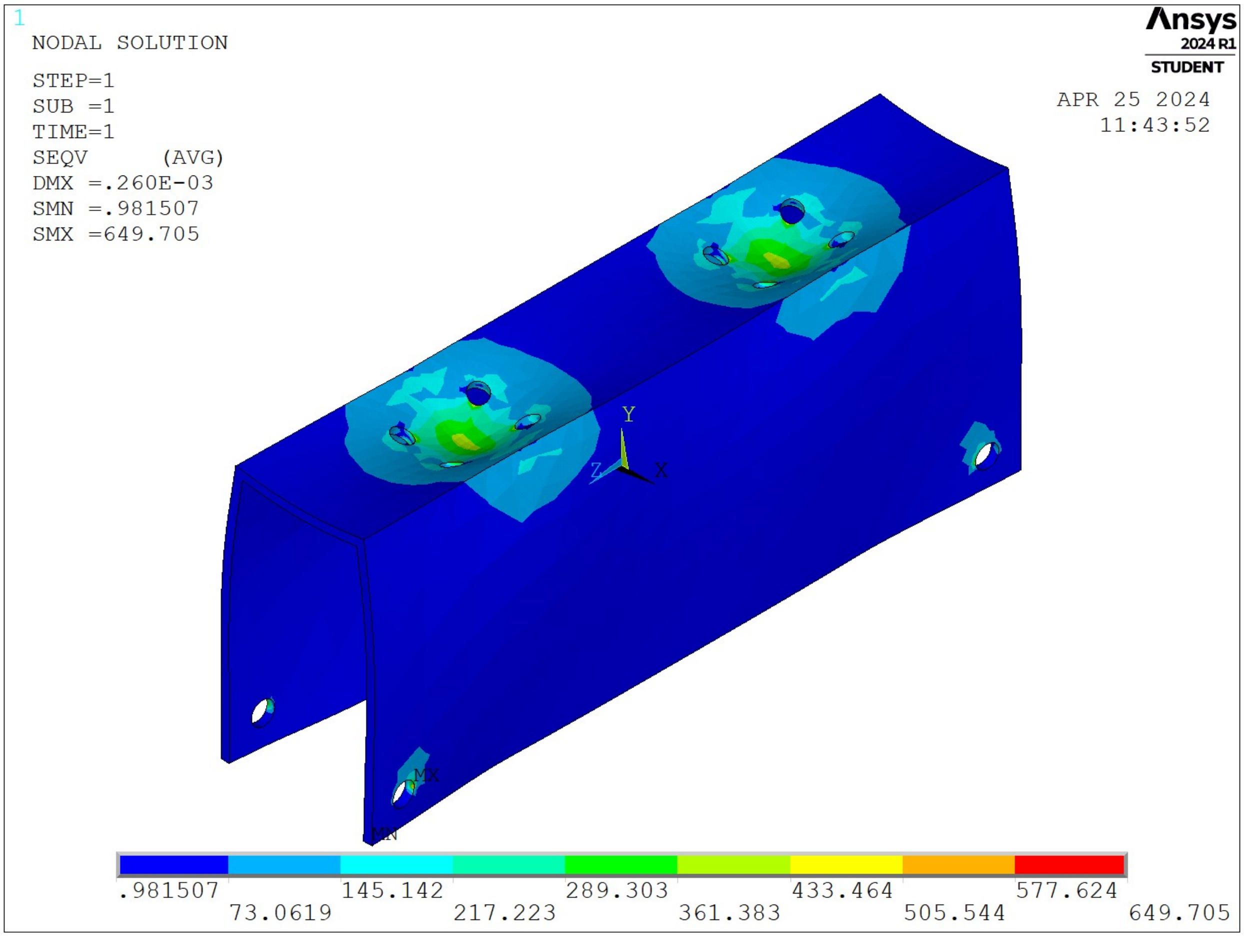

Figure 24: Contour plot of the von Mises stress in the truss retrieval cart body.

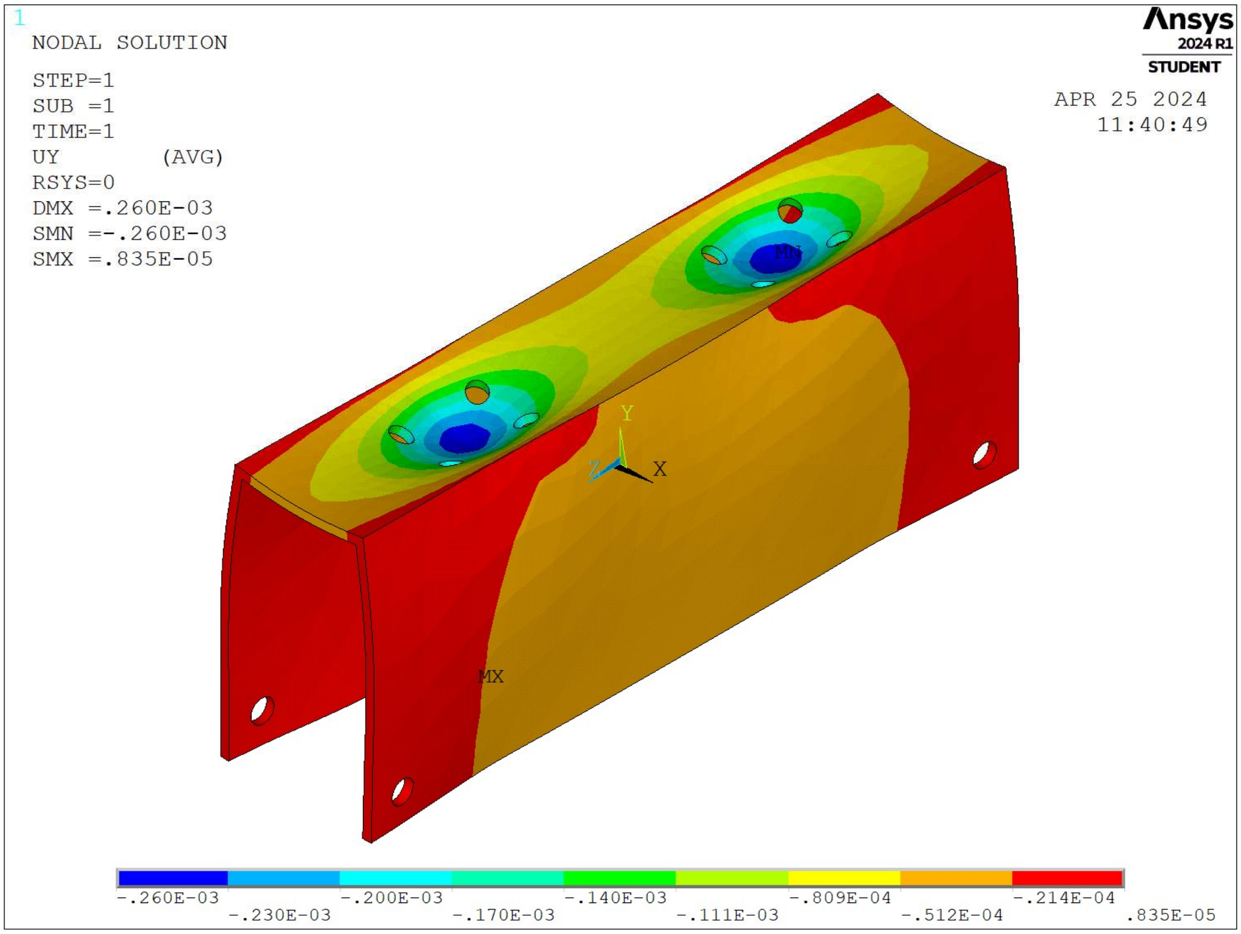

Figure 25: Contour plot showing deformation in the Y-direction of the truss retrieval cart body.

2.4. Results of Design Study

The purpose of the work described above was to find a solution to install CRPs in the cryostat at the Long Baseline Neutrino Facility. This required engineering a complex system including a truss to support CRPs, pneumatics to lift and lower the truss, rolling carts to carry the truss, and a rail platform for the rolling carts. This design is complete, and workable but does have drawbacks.

The system overall is expensive with the truss members themselves contributing significantly to the cost. The pneumatics and rails create hazards which need to be avoided by crews working on the CRP. This system with all its components now takes significantly more time than using the truss alone for ProtoDUNE. The goal is to install 4 CRPs every three days, so the speed and ease of each CRP installation is important.

To work at this pace, more than one of these systems may be needed which further increases cost. Because of these drawbacks, and other factors outside the scope of the document, it was decided that installing CRUs individually should be considered.

3. Installation of CRU in the Vertical Drift Detector

3.1. CRU Installation Introduction and Design

Changing to a CRU based installation approach changes several parameters by itself. One of these is the obvious doubling of the number of installation positions, increasing to 160 from 80. To maintain stability, each CRU will still be supported using four feet. This then also doubles the number of feet from 320 to 640. If the design of the supports stays the same, the cost of the bottom support system would also double. This motivated a push to reduce the cost and complexity of the feet. The condition which led to such a complex system is the no-slip along the floor. This requirement has been relaxed, and the bottom support is allowed to slide along the surface of the membrane floor. However, this does not mean that the CRU should be entirely free to move about when the cryostat and CRU undergo thermal contraction.

3.1.1. Bottom Support Feet Design

To maintain authority of the final position of the CRU, one of the four feet should have a higher static coefficient of fiction (COF). Friction is a property specific to the two surfaces in contact, with many factors influencing the value of the coefficient of friction. Factors like temperature and the presence of a liquid cryogen, such as liquid argon, can influence the COF. Fortunately, as part of the original design of the bottom support, Joshua Truchon conducted tests using sheet stainless steel like that of the membrane floor and the old bottom support design while submerged in liquid nitrogen at 77 K. Truchon found that the COF between the stainless-steel sheet and machined stainless steel was 0.2. The COF between the sheet and machined aluminum is reported as 0.34. Truchon also reported standard deviations for the data, which allows for the plotting of the probability distribution in Figure 26 [14]. The plot shows that the two have distinct enough COF such that the aluminum support will always have the highest COF.

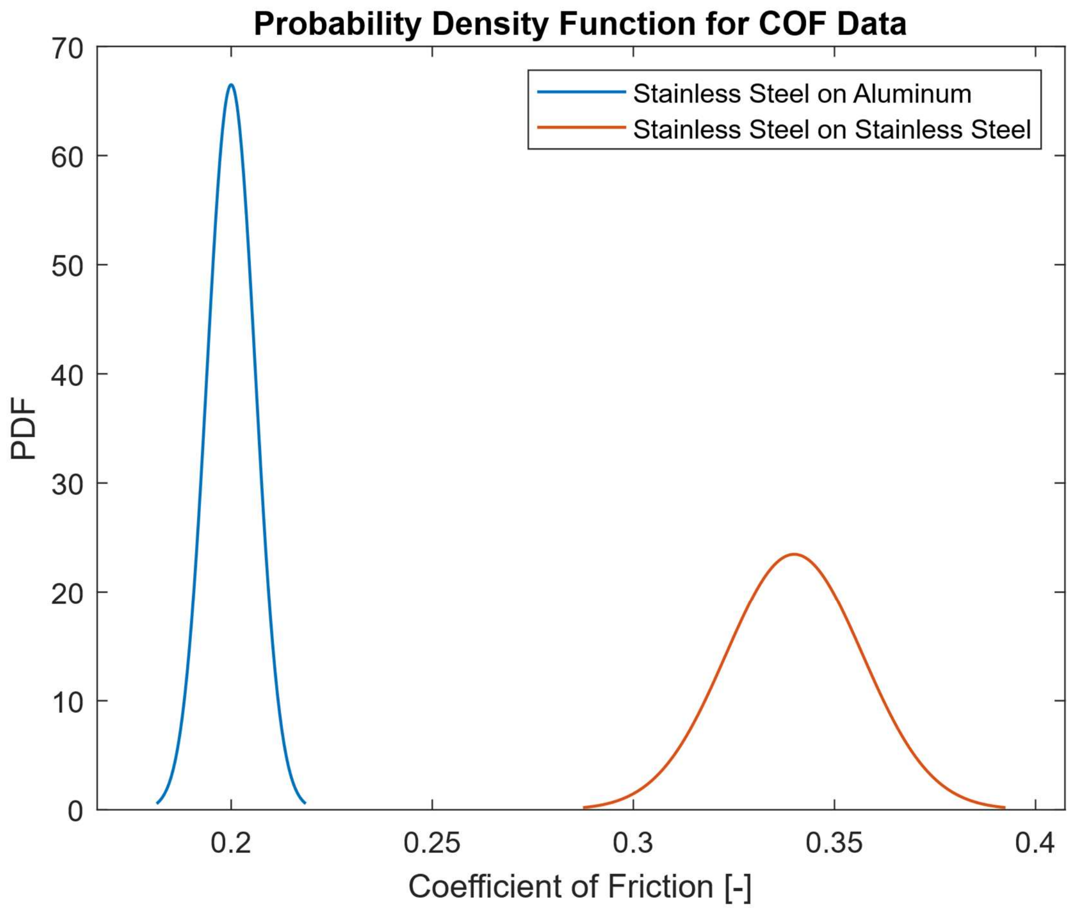

Figure 26: A plot showing the probability distribution of the COF for machined supports made from stainless steel and aluminum against stainless steel sheet metal. The data is obtained from Truchon [14].

Informed by this data, the bottom support feet will be made with removable contact surfaces made from either aluminum or stainless steel depending on the requirements of each CRU. Another consequence of the increased number of installations is the increased number of positions. As with the CRP installation, each foot position is carefully considered to be compatible with the membrane floor by avoiding the corrugations and weld seams between sections of the floor panel. This introduces new foot positions which need to be accommodated by the adapter plate.

3.1.2. Adapter Plate Design and Material Selection Introduction

As part of the change to installing CRUs rather than CRPs, the adapter plate design requirements change. Each adapter plate now needs to hold two bottom support feet rather than one. This combined with the increased number of foot positions forces the adapter plate to become larger. There was also concern from collaborators that the earlier adapter plate design would problematically impede argon flow during the filling of the cryostat. Additionally, there is a desire to minimize the cost of each adapter plate as the installation requires 320 plates.

Earlier designs were manufactured from sheets of G-10, a woven fiberglass composite material commonly used in electronics. Argon flow was enabled by CNC drilling many small holes into the G-10. Drilling G-10 is difficult and expensive as the glass fibers are hard and damage tooling. To increase argon flow without drilling more holes and driving the cost up, pockets which can be machined using a router or vertical mill are used instead of drilling. This new geometry can be made using laser cutting or waterjet cutting.

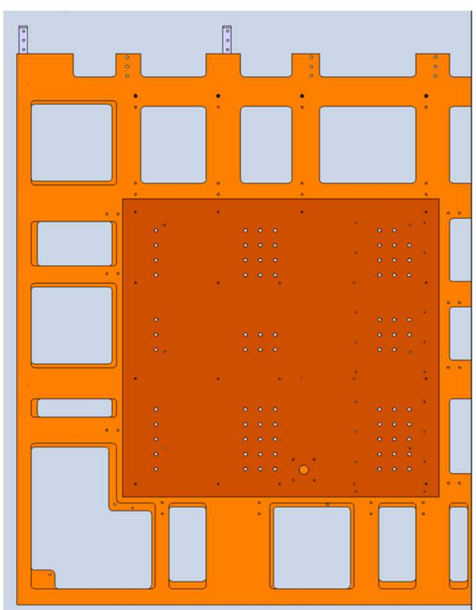

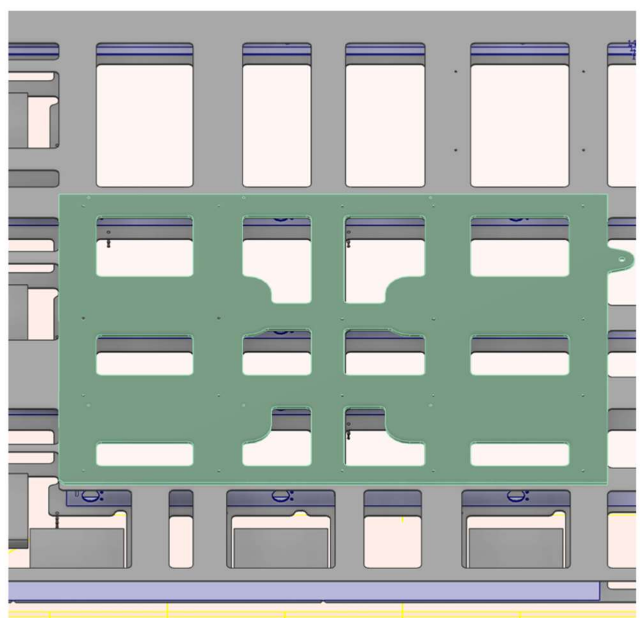

Figure 27: Comparison of CRP adapter plate (left) and CRU adapter plate design (right).

However, G-10 is not suitable for processes other than machining such as waterjet cutting or laser cutting due to issues with delamination. Because G-10 cannot be waterjet or laser cut, other materials are considered. Any selected material should have a similar secant coefficient of thermal contraction (SCTE) over the temperature range 87-293.15 K to that of the CRU composite layup, which has been measured by colleagues at the Aneccy Particle Physics Laboratory (called LAPP) as 12E-6 1/K with 10% uncertainty [15]. This requirement is to limit the mechanical stress that the CRU composite will experience. Differential thermal contraction between two surfaces attached to each other causes stress build up as a material is not able to relieve the strain through deformation alone.

To compare materials data from the NIST Cryogenic Materials Database is used. [16] Much of the data is provided as non-dimensional linear expansion data, which is calculated by comparing the length of a sample at a given temperature, L(T) to its original length L_0. This difference in length is the thermal strain ε_t. The thermal strain is equal to the SCTE, $\overline{\alpha}$, multiplied by the difference in temperature. After comparing calculated SCTE values for multiple materials, the only materials with similar SCTE to the CRU are G-10 and stainless steel. [17], [18] The SCTE for G-10 between 87 K and 293.15 K is 9.85E-6 1/K, and the SCTE for 304 stainless steel is 13.2 1/K. Stainless-steel's SCTE is a closer match to the CRU than G-10, but both still require interfaces to be engineered to account for the thermal contraction, and both can be accommodated.

$$\varepsilon_t = \frac{L(T) - L_0}{L_0} \tag{3}$$

$$\varepsilon_t = \overline{\alpha}(T_2 - T_1) \tag{4}$$

Since the contraction of both can be accommodated, cost and weight will be the determining factors between these materials. The weight of the adapter plate is relevant as it impacts the weight which needs to be supported by installation tools and machinery, with a lower weight being preferable. Several quotes were obtained for the cost of manufacturing the adapter plates. The stainless-steel adapter plate was quoted with two different thicknesses and manufacturing processes. The two thicknesses were ¼" and 3/16". The ¼" could only be waterjet cut, while the thinner 3/16” could be waterjet cut, or laser cut. G-10 could only be cut using a CNC router. The weight of each component is easily calculated by multiplying the volume of the adapter plate, given by CAD software, and the densities of G-10 and stainless steel. The G-10 was both the cheapest, and the lightest and was therefore selected.

Table 1: Cost and Mass Comparison of Adapter Plate Material Candidates

Stock Material & Process	Piece Manufacturing Cost	Mass	Selected
¼” G-10 – CNC Router	$424.15	17.2 kg	✓
¼” 304 Stainless – Waterjet Cut	$852.03	70.54 kg	
3/16” 304 Stainless – Waterjet Cut	$737.06	52.91 kg	
3/16” 304 Stainless – Laser Cut	$511.52	52.91 kg	

3.2. Development of a Detailed Finite Element Model (FEM) for the CRU

To validate the adapter plate design, a finite element model is created. The model is created using ANSYS Mechanical 2023 R2. To create the model, the geometry of the CRU is imported from a CAD system as a STEP file which can be modified or simplified using ANSYS SpaceClaim. Some of the geometry is simplified to speed calculation.

3.2.1. CRU FEM Geometry Simplification

Several components of the CRU 3D model are modified to improve calculation efficiency. The anodes are represented by 2D surfaces whose stresses are calculated using shell elements, and the many small holes for argon flow are removed. To compensate for this simplification, the material properties of the anodes are modified, where the density and modulus of elasticity are lowered.

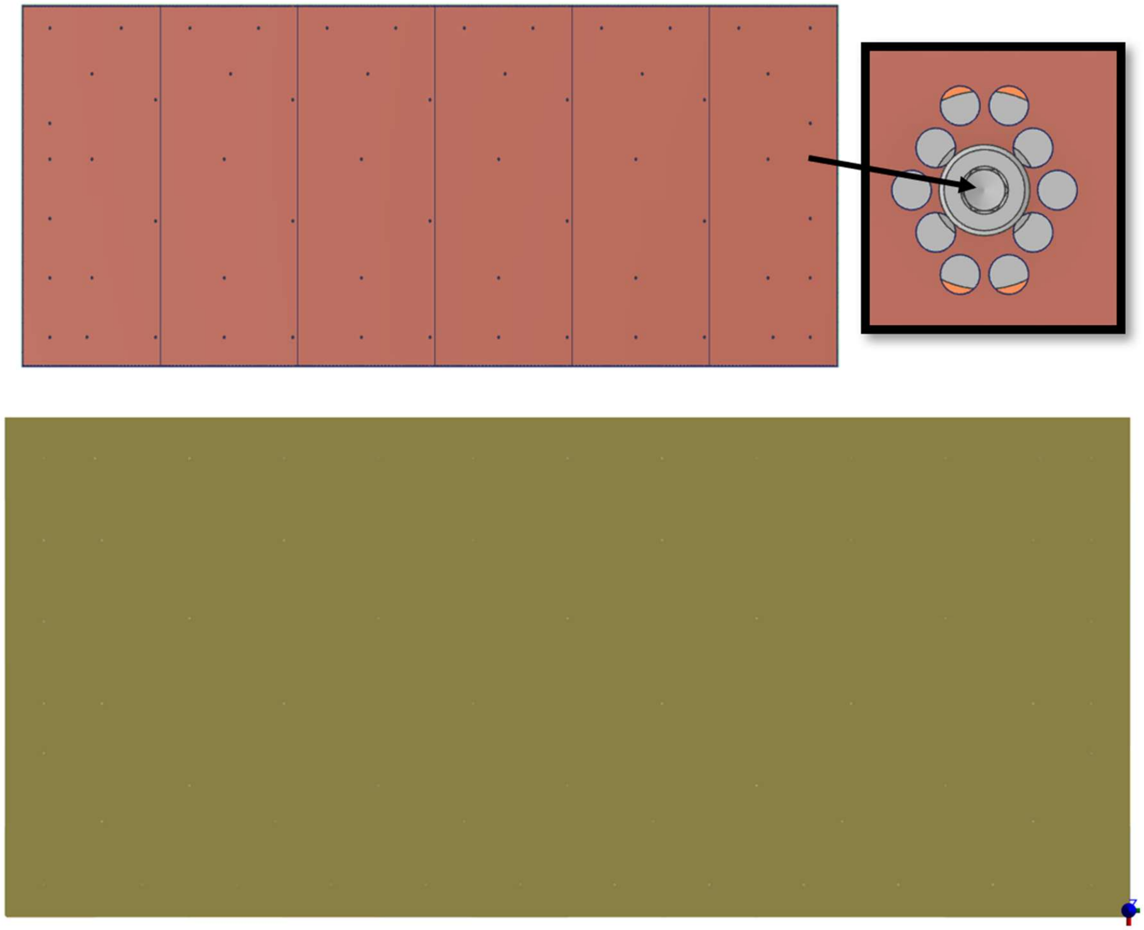

Figure 28: A figure of the anodes showing the structural holes for the PEEK fasteners above, and the simplification. Note that the argon flow holes are not shown in either view.

The BDE adapter boards are unified into a single surface and modelled as shells, with holes removed. This reduces the number of contacts within the model, as contact formulation and implementation are computationally expensive.

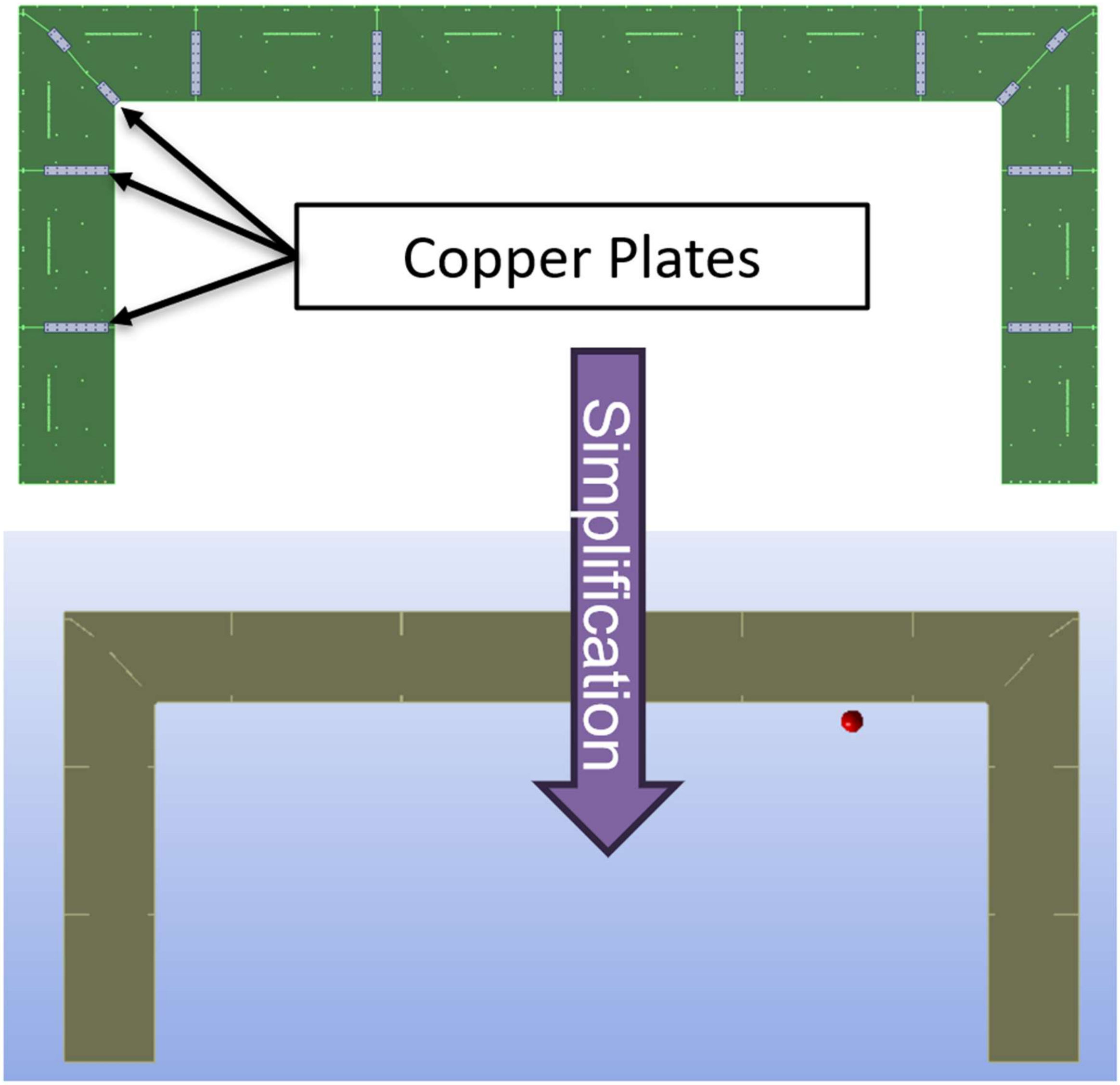

Figure 29: Diagram showing the real BDE geometry, and the simplified geometry for the FEM.

Small features such as rivet nuts, and small non-structural holes are removed from the composite skins. Additionally, the mass of patch panels, 1.5 kg each, the hanging mass of cables which connect to these patch panels, 2 kg per patch panel, are added as two-point masses scoped to the lower composite skin. Lastly, the mass of cables which connect to the front-end motherboards (FEMBs) are modeled as a distributed mass which is equally distributed across the bottom surface of the upper composite skin.

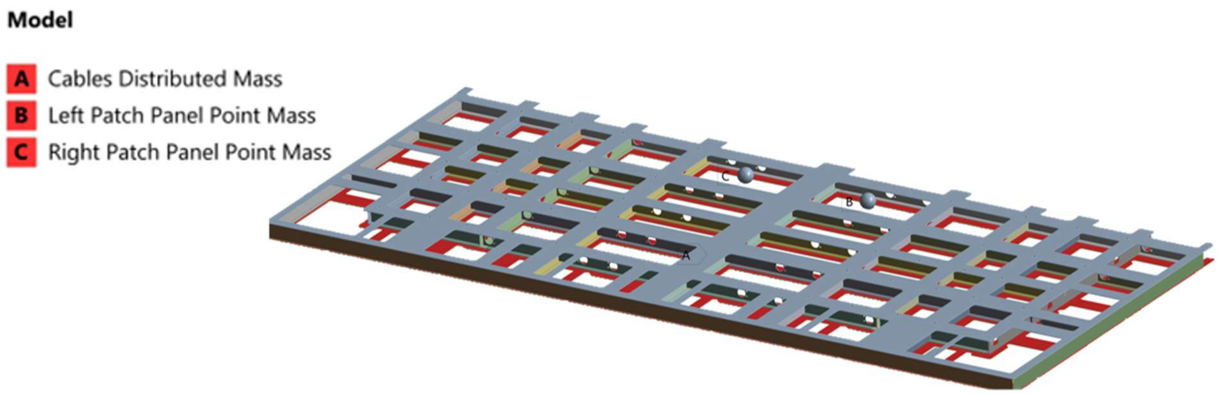

Figure 30: Diagram showing the simplified geometry for the composite superstructure, and mass elements scoped to it.

The FEMBs are modelled as rectangular boxes with a density calculated to so that the mass is that of the real part. The boxes are large enough that the spacers which suspend them from the BDE can be in their real locations so that the mass can be distributed to the BDE correctly. These spacers are modelled as simple cylinders with the nominal diameter of the hardware.

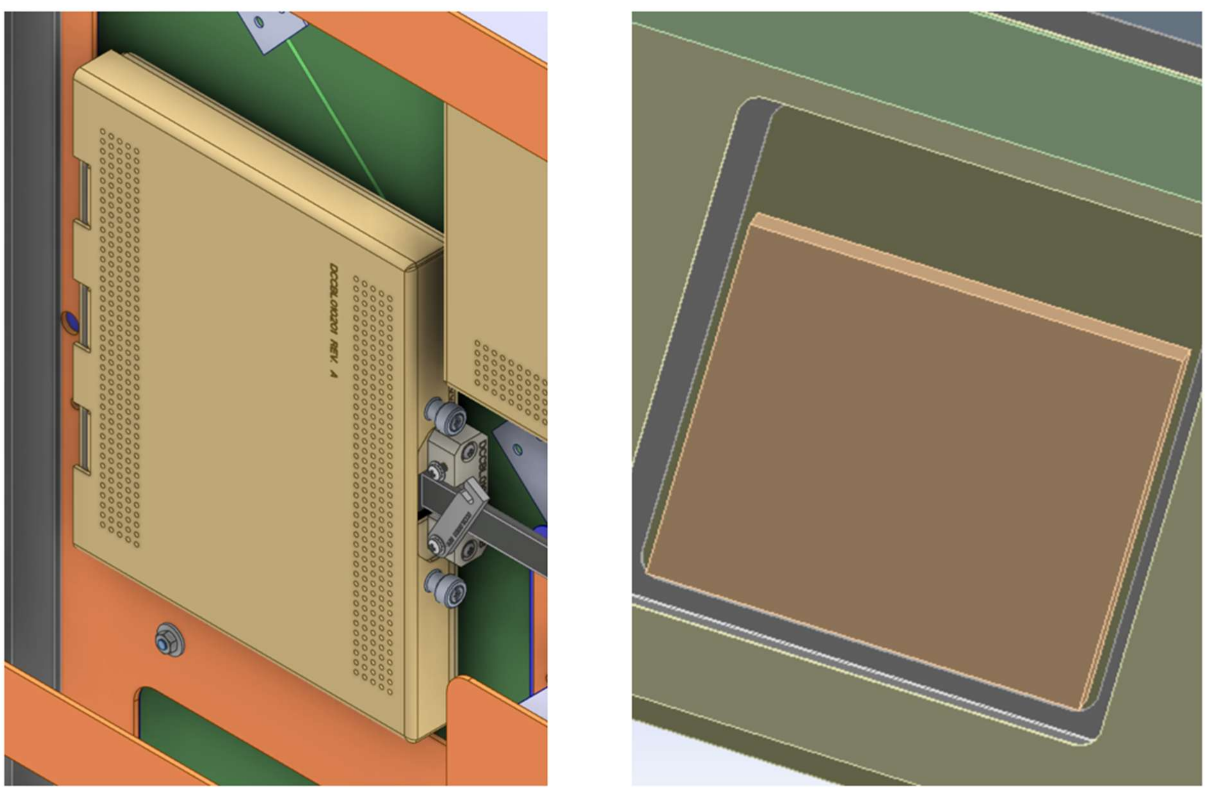

Figure 31: Diagram of realistic FEMB geometry (left), and the simplified geometry used in the FEM (right).

The anode spacers are handled differently. The anode spacers are simplified into 1D line bodies, which are simulated using beam elements. The beam elements follow Timoshenko beam theory, which is a first order model. The ANSYS software discretizes the total spacer into many small beam elements connected to each other at ends to capture any non-linear behavior. The beams are defined with circular cross sections which correspond to the shoulder diameter of the real spacer, that is 6.3 mm for the sections between the composite skin, through to the bottom anode, and 5.5mm for the section spanning the bottom anode to the top anode.

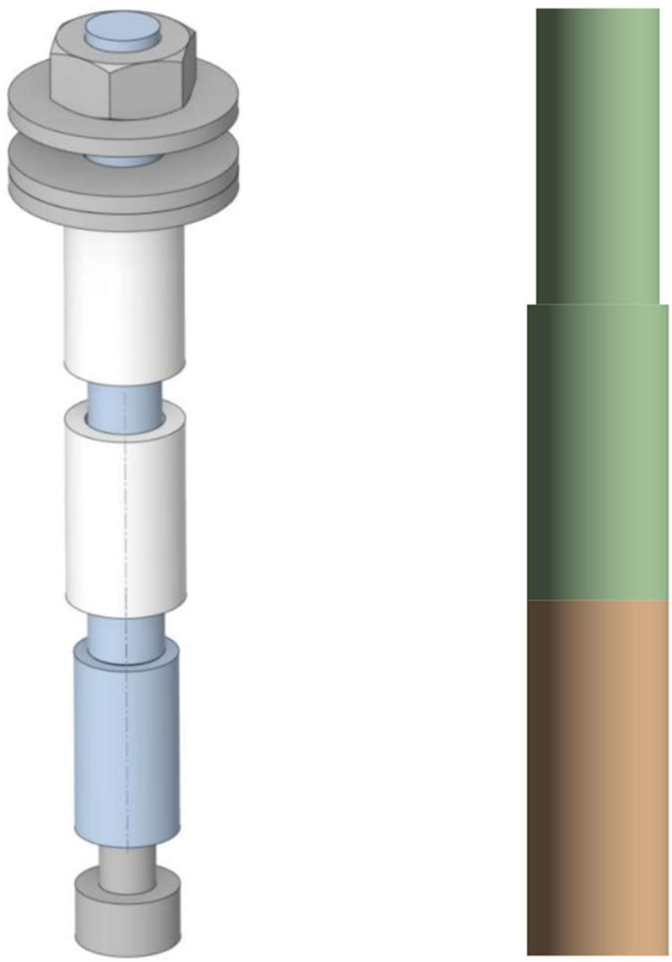

Figure 32: The PEEK fasteners used to position the anodes. The left is a 3D CAD model with the threads removed. The right is the simplified version for the FEM.

Finally, the bottom supports which incorporate a levelling mechanism, spherical joint, and an argon gas relief port have been simplified. All mechanisms are removed, and replaced with solid material, and the gas relief port is filled in as well. Analyzing the feet in detail is not a primary objective of this model, this can be done better with a more specific model, instead the feet are present to provide a reasonable support condition which includes the effect of the CRU being some distance above the floor.

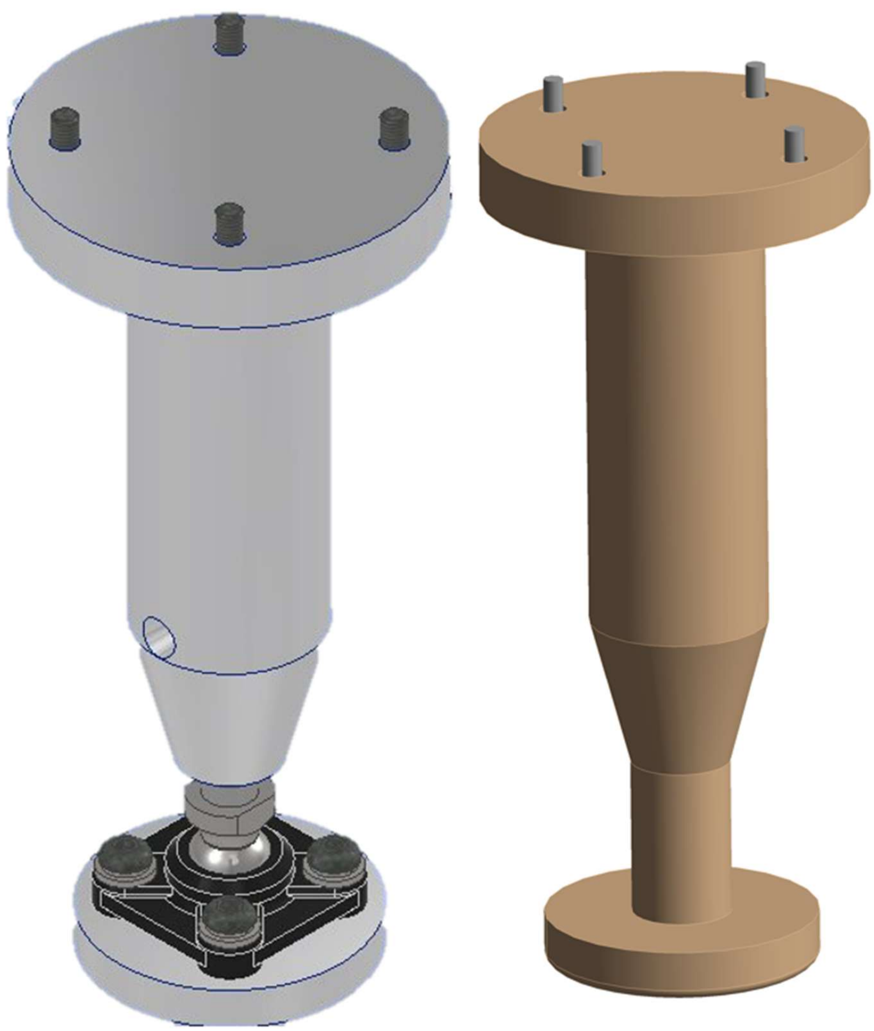

Figure 33: The new bottom support design, with the detailed CAD model on the left, and the simplified version used in the FEM on the right.

3.2.2. CRU FEM Material Models

Beyond geometry, material properties and models are established. For the FEM of the entire CRU, a linear elastic model describes all materials. A linear elastic model deforms elastically with applied load, following Young's modulus with no non-linear effects like yielding. Most materials do have a linear elastic region, and this type of model is sufficient if material yielding would be considered failure. The requirements set by the DUNE compliance office do not permit yielding, so this type of model is sufficient. An ANSYS model for the CRP was developed by Sebastien Canva at LAPP. In this model, the materials were treated as linear elastic. For the CRU model, the same mechanical material properties are used. The material properties are tabulated below. For G-10 the data used is obtained from Matweb. Data for copper is obtained from three sources, the ANSYS Granta Database, Matweb and the NIST Cryogenic Materials Library. [19], [20], [21]

Table 2: Baseline material properties used in analysis, sourced from LAPP CRP FEM documentation, NIST, Matweb and ANSYS Granta Design.

Component	Material	Density [kg/m^3]	Poisson's Ratio	Young's Modulus [MPa]	Secant CTE [1/K]	Yield Strength
Composite Skin	Woven Fiberglass Composite	1904	0.3065	13,000	1.20E-05	205
Beams	Quasi-Isotropic Fiberglass Composite	1845.5	0.1543	13,000	1.20E-05	250
BDE Adapter Board	PCB	1845.5	0.1543	24,000	1.20E-05	440.1
Anodes	PCB	804	0.1543	10,250	1.20E-05	440.1
Spacers	PEEK	1310	0.4	3,850	5.48E-05	90.9
G-10 Adapter Plate	G-10	1845.5	0.11	18,500	0.985E-05	375
BDE Link Plates	C10100 Copper, H0 Temper (Oxygen Free Electronic)	8942	0.345	126,000	1.44E-05	195
Fasteners	Stainless Steel, 316	7967	0.27	195,000	1.388E-05	250

The Young's modulus of most materials varies with temperature, typically decreasing with increasing temperatures and vice versa. The changes are usually small enough to be considered negligible. However, for many polymers this is not true, and the changes are significant. PEEK exhibits significant stiffening with temperature, increasing its modulus to 6,100 MPa at 77 K according to Zhang and Hartwig. [22] This value is added to the material model of PEEK in the FE models as another data point. The solver will linearly interpolate the Young's modulus at 87 K. This is acceptable, as the data gathered by Zhang and Hartwig shows that the stiffening of PEEK is a linear phenomenon.

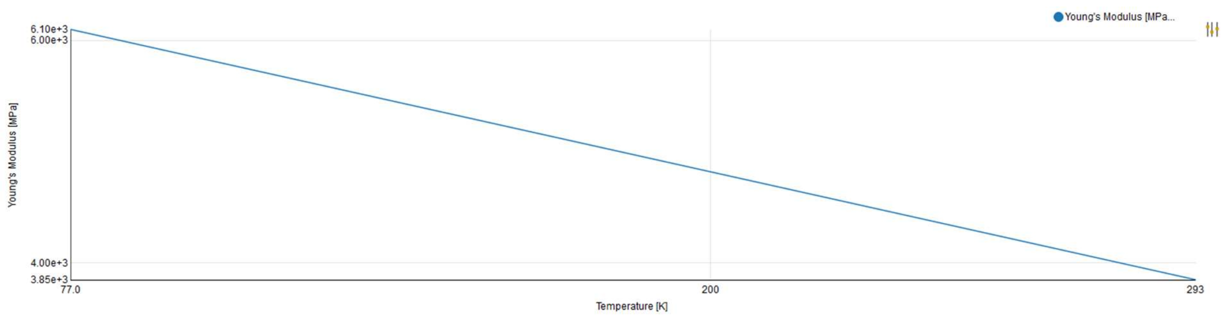

Temperature [K]	Young'S Modulus [M Pa]	Poisson'S Ratio	Bulk Modulus [M Pa]	Shear Modulus [M Pa]
77	6100	0.4	10167	2178.6
293.15	3850	0.4	6416.7	1375

Figure 34: Young's Modulus of PEEK vs Temperature, plotted within ANSYS.

3.2.3. CRU FEM Connection Types

Beyond defining the material properties of each component of the CRU, the connections between the various components need to be captured by the model as well. Within the ANSYS environment there are many options for these connections. Connections can be defined as joints or contacts, with each category having further options, or can be attached together using a beam. For most of the connections in the CRU, the bonded contact connection is used. This option transmits all forces between contacting surfaces, like a weld in a real structure would. The CRU structural components such as the beams and composite skin are adhesively bonded together, which makes the bonded contact the most appropriate choice. For bolted components, this behavior type is not accurate but models a case where the stiffness of the joint is high, likely much higher than the real bolted connection. This can be useful to provide an upper bound on the stiffness of the joint, but it is best avoided. An example of a bonded contact connection type is shown in Figure 35. Bonded contact is also used to establish connections between the 1D beam elements and the shell elements for the PCBs, where the end of each beam is bonded to circular edges on each PCB with the same diameter as the spacer shoulders.

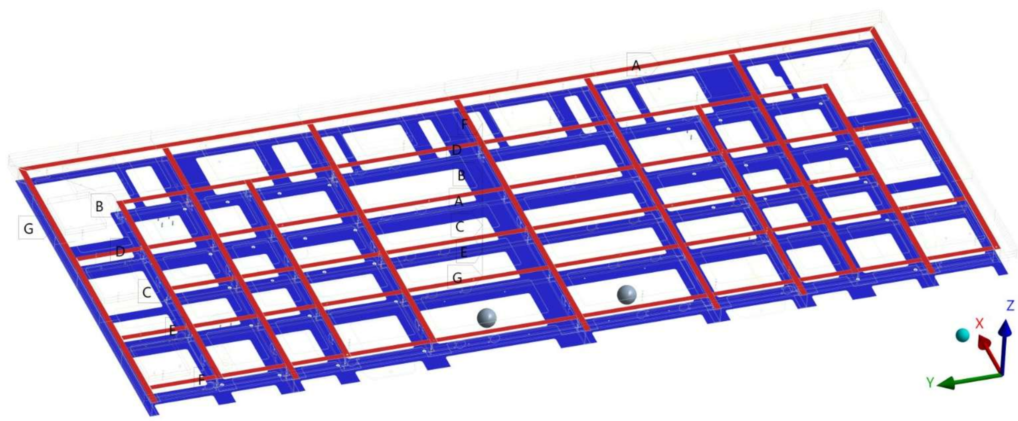

Figure 35: Bonded contact between a beam in the CRU structure and the composite skin of the CRU structure. These components are held together with adhesive on these surfaces during assembly, hence the use of the bonded contact. The beam is the contact, so it is checked against the composite skin for penetration.

In a model which captures the frictional sliding behavior of the CRU along the membrane floor by using simplified geometry which has the appropriate mass and stiffness. The frictional contact type is used. This contact type transmits all normal forces. Shear forces are transmitted up until a slip condition is determined by the coefficient of friction and normal force is met. Once the slip condition is met, the model allows the contact body to slip relative to the target body, until the shear forces reach equilibrium at a value below the slip condition. This contact formulation is non-linear and requires solver iteration, which is why it is omitted from the larger CRU model. The coefficient of friction applied to the model is user definable, and this model uses the values from Truchon. [14] Figure 36 shows a view of the mock CRU and the contact regions which capture the interaction between the membrane floor and the bottom supports.

Figure 36: Diagram showing the mock CRU and the frictional contact regions which capture interactions between the membrane floor and the CRU bottom supports.

One of these contact regions will act as the pseudo fixed support, where the bottom support interface material is aluminum, increasing the coefficient of friction from 0.2 to 0.34. Which support will have this increased COF will depend on the position of CRU within the cryostat. For this model, the contact region labelled C is treated as the pseudo fixed support.

Table 3: Coefficient of friction applied to contact regions in Figure 36.

Label	Assigned Coefficient of Friction	Material Interface Modelled
A	0.2	Stainless-Stainless
B	0.2	Stainless-Stainless
C	0.34	Aluminum-Stainless
D	0.2	Stainless-Stainless

For some of the bolted connections within the CRU a beam connection type is used. The beam connection type behaves differently to the bonded and frictional connections used elsewhere in the model. The construction of this connection is as follows. First, two areas (or edges, but areas are generally a better choice), are selected. One of these areas will be treated as the reference area, while the other is called the mobile area. At the centroids of these areas the program creates remote points. Remote points are like nodes, but are not associated with any material or geometry, but have degrees of freedom which can be used to write constraint equations. The software then writes constrain equations that connect the nodes in the areas to the correct remote point. The user can control the behavior of the remote point. By default, this is set to deformable, which allows the remote point to move with the geometry as it undergoes deformation. This is the most accurate method, but is more computationally expensive than rigid behavior, which keeps the remote point fixed in space. All beam connections use deformable behavior in this model. The software then generates 1D beam elements between these remote points to capture the stiffness of the bolt. The user chooses which area is the reference and which is considered mobile. The relative motion of the mobile area compared to the reference is used to calculate the beam behavior. Generally, the reference should be the area on the stiffer body. There are 46 beam connections which connect the composite superstructure to the adapter plates, and 16 beam connections which connect the bottom supports to the adapter plates.

To better understand the behavior of these beam connections, let us use an example. This example shows a beam connection which models a bolt between the adapter plate and the CRU composite structure. The composite structure is shown in blue, and the adapter plate in green. In a load step of this analysis, all bodies will experience a change in temperature from room temperature to liquid argon temperature. There will be significant deformation due to this thermal contraction, much greater than any due to mechanical loading. The adapter plate will contract less over the same length due to G-10's lower CTE, so the area on the adapter plate is considered the reference shown in red. The CRU area is therefore the mobile area, colored blue in Figure 37.

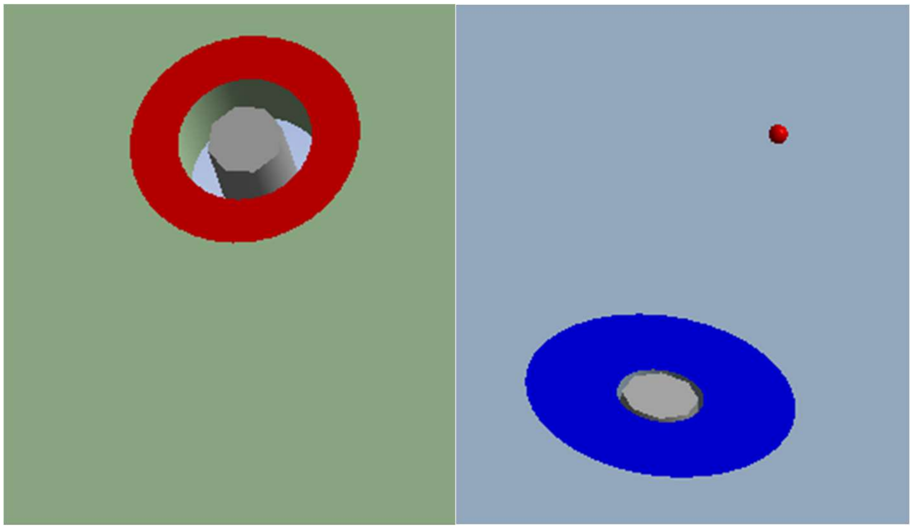

Figure 37: Close view of a beam connection modelling a bolted joint between the adapter plate (green) and the CRU structure (blue). The adapter plate undergoes less thermal deformation, so this area is the reference (red).

The connection type used in the model is the fixed joint connection. This connection type creates remote points at the centroid of the selected entities, and similar to the beam connection type defines one as the reference and the other as the mobile. The fixed joint does not allow for any degrees of freedom between the remote points. The mobile point must follow the motion of the reference, and this is enforced using constrain equations. This connection is used between the composite skin, and the anode spacer line bodies. In this case, the vertex of the line body is considered the mobile entity, and so a remote point is created there. The area underneath the shoulder of spacer on the composite skin is the reference area, and a remote point is created at this centroid. These remote points are coincident but scoped to these two different bodies. The nodes which have constraint equations scoped to them have lines drawn to them in Figure 38, notice how all the lines draw to the center of the line body.

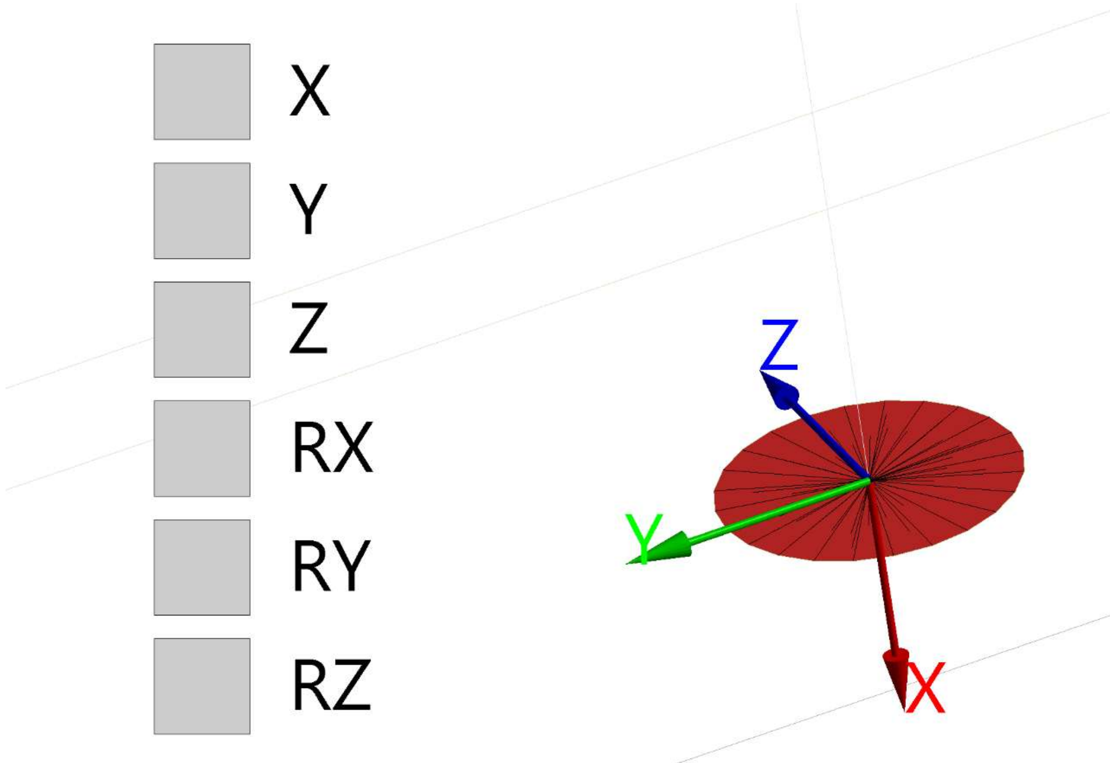

Figure 38: Fixed Joint Constraint Equation Example

3.3. Load Cases for the CRU FEM

With geometry, material models, and connections defined, loads and boundary conditions can now be applied to the model. Beginning with the CRU after it is placed in the cryostat, there are three load steps to consider. The first step is just the CRU resting on the bottom support design at near room temperature conditions and loaded by its own weight. The next step captures the effects of the cryostat filling process. The liquid argon will be pumped into the cryostat, where upon entering near the membrane floor it will expand into a gas. This will happen over a considerable time due to the large volume of the cryostat and the fill rate. This will effectively precool the CRU to near liquid argon temperature before it is submerged. So, in this case, the CRU experiences thermal loading, but no buoyancy. This load step is the most extreme loading within the cryostat. The last step is the long-term loading of the CRU while it is submerged within liquid argon. This step is like the preceding, but now buoyant forces are applied.

3.3.1. Detailed Description of Load Step 1

The first load step in the analysis is the case where the CRU has been placed into position with some installation tooling already. The CRU is now resting on the bottom supports at room temperature. To define this load case, three of the feet are selected to be considered the low coefficient of friction feet (or free feet), and one other is the 'fixed' foot. The fixed foot receives the fixed support boundary condition on the surface in contract with the membrane floor. This fixed support prevents node displacement and rotation at all nodes on the face. This face is has label A in Figure 39. The other three supports are assigned frictionless support, which constrains all nodes on the surface to have zero vertical displacement, but all other degrees of freedom are free. This mimics the behavior of the real support without using non-linear contacts, which speeds the model and allows for more complex geometry to be used.

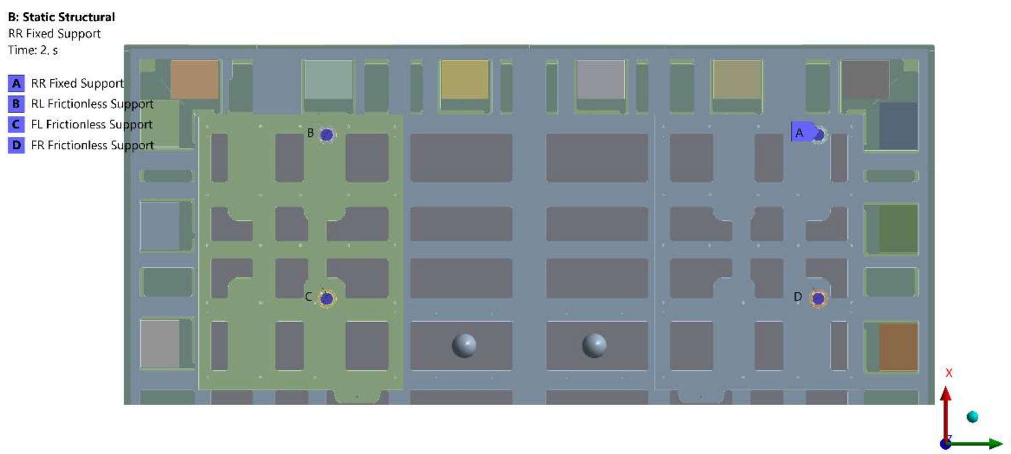

Figure 39: The support boundary conditions for the model. The right rear support (label A) is treated as fixed, with a DOF 0, and labels B, C, and D are given frictionless, with all DOF except vertical displacement.

For this load step, gravity is the only external load on the model. To apply gravity, the ANSYS standard earth gravity load is assigned. This load is an inertial load, which has the reference frame accelerating around the body to keep the problem static. This load captures the effects of the mass distribution of the CRU, including the attached patch panels and the distributed mass of the cables for the FEMBs.

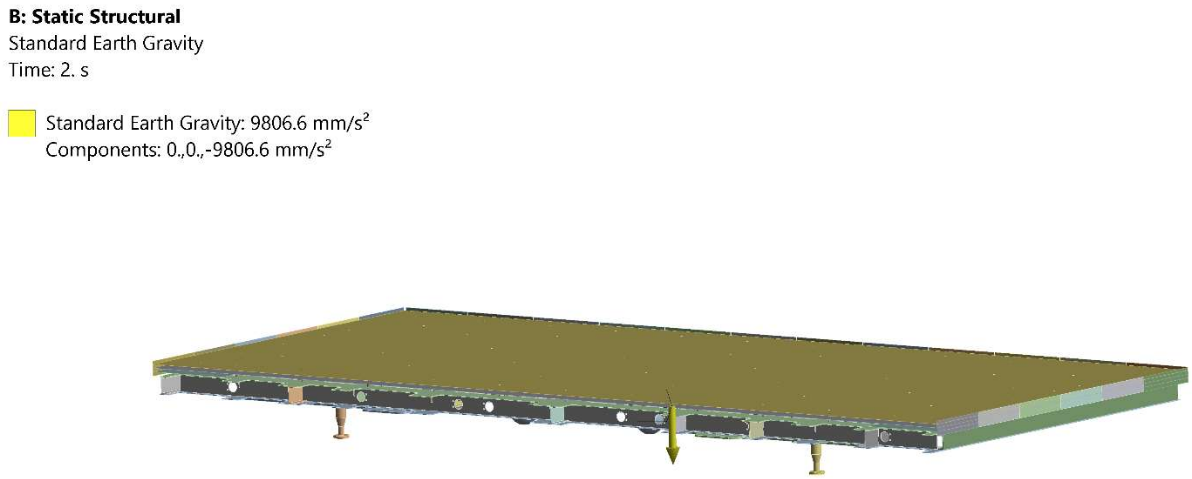

Figure 40: Gravity Inertial load applied to the CRU within ANSYS.

To fully define this load step in the analysis, one final load needs to be applied to the model, which is the pretension in the bolts. Bolt pretension has a significant impact on the stiffness of any bolted joint, so pretension forces must be applied to the beam connections to create an accurate finite element model. The bolt pretension can be assigned to a beam connection using the bolt pretension object under loads in ANSYS Mechanical. To find the proper pretension in the bolt, the joint needs to be inspected. A diagram of the joint is shown in Figure 41. The head of the bolt is in contact with a spring washer, which rests upon a fender washer to distribute the load over a larger area. The spring washer's purpose is to maintain preload on the bolt, even after the thermal contraction has occurred.

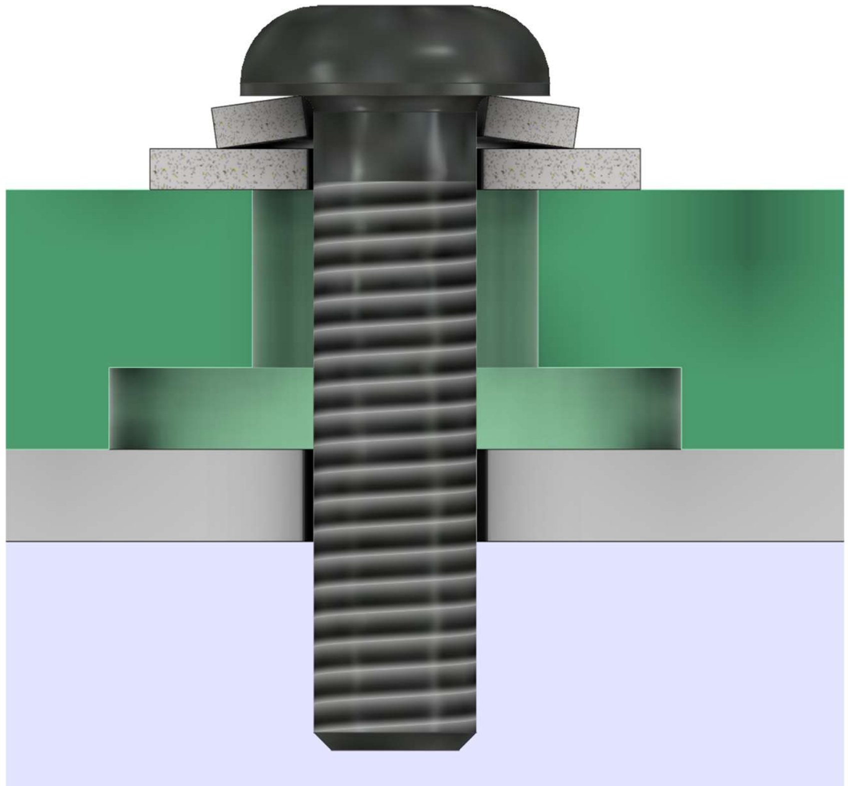

Figure 41: 3D model bolted joint between CRU and adapter plate. Note the belleville washer and fender washer.

Typically, the preload applied to the bolt is between 75% and 90% of the proof strength, which is determined by the material's yield strength. For this joint, 75% is chosen as the compliance office typically considers yielding failure. [23]. As part of the design of the CRU, all fasteners must be made from stainless steel. The rivet nuts placed in the CRU use typical metric M4 threads and are stainless steel. Stainless steel metric fasteners are rated using a two-part system, where the first part being either A2 or A4, which denotes the alloy of stainless steel to be used, with the codes corresponding to AISI 304 and AISI 316, respectively. The second part of the system is called the property class and is numbered corresponding to the tensile strength of the fastener, for example a property class of 50 corresponds to a tensile strength of 500 MPa. The most common stainless steel M4 fastener sold in the U.S is an A2-70 type fastener, which has a yield strength of 450 MPa. [24]

Table 4: Tensile and Yield Strengths for metric stainless steel fasteners by property class.

Property Class	Tensile Strength [MPa]	Yield Strength [MPa]
50	500	210
70	700	450
80	800	600
100	1,000	800

The proof strength of metric stainless steel fasteners is just the yield stress. Multiplying this stress by 75% and dividing by the stress area of an M4 bolt, which is 8.78 mm^2, the desired preload force is then 2963 N. [23] To check whether is amount of preload is sufficient, the change in thickness of the adapter plate is calculated.

The expansion of G-10 in the direction of the thickness is different than the in-plane expansion. This data is also collected by NIST, and this value is -6.256 mm/m. Stainless steel is isotropic, so the CTE is the same as in Table 2. [17], [18] Since both the rivet nut and bolt are made of stainless steel, their contraction is the same, so the only relevant length is the thickness of the adapter plate, which is 6.35 mm. The adapter plate shrinks 0.02243 mm more than the stainless-steel bolt. This is also the amount of relaxation in the DIN spring washer.

To find the residual bolt tension, the spring force of the washer is needed. The first step is to determine the deformation of the washer at the initial tension of 2963 N. The behavior of spring washers has been studied, with multiple models being presented. The most complete model at the time of writing is by Mastricola and Singh. Their model builds on the work of Almen and Laszlo by adding terms that account for the friction between the contacting surfaces and edges of the spring washers as shown in equation 6. In addition, the Almen and Laszlo expression was simplified by Curti et al to the form in equation 5. The expression accounts for the geometry of different washers, the coefficient of friction, and the Young's modulus of the washer material. [25] In these calculations the two coefficients of friction are equal and take a value of 0.2 based on Truchon's testing of stainless-steel frictional contact. [14] According to Matweb, the Young's modulus for AISI 304 and AISI 316 is 193 GPa [26], [27].

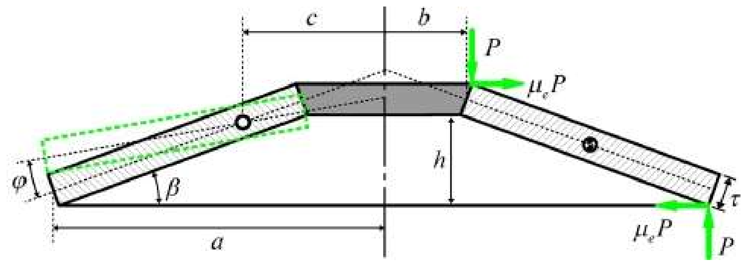

Figure 42: Geometry needed to determine spring washer deformation. All parameters are labelled.

$$P_{L2}(\delta) = \frac{E\delta\pi}{a^2}\left(\frac{\alpha}{\alpha-1}\right)^2\left[(h-\delta)\left(h-\frac{\delta}{2}\right)\left(\frac{\alpha+1}{\alpha-1}-\frac{2}{\ln\alpha}\right)\tau+\frac{\tau^3\ln\alpha}{6}\right] \tag{5}$$

$$P_F(\delta) = \frac{P_{L2}(\delta)}{1 \mp \left[\frac{\mu_e(h-\delta+\tau)+\mu_\phi\frac{\tau}{2}n_p}{a-b}\right]} \tag{6}$$

Symbol	Physical Quantity
E	Young's Modulus
a	Mid-Surface Outer Radius
b	Mid-Surface Inner Radius
α	Radius Ratio (a/b)
h	Cone Elevation (Flat to undeformed)
δ	Axial Deflection of Washer
τ	Thickness of washer
$\boldsymbol{\mu_e}$	Static Coefficient of Friction at Edge Interfaces
$\boldsymbol{\mu_\phi}$	Static Coefficient of Friction at Surface Interfaces
$\mathbf{P_{L2}}$	Force from Analytical Model not accounting for friction. Curti et al simplified form of the Almen and Laszlo expression
$\mathbf{P_F}$	Force from analytical model with frictional terms by Mastricola and Singh

Using the geometry for DIN 6796 spring washer for an M4 fastener, the Young's modulus, and the initial preload, equations 5 and 6 can be solved for the displacement, which is 0.156 mm, which is within the washer's ability to deform. Subtracting the relaxation distance from the initial compression gives 0.134 mm. Using this as the displacement in equations 5 and 6 gives a residual force of 2503 N, which is sufficient tension to keep the joint together. In our analysis, the bolt pretension for the first step is set to 2963 N and will be adjusted to 2500 N for steps 2 and 3. This concludes the loads for the first step of the analysis.

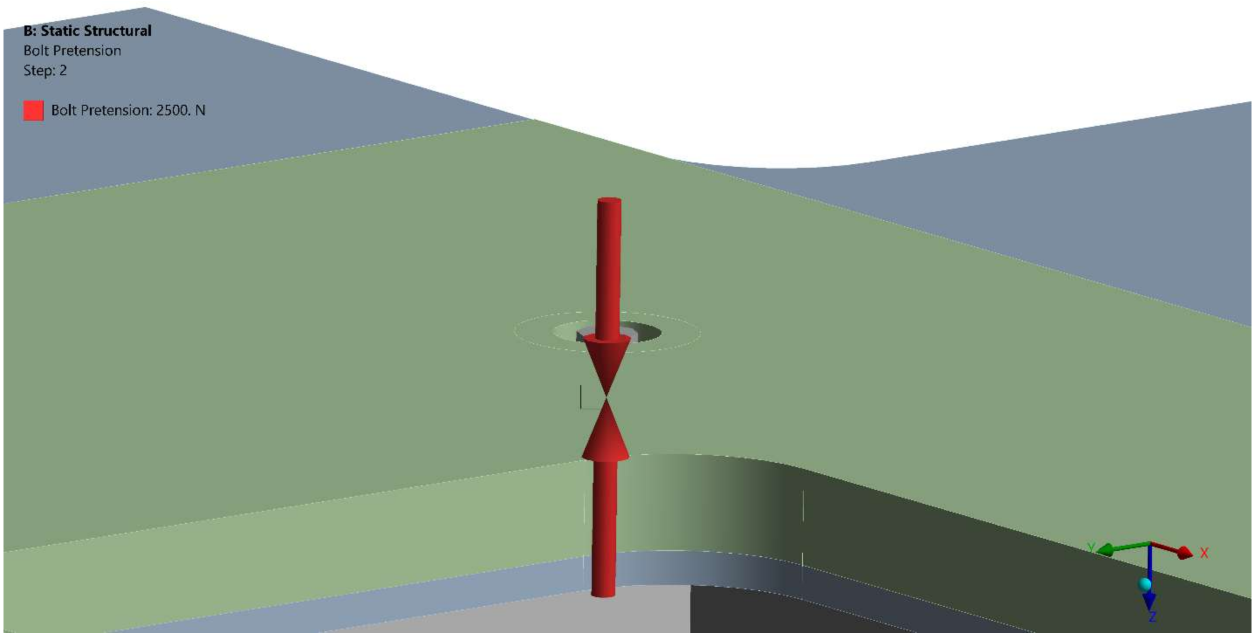

Figure 43: Example of bolt pre-tension load.

3.3.2. Detailed Description of Load Step 2

The second load step is where thermal effects are considered, but without any buoyancy effects. This represents the time when the cryostat is being filled, but the volume near the floor is occupied by cold gas, rather than liquid. In this step, the same gravity load is applied. The bolt pretension is reduced to 2500 N as found by the bolt calculations in the section above. A uniform temperature thermal condition load is applied to all bodies and surfaces in the model. This load ramps the temperature down to 87 K from the initial temperature of 293.15 K.

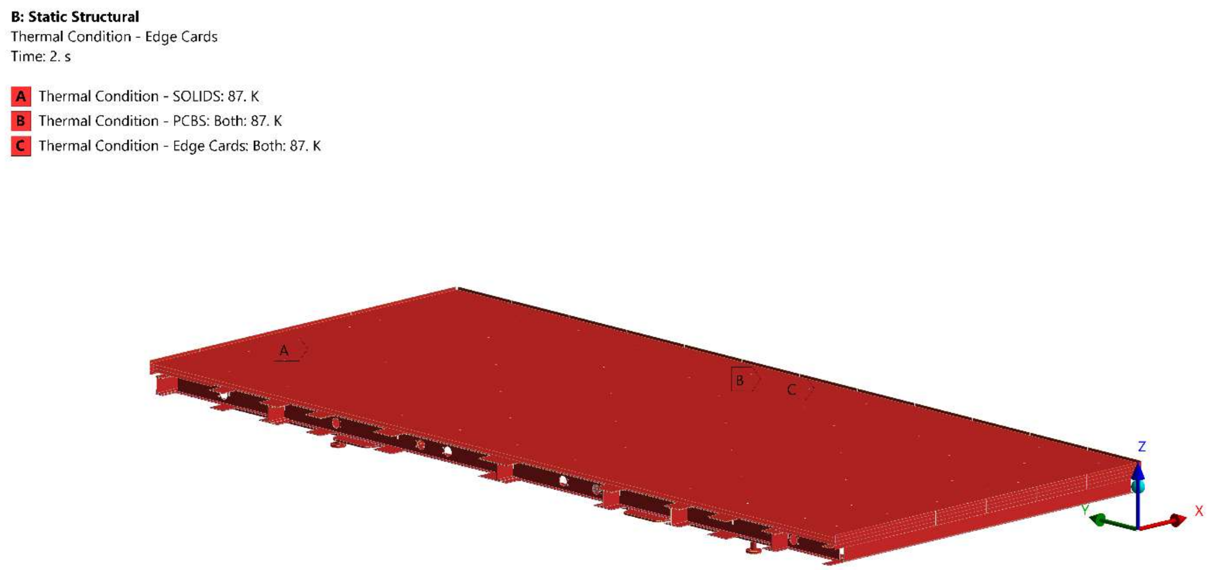

This step also includes remote forces applied to the bottom surfaces of the feet. The design of the feet has them slip along the surface of the cryostat floor during the cool down. A separate sub-model was created, with the CRU modelled as a solid rectangular prism, with the density and modulus of elasticity assigned to mimic the mass and general deformation of the CRU. Bottom supports are then bonded to this highly simplified CRU. Four surfaces coincident with the bottom of the CRU supports are created and modelled with shell elements. These surfaces are constrained with the fixed support boundary condition, so that they do not deform. Then, frictional contact is defined between these surfaces and the bottom surface of the CRU supports. The coefficient of friction for three feet is set to 0.2, while the last is set to 0.34. Then all bodies and surfaces have the same uniform temperature load as above. The forces from this sub-model are then applied to the global modal with the linear boundary conditions. This allows for the stresses due to thermal contraction to be estimated efficiently.

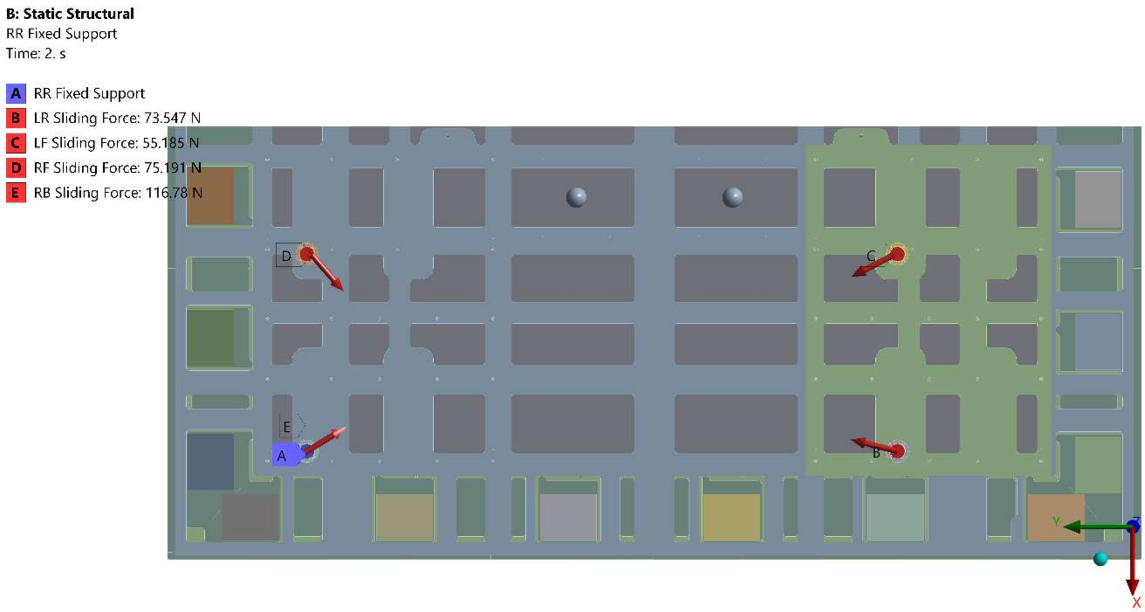

Figure 44: Sliding loads applied to load step 2 of the finite element model.

3.3.3. Detailed Description of Load Step 3

The third load step is when the CRU is in a filled cryostat. The only difference between the second and third load step is that buoyancy effects are included in the third load step. The gravity load is still present in this step, but remote forces are applied via surface effects to all surfaces facing the membrane floor that represent the buoyant force on those components. The surface effect formulation of a remote force is like applying a pressure load that redistributes based on the deformation of the body it is scoped to. The buoyant force on each component is equal to the force of gravity that would act on the same volume of liquid argon, as shown in equation (6), where F_B denotes the buoyant force, ρ_{LAr} denotes the density of liquid argon, and g is the acceleration due to gravity near earth's surface. The bolt pretension loads, and frictional loads are the same as load step 2. Figure 45 shows one of these forces in the Ansys Mechanical GUI for clarity.

$$F_B = V_c \cdot \rho_{LAr} \cdot g \tag{6}$$

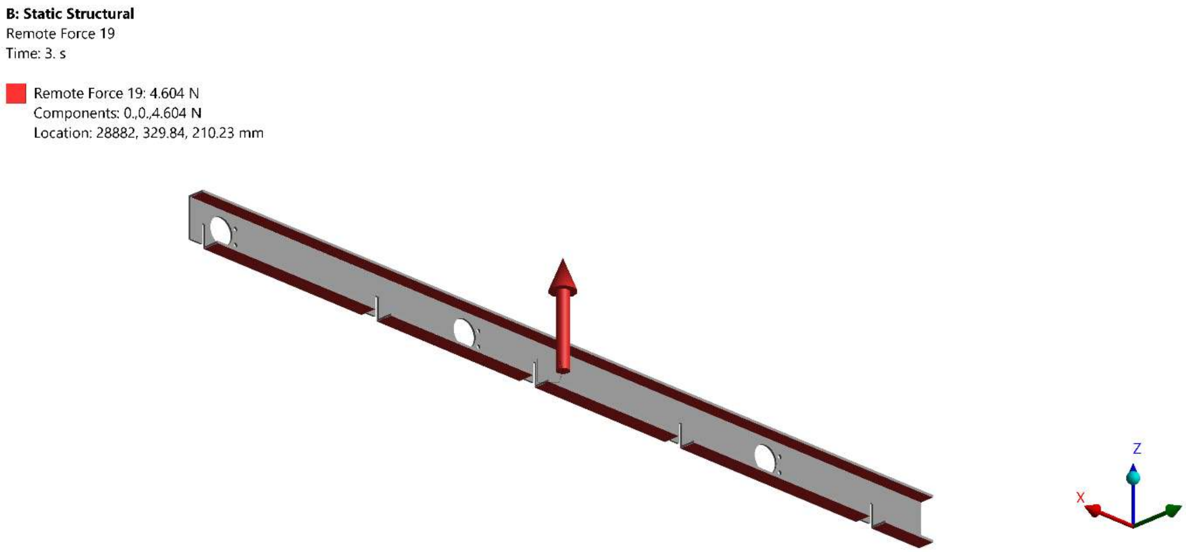

Figure 45: Example of the buoyant force being applied by remote force.

3.4. Finite Element Model Results and Discussion

3.4.1. Stress Limits

There are several key components where stresses are to be analyzed and compared against limits. These components are the composite skin, the composite beams, the anodes, the BDE board, the anode spacers, and the adapter plates. The stress limits are set by the DUNE compliance office, based on the material's 0.2% offset strength, and some strength factor, Φ, to account for loading and environmental effects like creep and humidity. The strength factor ranges from 0.215 to 0.245 depending on the load conditions. Additionally, a load factor, λ, of 1.4 is applied to the model stress results to account for things like material and model uncertainty. This load factor is applied to the von Mises stress from the model, which is what the compliance office uses to compare the results. These practices and values are taken from the finite element analysis report for the CRP by Canva. [15]

$$\sigma_{allowable} = \Phi \cdot \sigma_{0.2} \tag{7}$$

3.4.2. Safety Factor on Compliance

In engineering analysis, it is common to use the term safety factor when describing the performance of a material under load. The safety factor is defined based on the failure criteria being investigated such as yielding, tensile failure, compressive failure, creep, fatigue, etc. For this analysis, a safety factor on compliance is defined. Therefore, the safety factor is defined as the allowable stress divided by the quantity of the model calculated von Mises stress, multiplied by the load factor, 1.4.

$$SF = \frac{\sigma_{allowable}}{\lambda \cdot \sigma_{vM}} \tag{8}$$

3.4.3. Composite Skin Stresses

When analyzing the stress results of the composite skin some consideration must be given to regions involved in contact or other connections. For the bonded connections between the supporting beams and the composite skins, the mesh sizes are relatively similar, and the contact regions are large, allowing for the solver to distribute contact forces reasonably. So, the results in and near these regions can be taken at face value. However, for the bonded contact between the anode spacers and the composite skin, the meshes are highly asymmetric. Increasing the resolution of the composite skin mesh is not workable due to computational demands. In addition, contact formulation between objects of dramatically different sizes within large models is less reliable. Therefore, the results from this model of the entire CRU in these regions should be excluded and separately investigated.

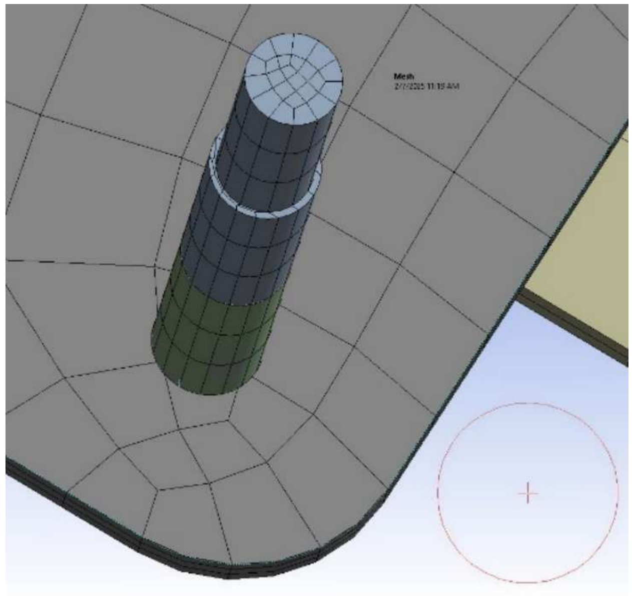

Figure 46: Detailed view of CRU FEM mesh around an anode spacer. Note the mesh asymmetry, and the low number of nodes on the composite skin coincident with nodes on the spacer.

To quantify the true stress in these areas, the results for each load step were analyzed, and one contact region consistently showed the highest stress. This region was then modelled independently of the global model. All geometry besides the composite skin and the spacer are removed, and only the region near the spacer on the composite skin is modelled, with the regions where the geometry is cut given the fixed support boundary condition. The stresses near the fixed supports should be ignored as this boundary condition is overly stiff. From the global model, the displacements of all contact surfaces on the anode spacer are extracted. Then, all the displacements at the contact regions with the PCB are rewritten as relative displacements with the contact surface between the spacer and the composite skin as the reference. These relative displacements are applied as loads to the model.

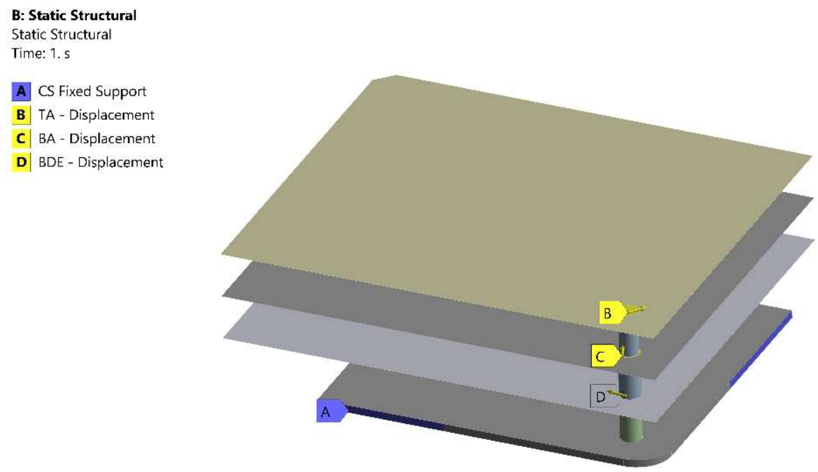

With the smaller geometry and single contact, the mesh can now be made finer on all contact surfaces. Since the results in and near the interface between the anode spacer and composite skin are of special interest, the mesh on these bodies is made carefully. First, the mesh on these bodies is made exclusively using tetrahedral elements, this is to allow the mesh refinement tools to easily modify the mesh. Then, contact sizing tools are used to make the mesh finer around the contact regions. Next, the refinement tool is used to refine the mesh around complex geometry and the edges of components. Finally, the mesh edit environment is used to perform a contact match. This operation forces all mesh nodes on either side of a contact pair to have identical node locations, making contact much more reliable and realistic. However, this function only works when the mesh on both bodies is only comprised of tetrahedral elements. This makes the tool unsuitable for large assemblies which would be inefficient to mesh using tetrahedral elements.

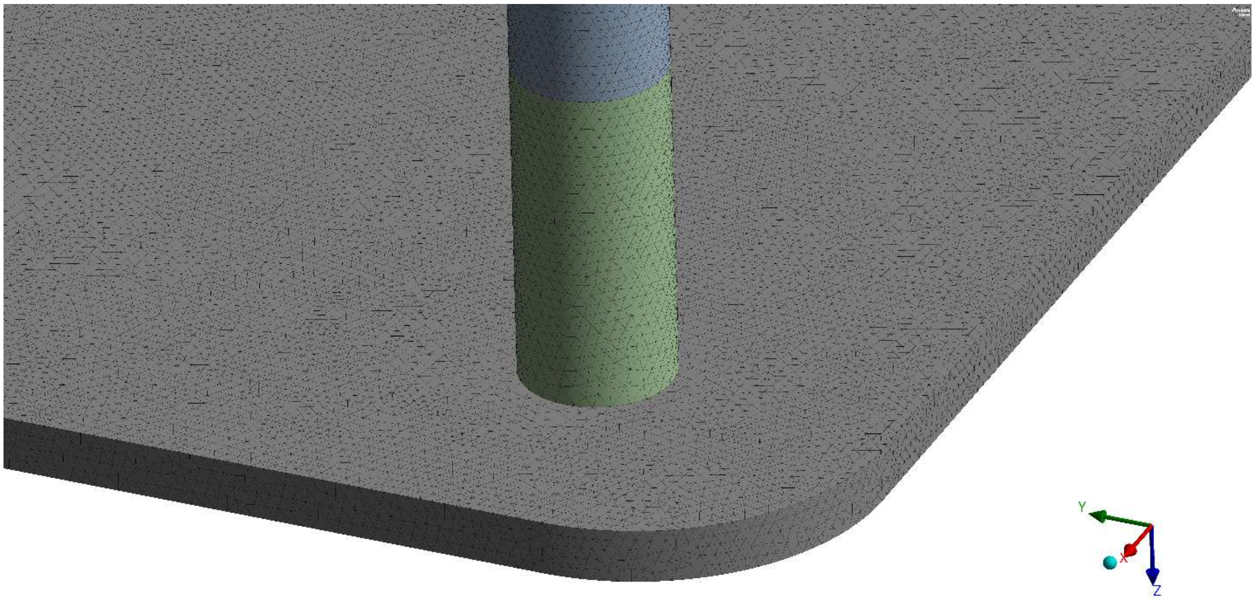

Figure 47: Mesh of the anode spacer - composite skin contact pair sub-model. Notice that the mesh is much finer, and that all nodes are coincident at the interface.

Upon performing the analysis and post-processing the results, the expected maximum contact stress is 3.03 MPa compared to the global model's prediction of 44.1 MPa, as seen in Figure 48. These maximum values both occur in the final load step when the CRU is submerged in liquid argon. The stress in the composite skin far away from the cut boundary and contact regions are within agreement as well, which validates the sub-model approach. Going forward, any contact stress near an anode spacer above 5 MPa will be ignored when post-processing the results of the global model on the composite skin.

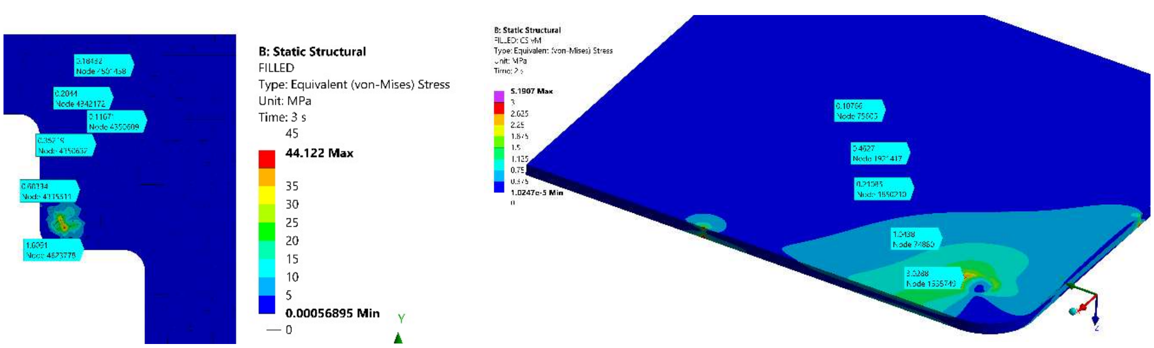

Figure 48: Stress results of the most severe anode spacer – composite skin contact pair for the global model (left) and the sub-model (right). Notice the much lower maximum stress due to the improved mesh and contact definition, and the similar stresses far away from the contact region.

Similarly, stress results near beam connections representing the bolted connections between the adapter plate and the lower composite skin require special attention when post-processing. The beam connections apply all the preload to the scoped reference and mobile areas, which are on the adapter plate and composite skin respectively, as the washers are not modelled. This makes the model simpler as mentioned in on page 53, but now the forces which would be borne by the washers are being directly applied to the composite skin and adapter plate. Additionally, the bolted joints have clearances to allow for differential thermal contraction which the beam connection does not model, so forces due to this contraction which would not occur in the cryostat are applied to the nodes in the scoped areas. Therefore, the results in and near these areas are ignored during result processing.

When the CRU is in room temperature air, the greatest stress in the CRU predicted by the model is the contact stress between an anode spacer and the upper composite skin. It is calculated that the true maximum contact stress is approximately 3 MPa from the sub-model. There are no stresses which occur in either the upper or lower composite skin of the CRU that exceed 3 MPa in this load step. Therefore, the maximum stress can be is 3 MPa.

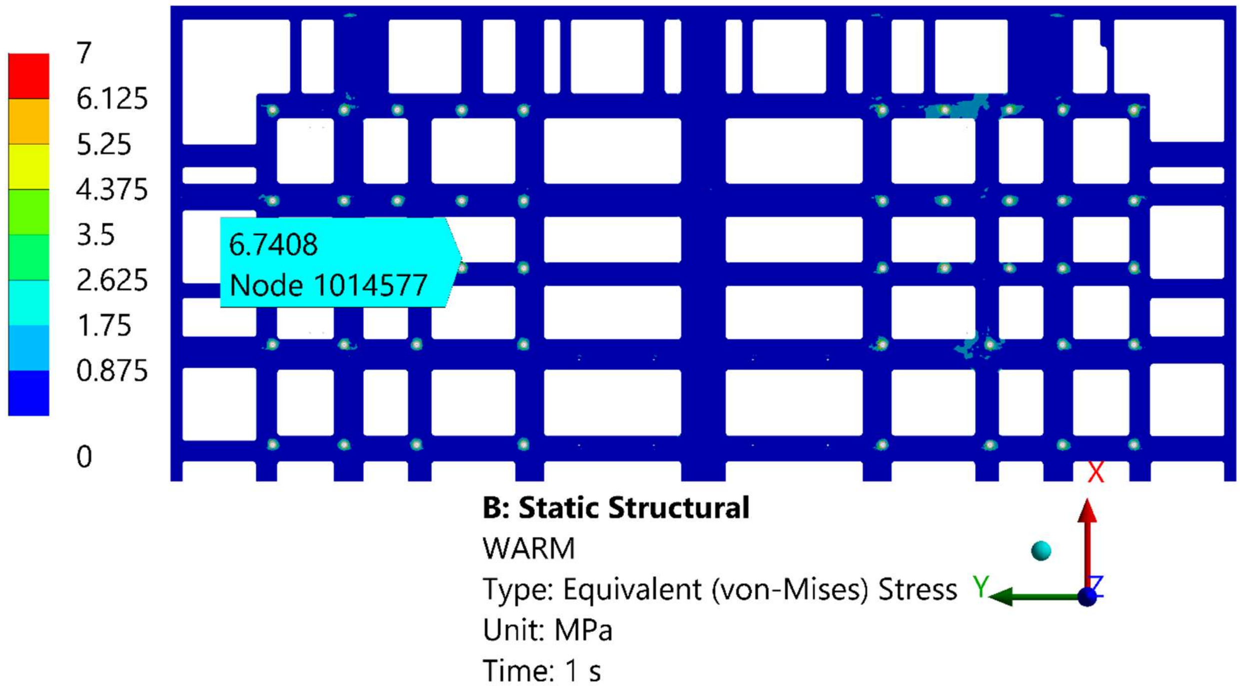

Figure 49: Stress in the composite skin in room temperature air.

During the second load step the CRU is exposed to liquid argon temperature, and slides along the membrane floor towards its final position. Both conditions increase the stress in the composite skin. The maximum stress in these conditions is 23.6 MPa and occurs where two composite beams intersect above a bottom support and adapter plate. This region has high stiffness which results in higher stresses.

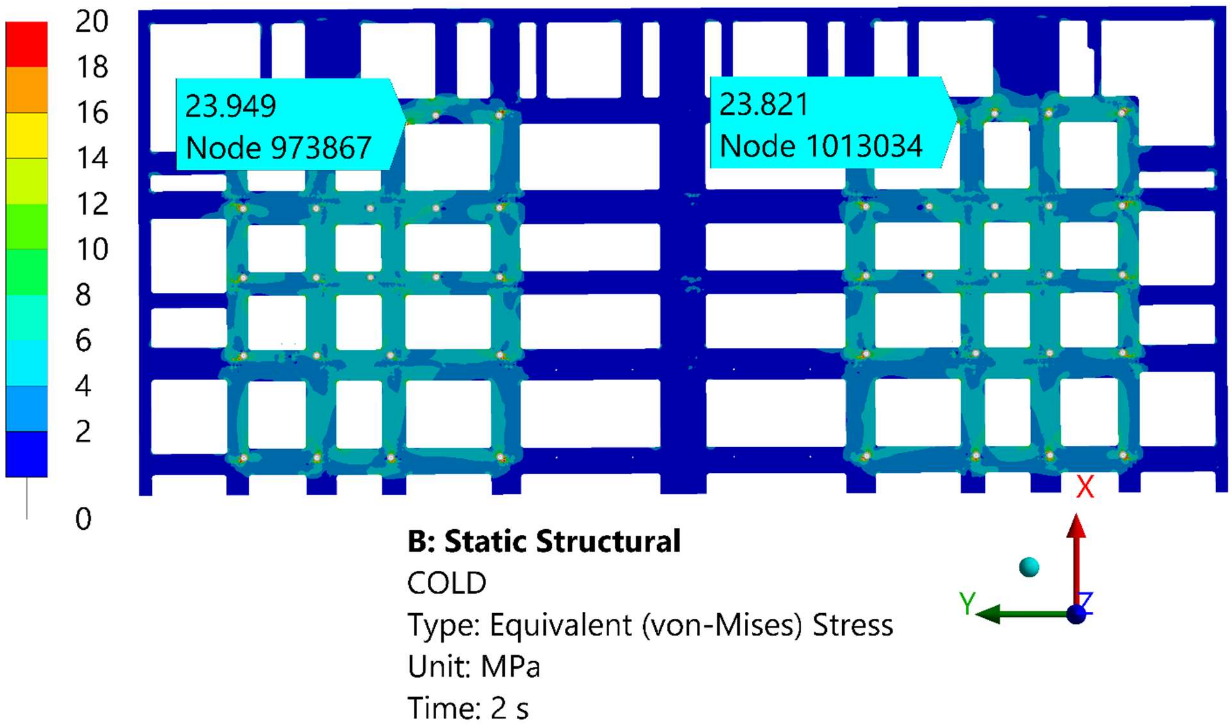

Figure 50: Stress in the composite skin during cooldown.

After this load step the CRU is submerged in liquid argon, and the buoyancy forces are added. The maximum stress on the composite skin in this condition is 25.2 MPa. The safety factor on compliance for this load case is 1.3.

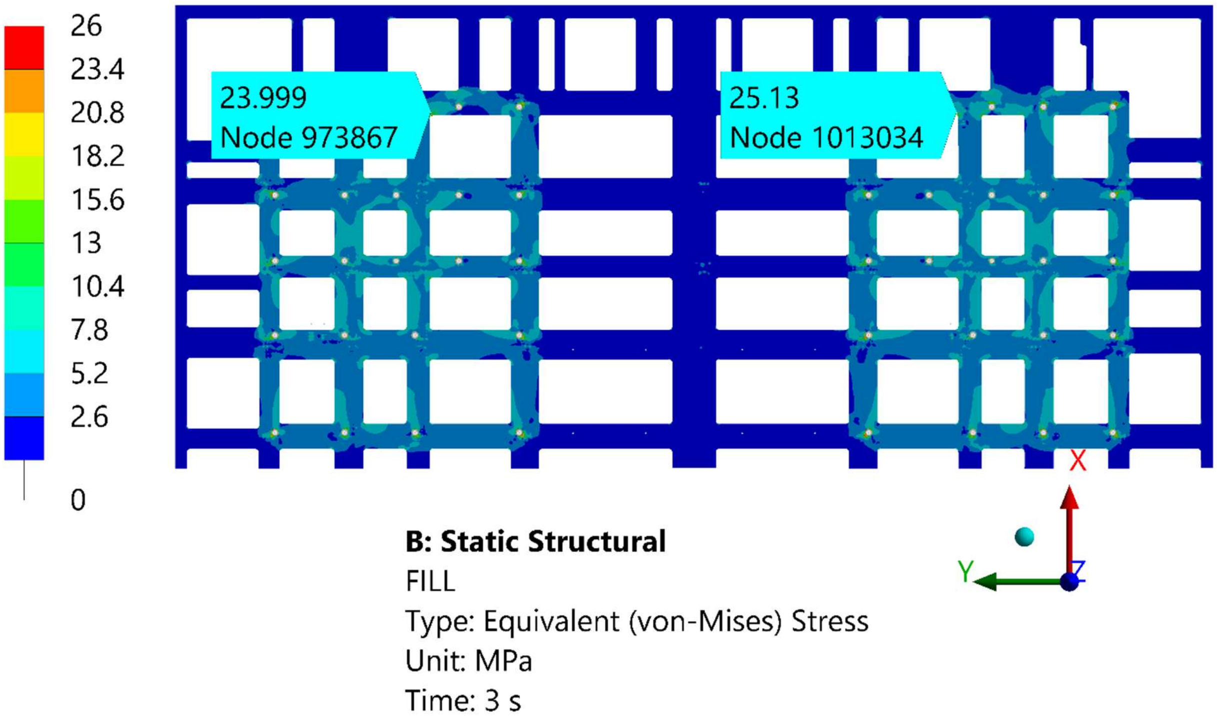

Figure 51: Stress in the composite skin when submerged in liquid argon.

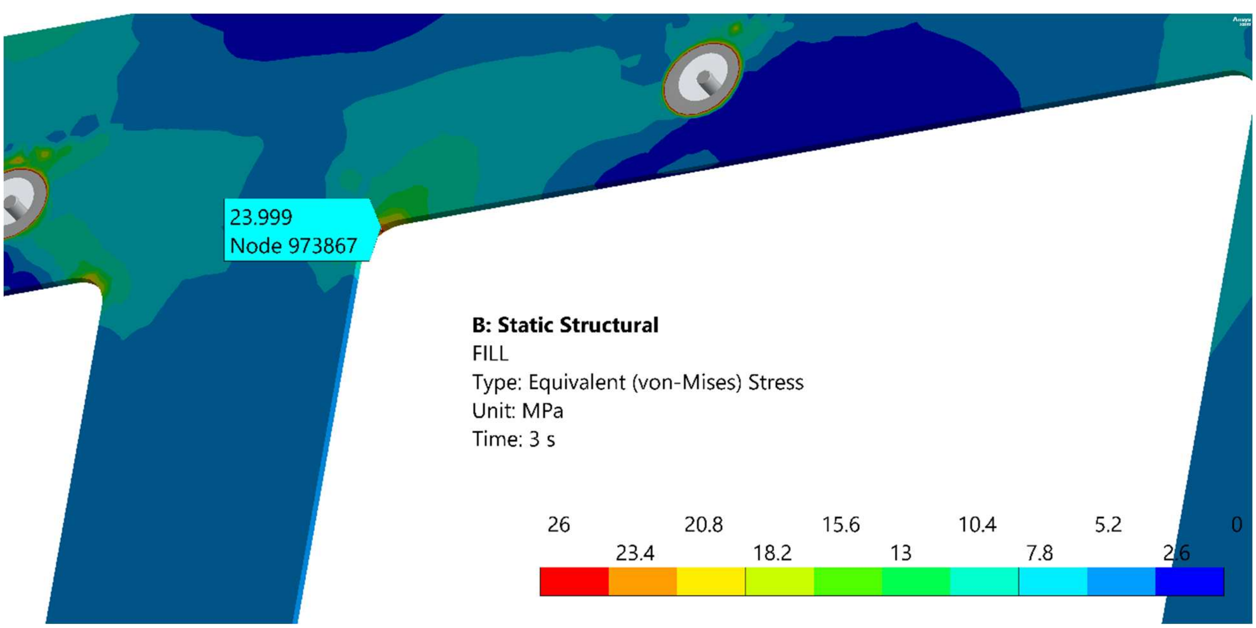

Figure 52: Detailed view of the maximum stress in the composite skin when submerged in liquid argon.

3.4.4. Composite Beam Stresses

Unlike the composite skin, no particular care needs to be taken when post-processing the stress results for the composite beams, as the only contacts are those bonded connections to each other and the composite skin. These contacts are well defined over large areas with largely symmetric meshes. The maximum stress as the CRU is in room temperature air is 5.3 MPa. This occurs at one of the large circular cut-outs where cables pass through, right over a bottom support. The lack of material, the stress concentration associated with the hole, and the high stiffness of the region due to the support all contribute to increased stress in this location.

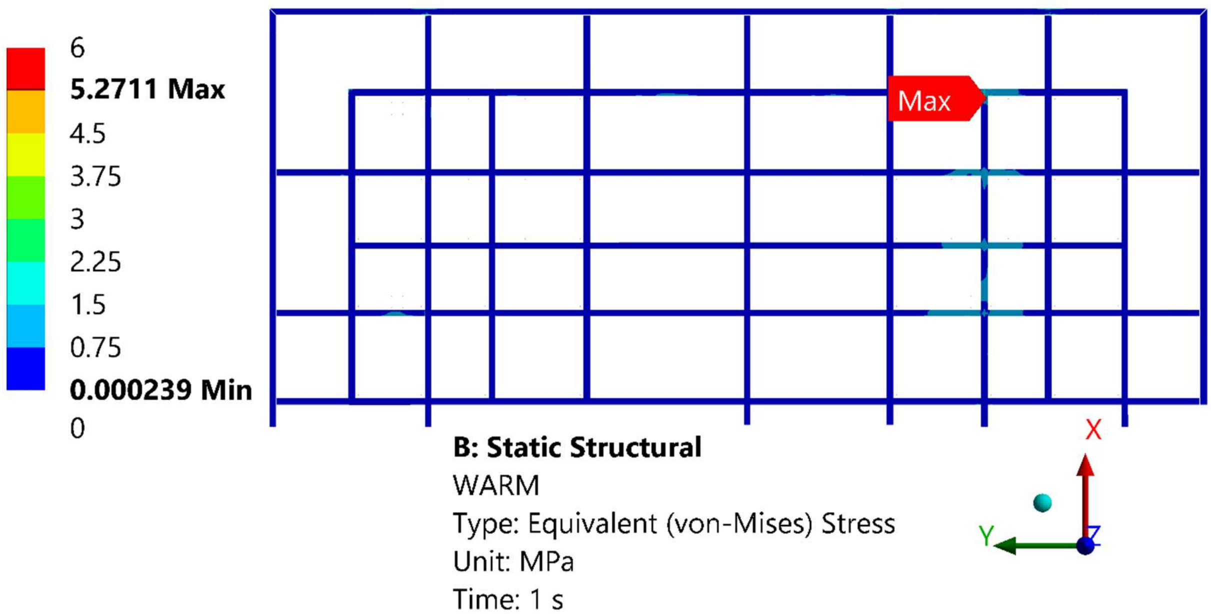

Figure 53: Overall view of the stress in the composite beam web of the CRU in room temperature air.

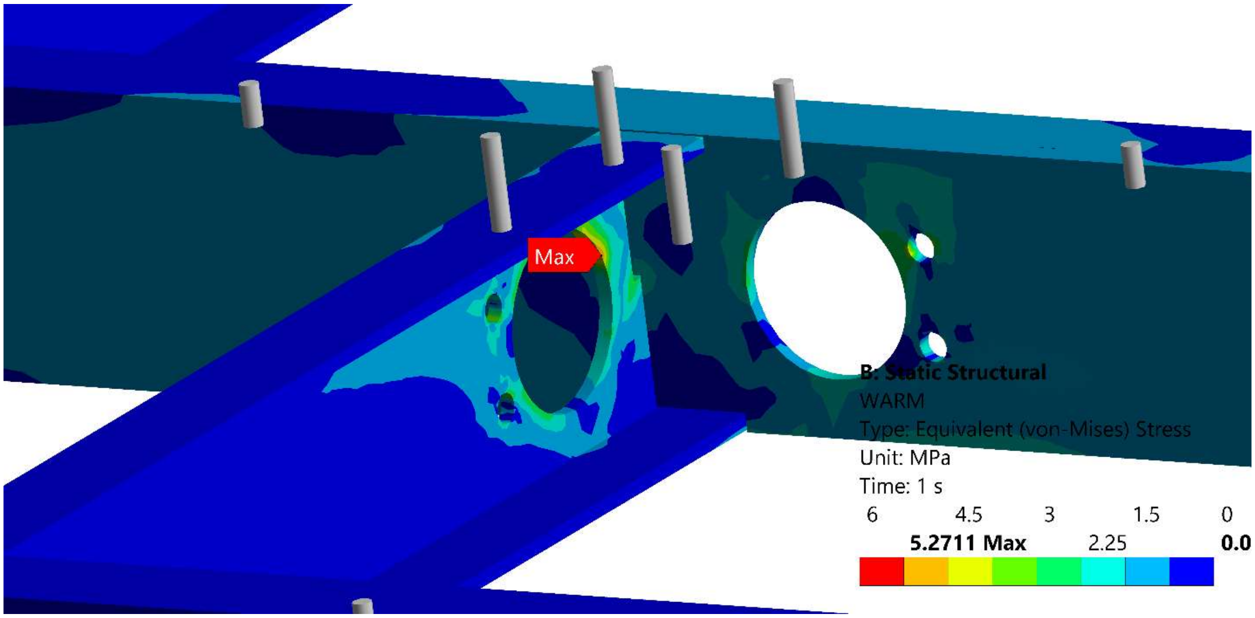

Figure 54: Detailed view of the maximum stress in the composite beams when the CRU is at room temperature.

As the CRU is submerged the maximum stress rises to 12.3 MPa, and occurs at a perpendicular intersection of two beams, over a support attached to an adapter plate. This maximum stress is used to calculate the safety factor on compliance, which has its minimum value of 3.0 when the CRU is submerged. This region has increased stiffness and in this load step differential contractions are occurring, so it makes sense that the stress in this area would be elevated. The maximum stress also occurs at a 3D corner on the beam which is a stress concentration point. The stress within the cross-section of this beam at the same axial position is noticeably lower than this maximum. A detailed view of this is shown in Figure 56.

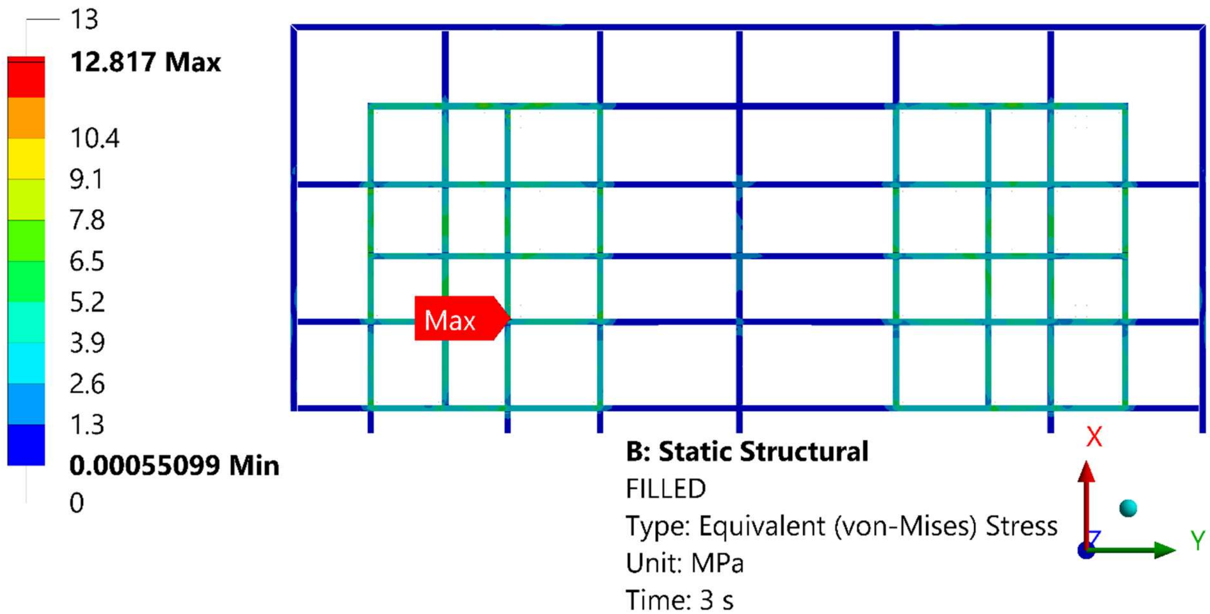

Figure 55: Plot of stress within the CRU's beam structure when submerged in liquid argon.

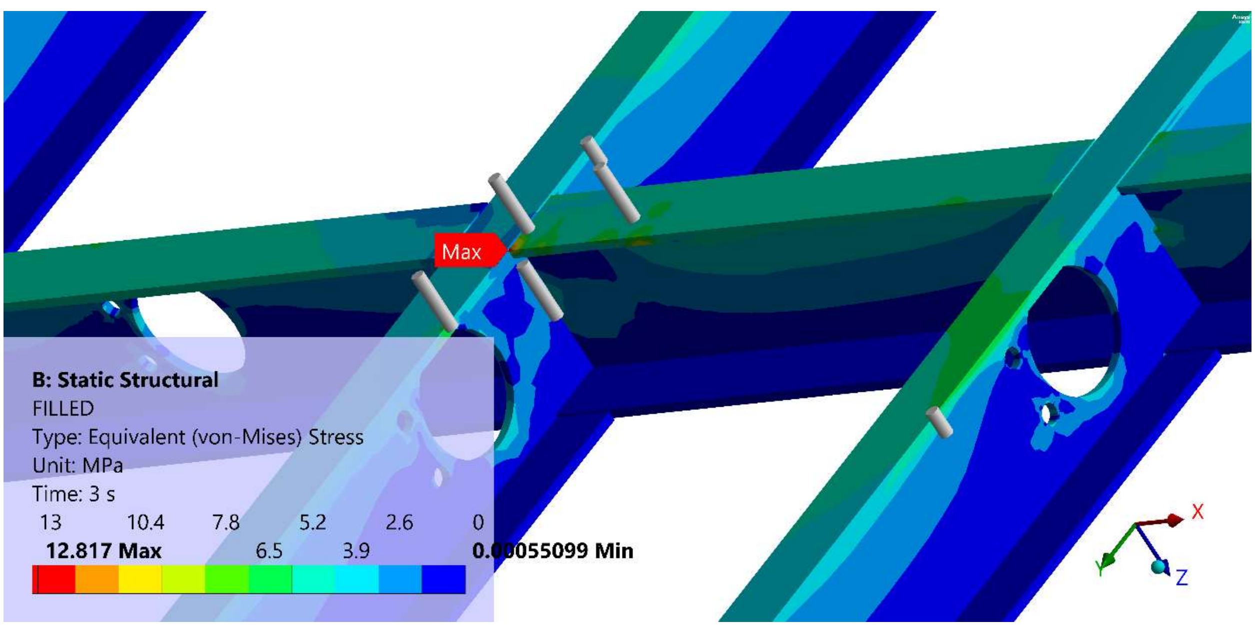

Figure 56: Close-up view of the maximum stress in the CRU beam structure.

3.4.5. Anode Stresses

When the CRU is in room temperature air, the maximum stress in the anode PCBs occurs in locations where they are supported by anode spacers. There is also increased stress along the edges where there are bonded contacts with the edge cards. The maximum for the bottom anode is 1.6 MPa, and 1.0 MPa for the top anode. The first figure shows the stress within the bottom anode, and the following figure shows the stress in the top anode.

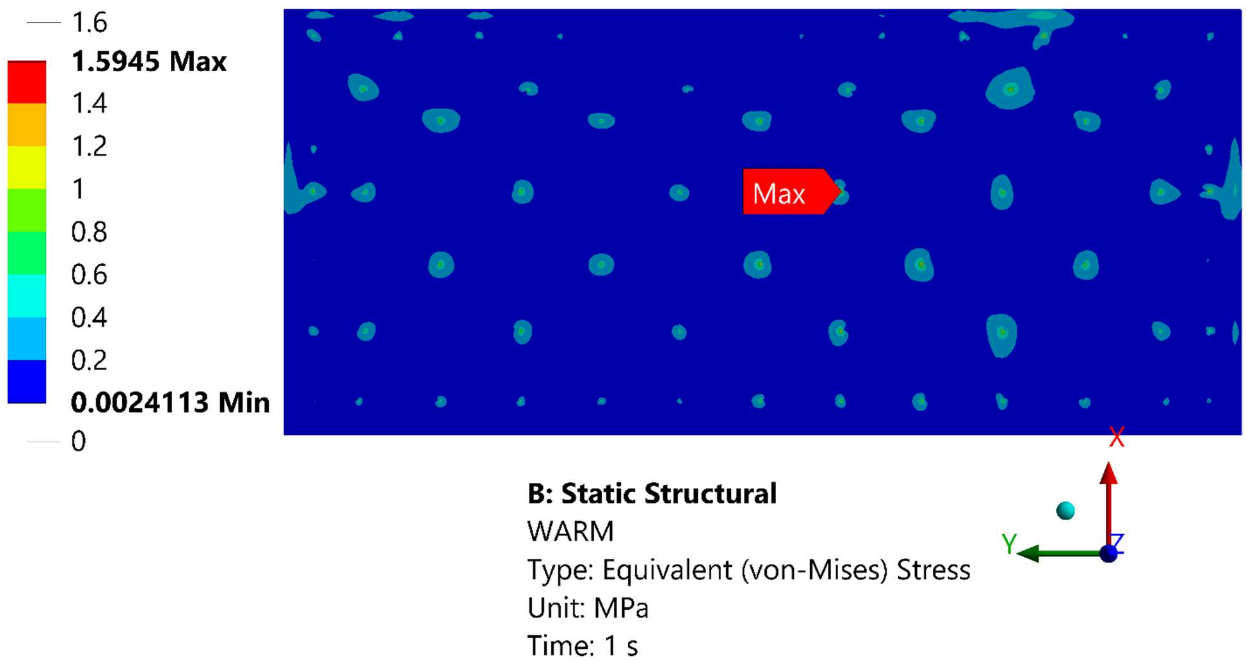

Figure 57: Stress in the bottom anode as the CRU is in room temperature air.

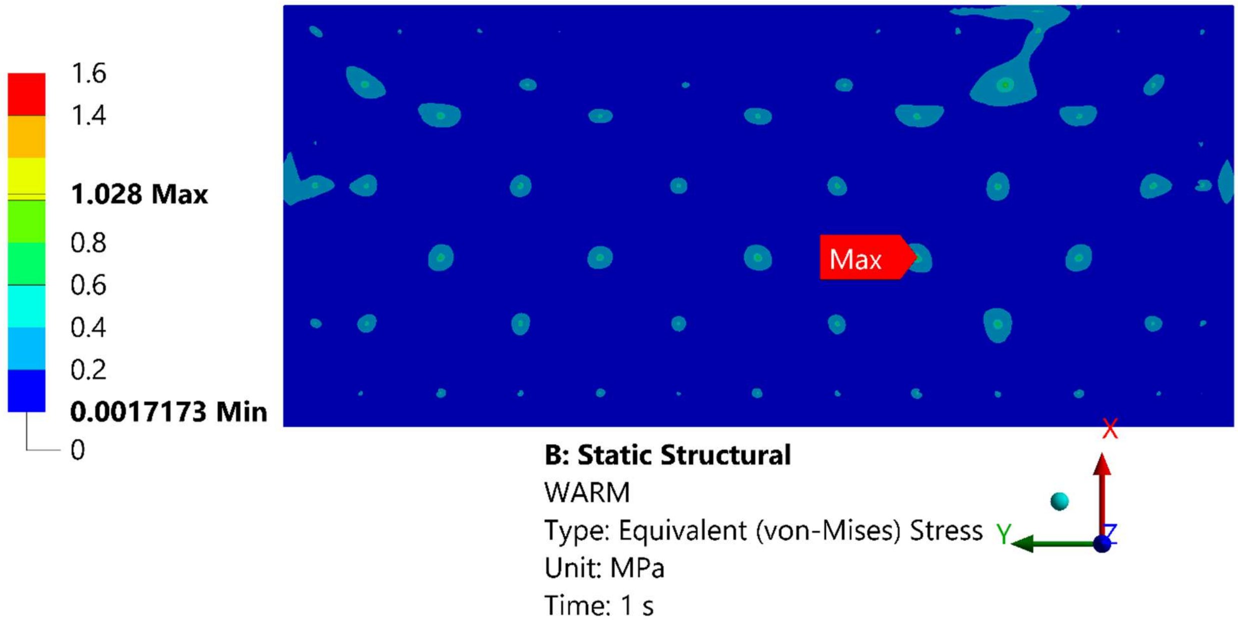

Figure 58: Stress in the top anode as the CRU is in room temperature air.

As the CRU cools down the primary source of stress becomes thermal contraction, and the effects of gravity become negligible. Thermal stresses are typically at their maximum where two components are joined together. In this case, the maximum stress shifts to where the anodes are bonded to the edge cards, instead of where the anodes are supported by the anode spacers. These values do not change by a significant amount whether the CRU cooled but not submerged, or if it is submerged and is 20.1 MPa for the top anode and 20.2 MPa for the bottom anode. This maximum occurs at the rear edge where the anodes are bonded to the edge cards and occurs near the midpoint of the edge. The minimum safety factor of on compliance for the anodes occurs on the top anode when the CRU is submerged. The value of the safety factor is 3.2. A detailed view of this is in Figure 63.

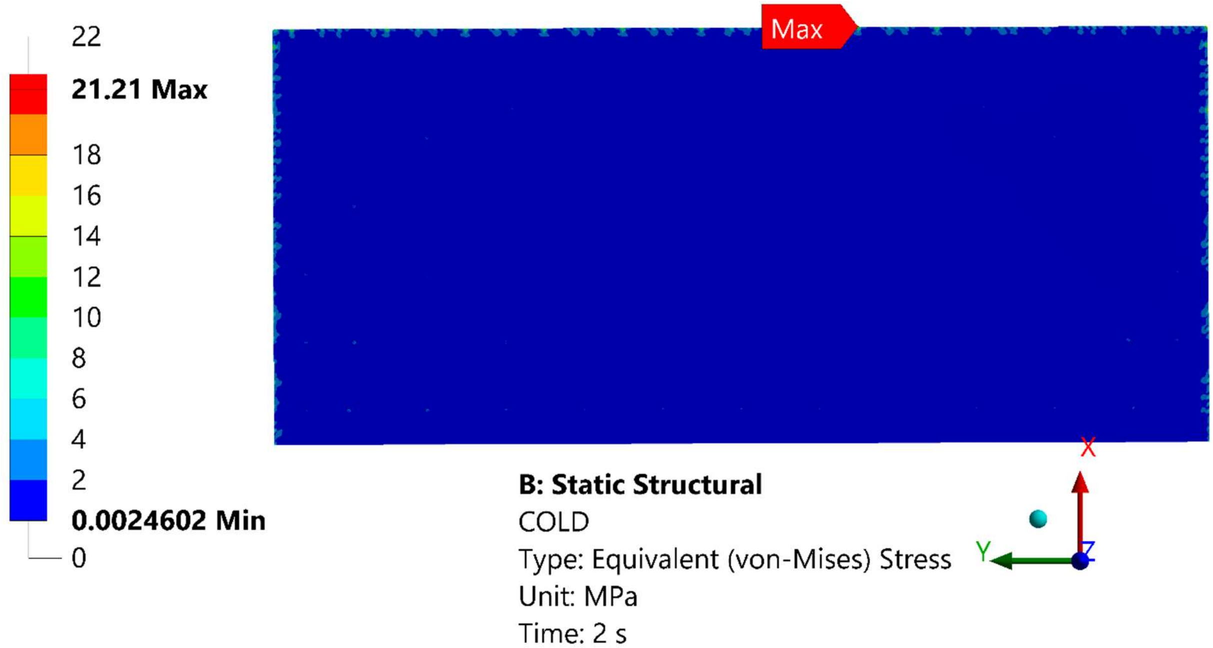

Figure 59: Bottom anode when the CRU is cooled but not submerged.

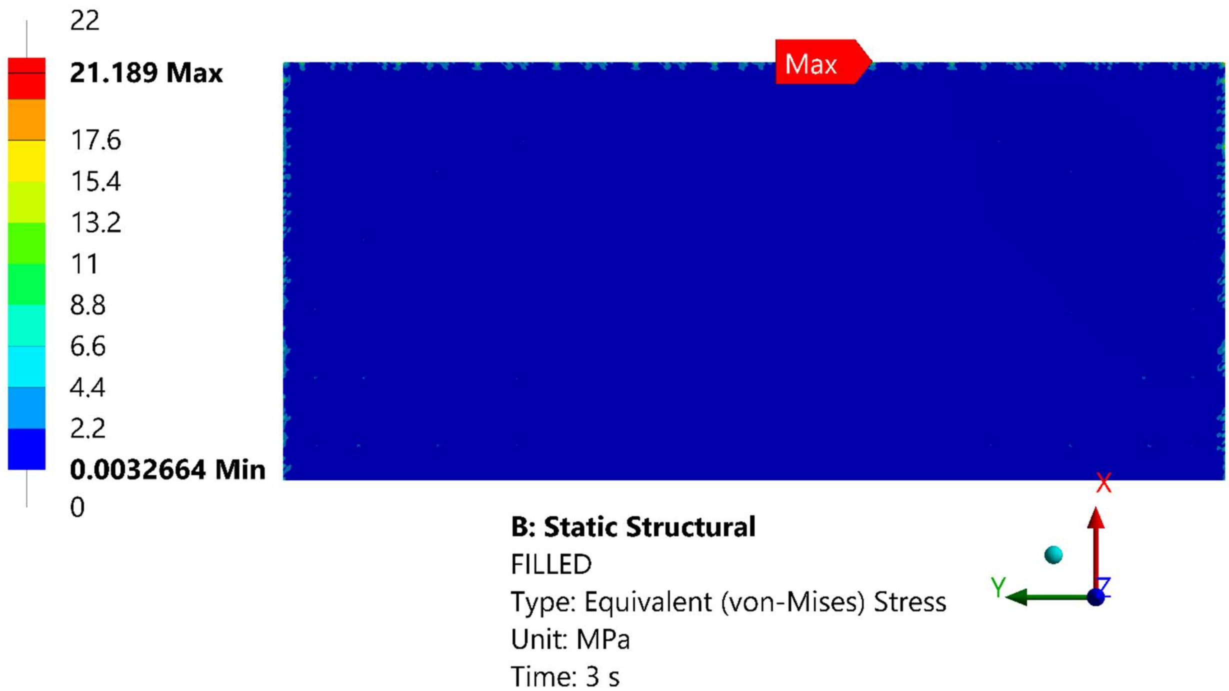

Figure 60: Bottom anode when the CRU is submerged.

Figure 61: Top anode stress when the CRU is cooled but not submerged.

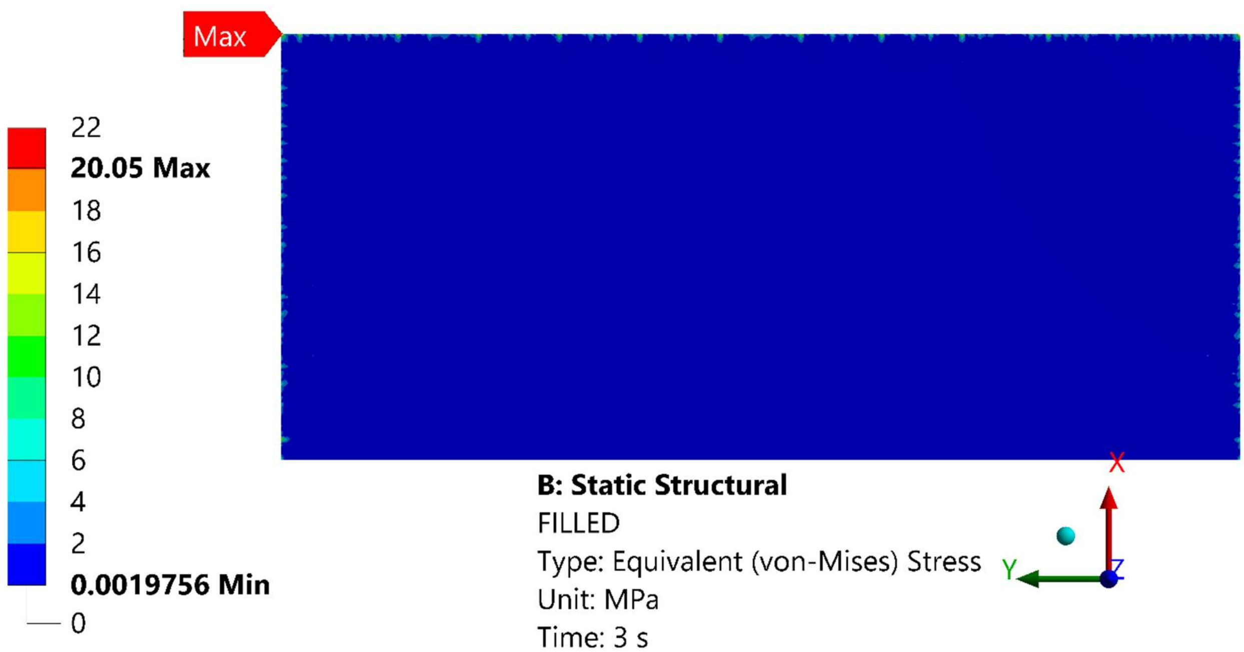

Figure 62: Top anode stress when the CRU is submerged.

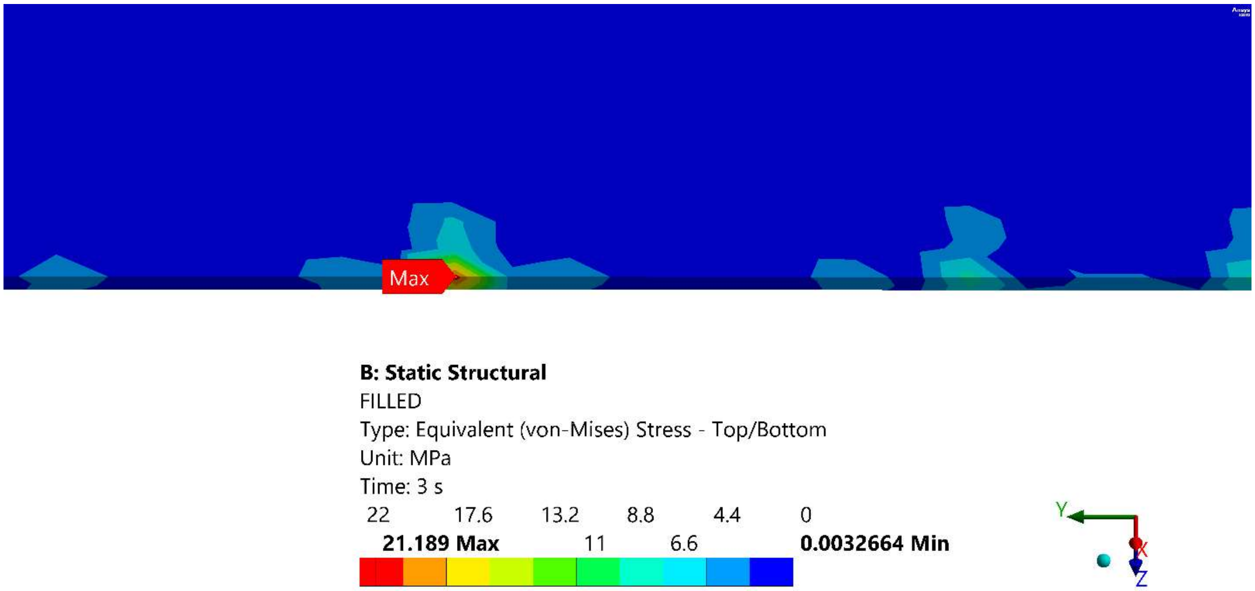

Figure 63: Detailed view of the location where the maximum stresses occur in the anodes. This is an edge with bonded connections.

3.4.6. BDE Stresses

The maximum stress in the BDE when the CRU is in room temperature air occurs at a corner in the simplified geometry where copper link plates are in the real geometry. Each of these sections of the BDE suspend an FEMB underneath them. The maximum stress when the CRU is in room temperature air is 4.2 MPa. This maximum occurs where an anode spacer supports the BDE from below.

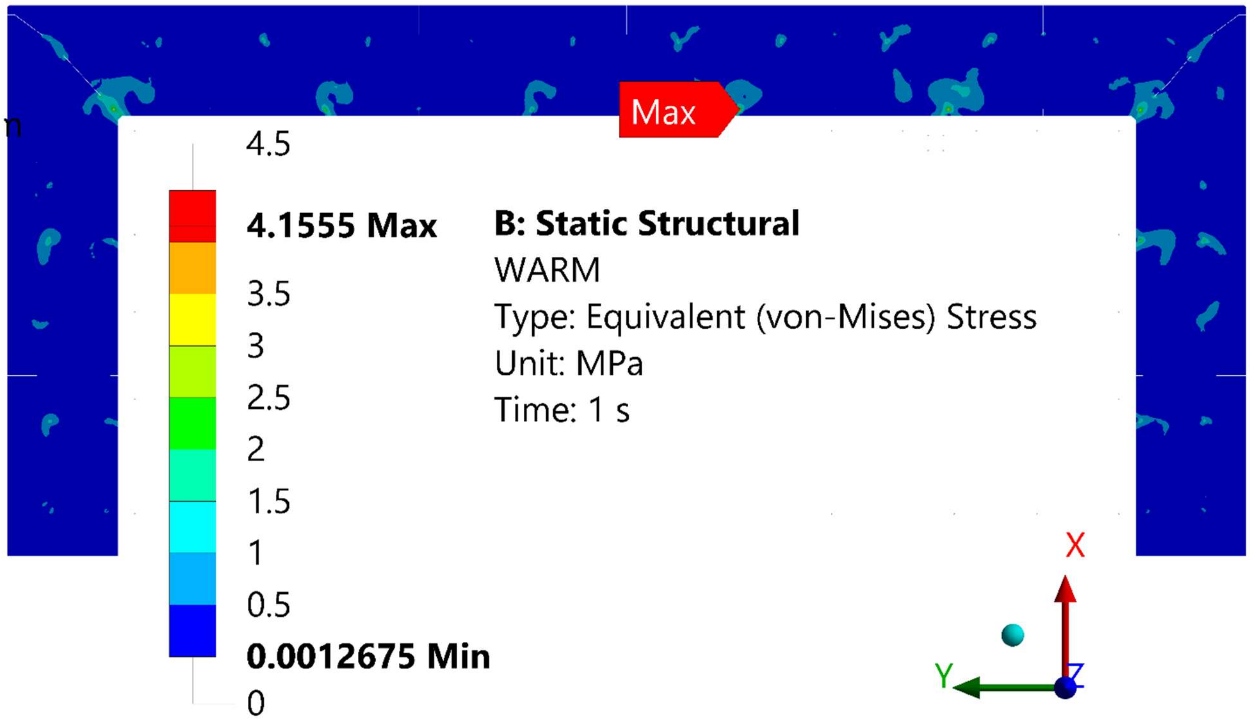

Figure 64: Stress within the BDE when the CRU is in room temperature air.

Like the anodes, when the BDE cools down the location of increased stress shifts to the bonded connection with the edge cards due to the thermal contraction. This stress does not have a strong dependence on whether the cryostat is filled, it is only due to the temperature change. The maximum stress, at 28.8 MPa, is greater than that for the anodes, but this is due to the stress concentration that occurs due to the location being a corner. Using this maximum stress value still gives a passing safety factor on compliance for these load cases. The minimum safety factor is 2.3 and occurs when the CRU is submerged.

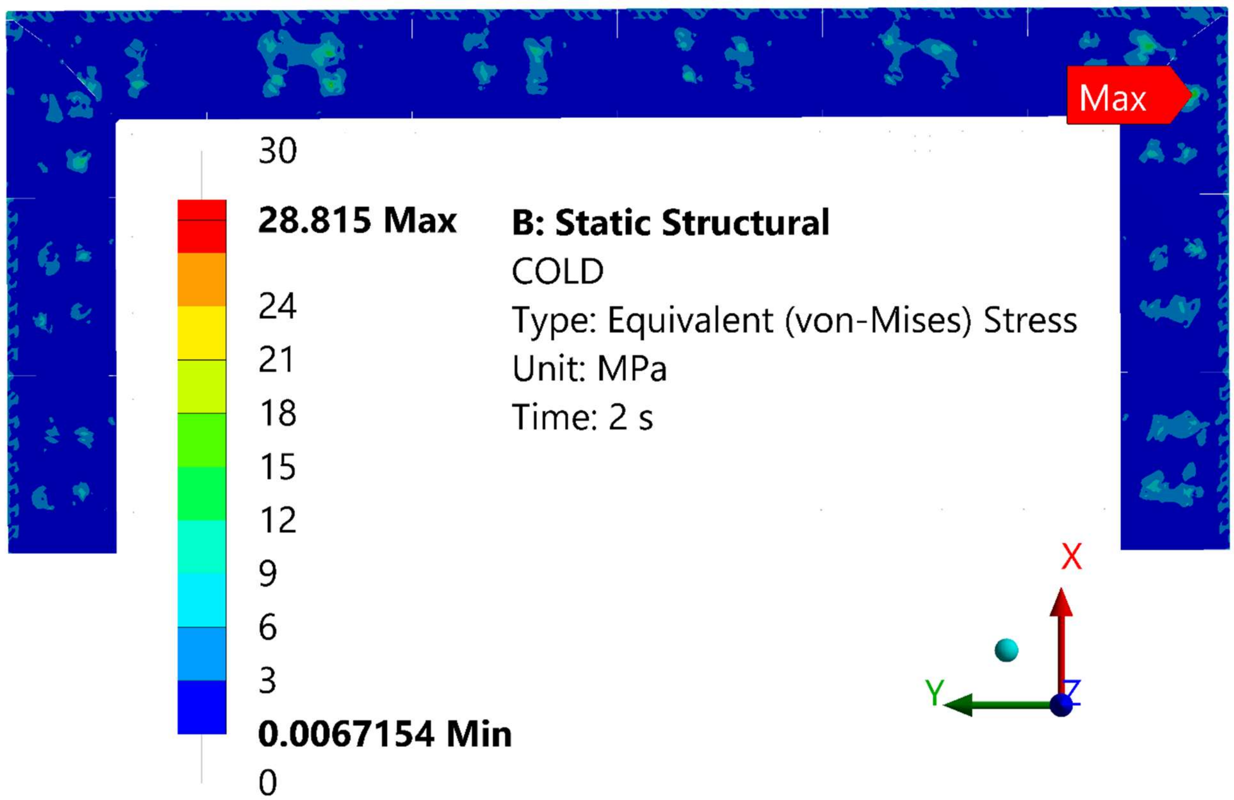

Figure 65: Plot of stress within the BDE when the CRU is cooled.

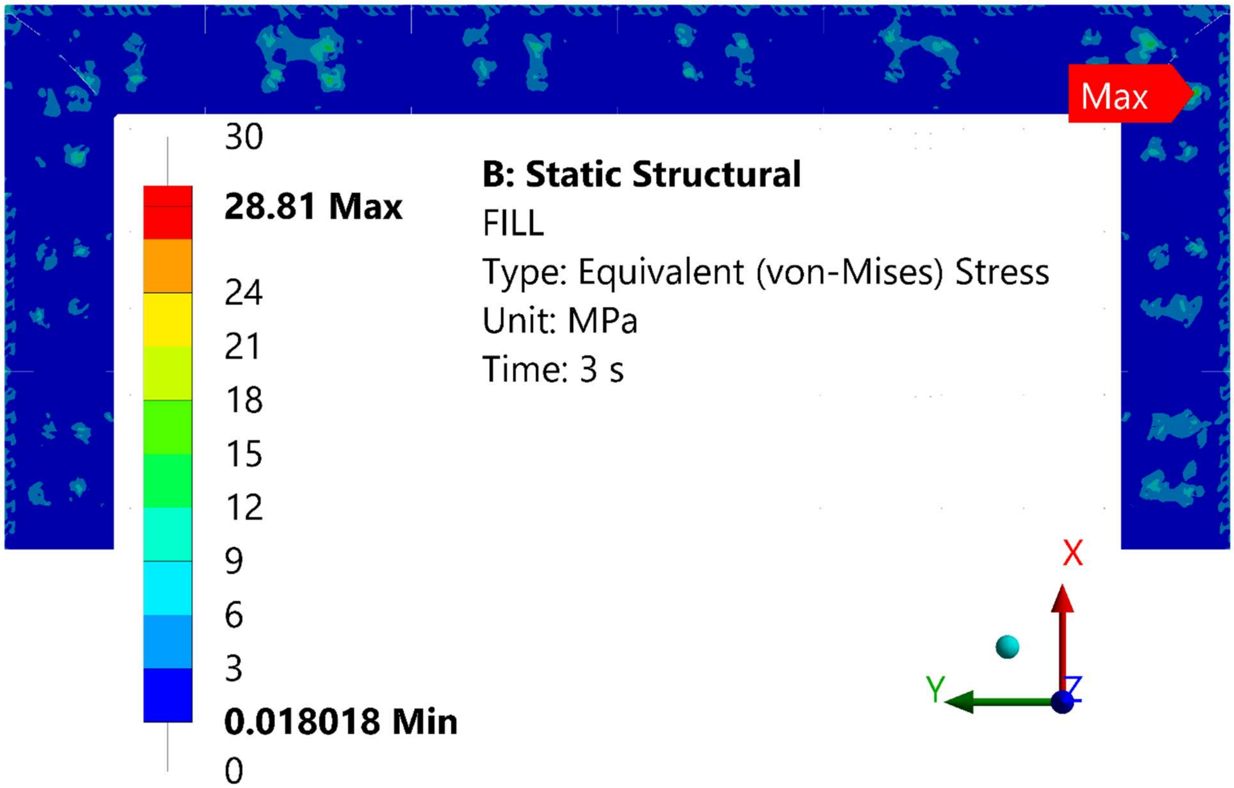

Figure 66: Plot of stress within the BDE when the CRU is submerged.

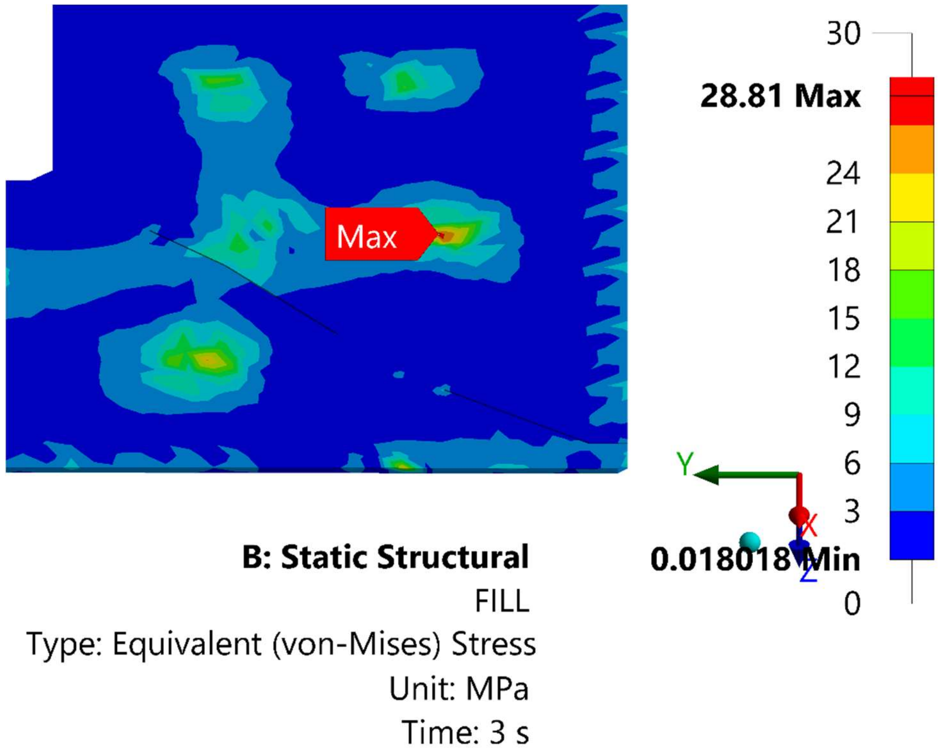

Figure 67: Detailed view of the location of maximum stress on the BDE. Notice that as a sharp corner it is a stress concentration.

3.4.7. Anode Spacer Stresses

Since the anode spacers are modelled using beam elements, there are several ways to post-process the results. The results can be any combination of direct axial stress, bending stress, or shear stress. Direct axial stress is the stress that occurs in a beam due to purely axial loading, like a point load acting through the centroid of the cross-section of the beam. Bending stresses are the result of either eccentric axial loads or loads perpendicular to the cross section at some distance from support. These same loads cause shear stresses. The von Mises stress in a beam is a combination of all these stresses and is the most complete depiction of the state of stress in a beam element. If the beam is sufficiently slender, the shear stresses can be ignored, and only the axial stress components from bending and direct axial loading become significant. The results shown are von Mises results from the FE model.

When the CRU is resting in room temperature air, the maximum von Mises stress within any anode spacer is 8.4 MPa. This stress occurs at the end of the beam which is fixed to the composite skin via a joint, which is consistent with expectation. The anode spacers are essentially cantilevered beams with loads being transferred to them by the PCBs. Cantilevered beams show the maximum stress at their fixed end.

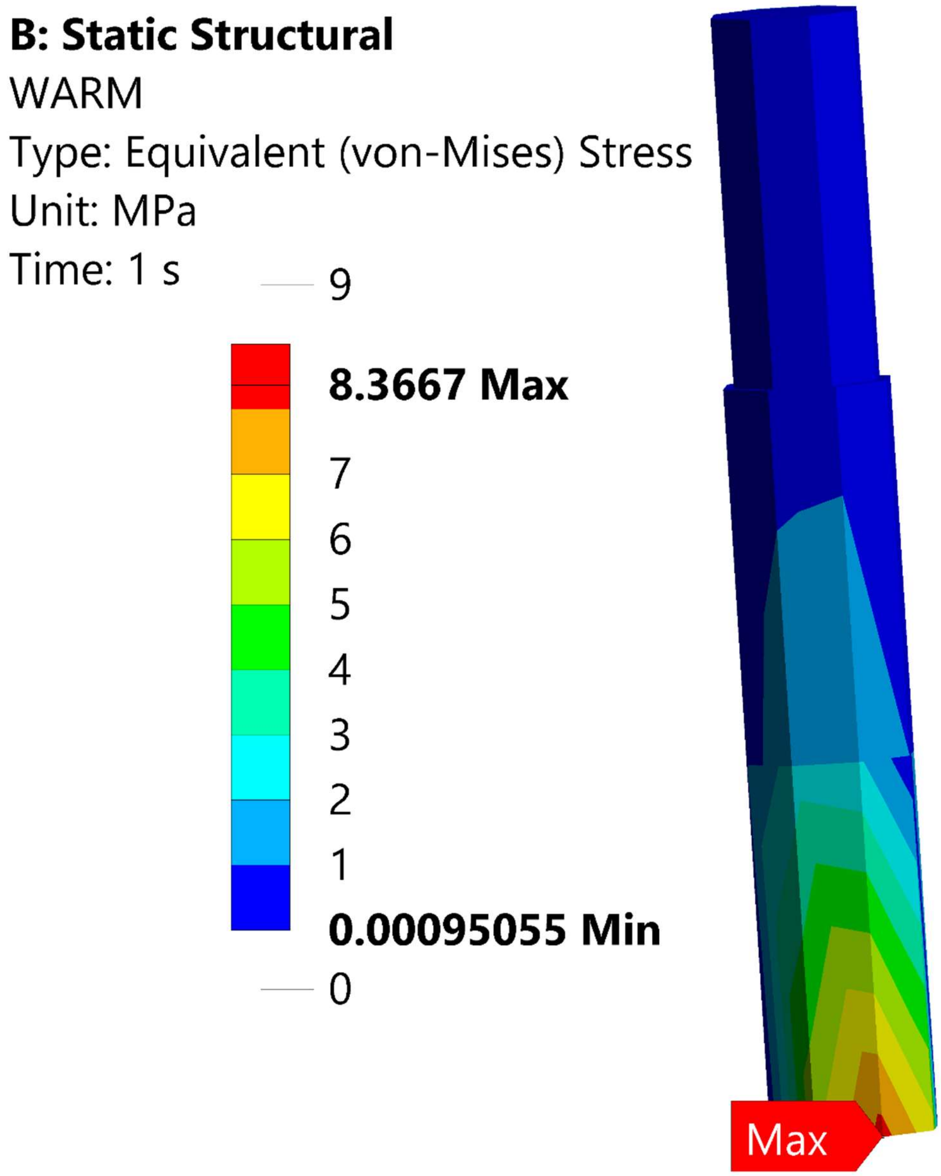

Figure 68: von Mises stress within the anode spacer with maximum stress when the CRU is in room temperature air.

As the CRU cools the maximum stress within any of the anode spacers rises to 13.433 MPa, and occurs where the BDE meets the anode spacer. This is where the most significant deformation occurs as the BDE suspends FEMBs and has some curvature. As thermal contractions occur, this is exaggerated.

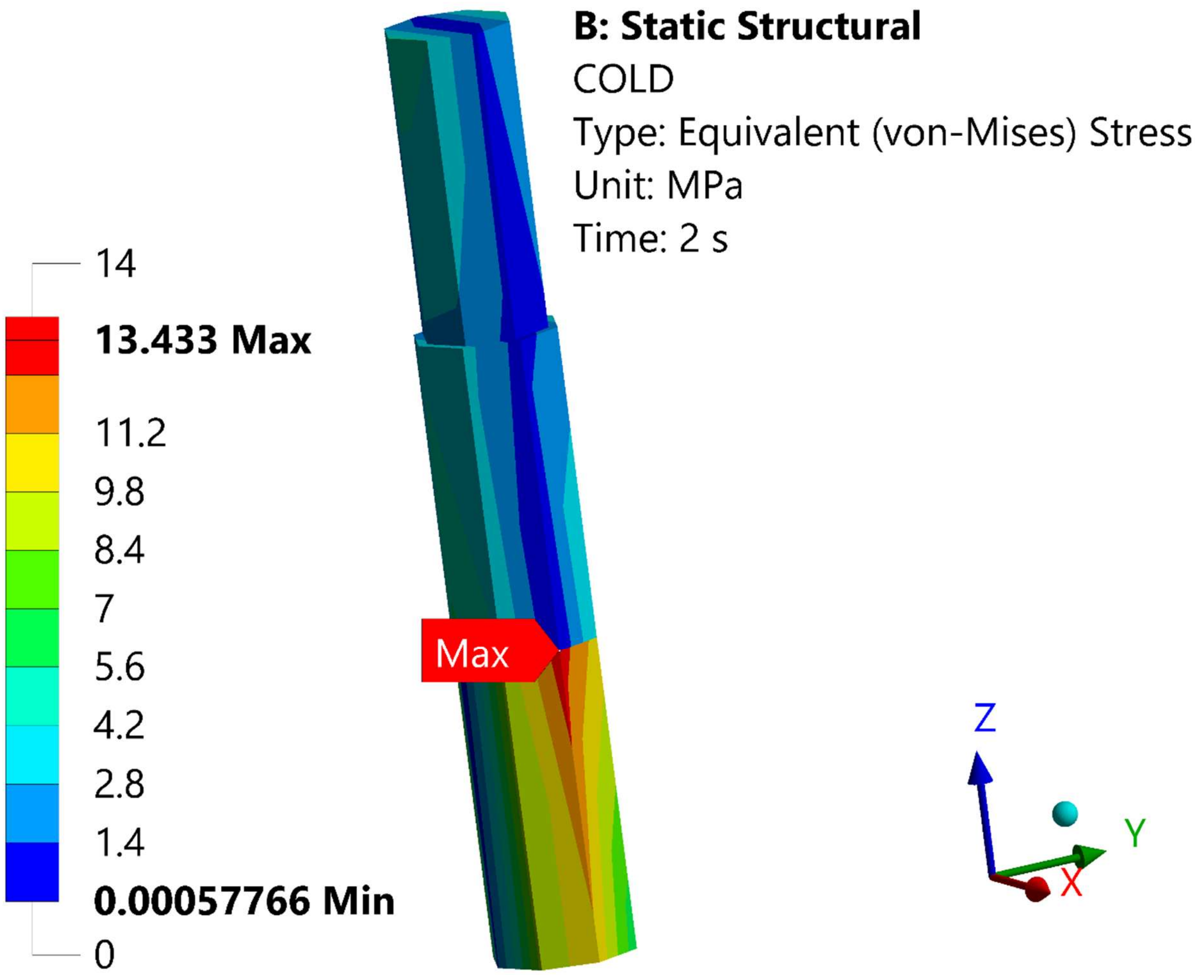

Figure 69: von Mises stress within the anode spacer with the most stress when the CRU is cooling down.

As the cryostat is filled with liquid argon, the stress in this spacer decreases slightly to 13.3 MPa, as the weight of the PCBs is reduced by the buoyancy effects of being submerged. This case has the lowest safety factor on compliance of 1.1.

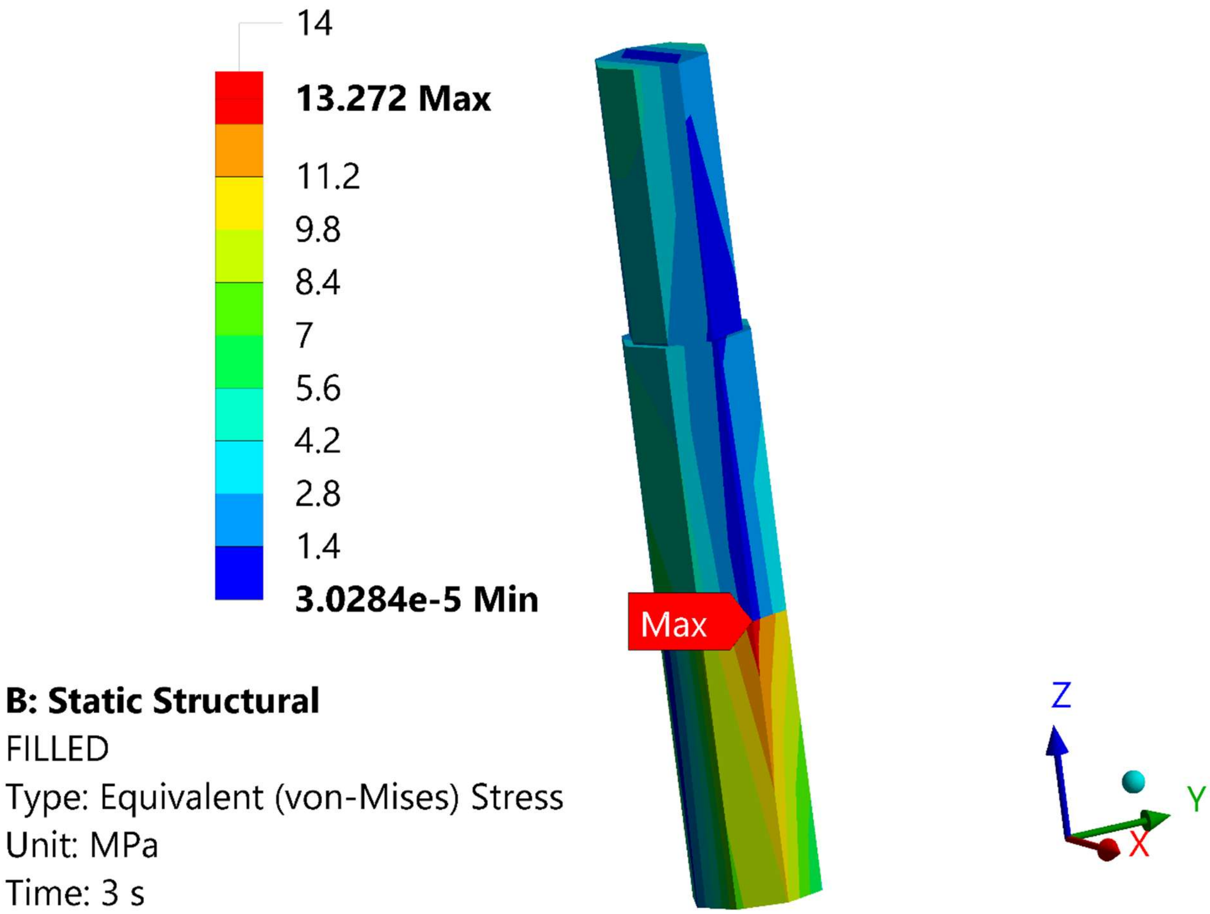

Figure 70: von Mises stress within the same spacer when the CRU is submerged in liquid argon.

3.4.8. Adapter Plate Stresses

The adapter plate serves as a medium to attach bottom supports to the CRU composite superstructure without requiring many additional rivet nuts to be inserted into the superstructure. Each adapter plate has 23 bolted joints to the CRU, and 8 bolted joints to bottom supports. These bolted joints are modelled as beam connections, as mentioned above. Just like 3.4.3, the stresses near these beam connections should be ignored during post-processing, as the beam connections do not account for designed clearance, or the washers in the assembly.

The maximum stress when the CRU is in room temperature air is 4.7 MPa and is where a bottom support is located. In general, all the regions of elevated stress, when the CRU is warm, are directly underneath the bottom support. When the CRU cools down, the maximum stress of 16.6 MPa occurs at a corner in one of the argon flow pockets near the bottom supports. When the CRU is submerged, the location of maximum stress is also a corner within one of the argon flow pockets, but this one is far from any bottom supports. The stress decreases to 16.4 MPa, but the submerged case still has the lowest safety factor on compliance of 2.3 due to more conservative limits.

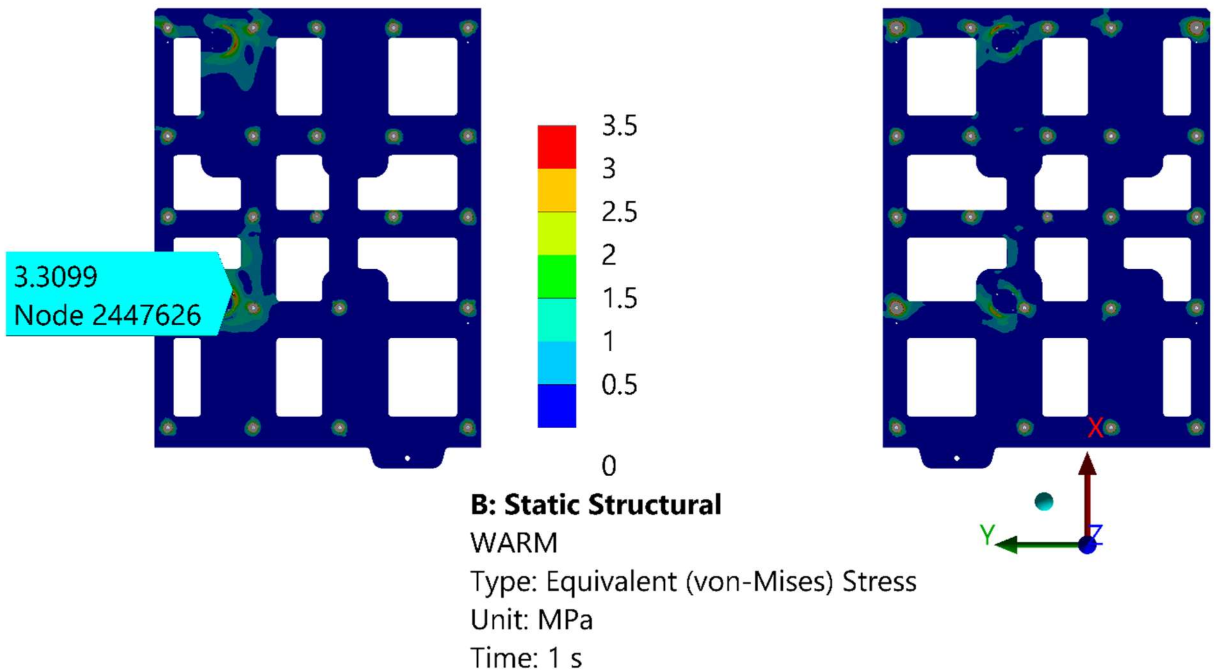

Figure 71: Plot of adapter plate stress when the CRU is in room temperature air.

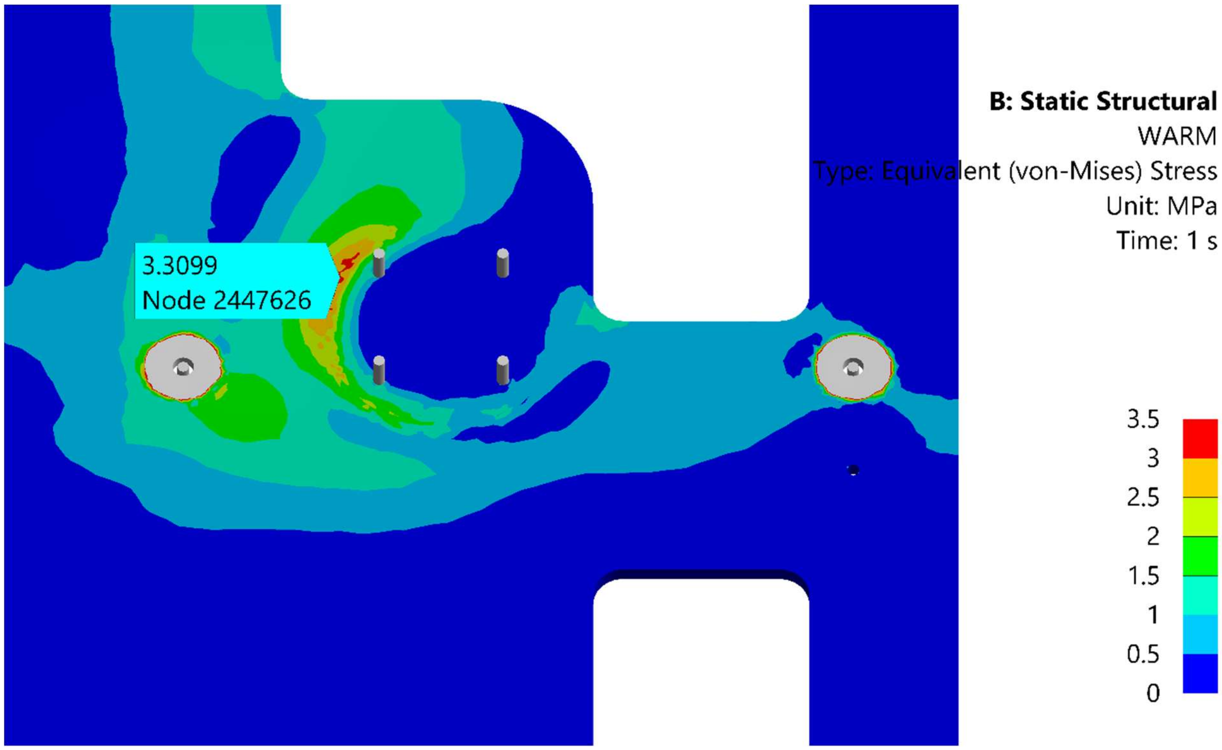

Figure 72: Detailed view of warm state adapter plate stresses.

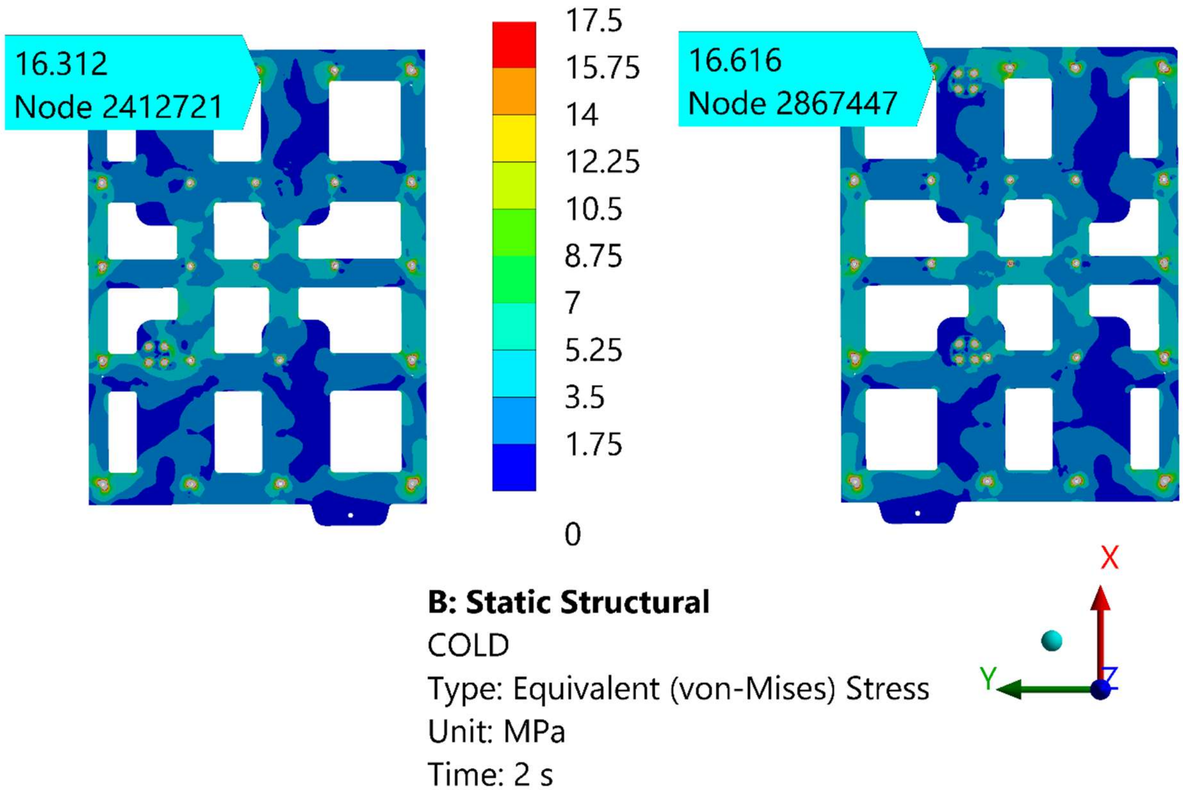

Figure 73: Plot of adapter plate stress when the CRU is cooled but not submerged.

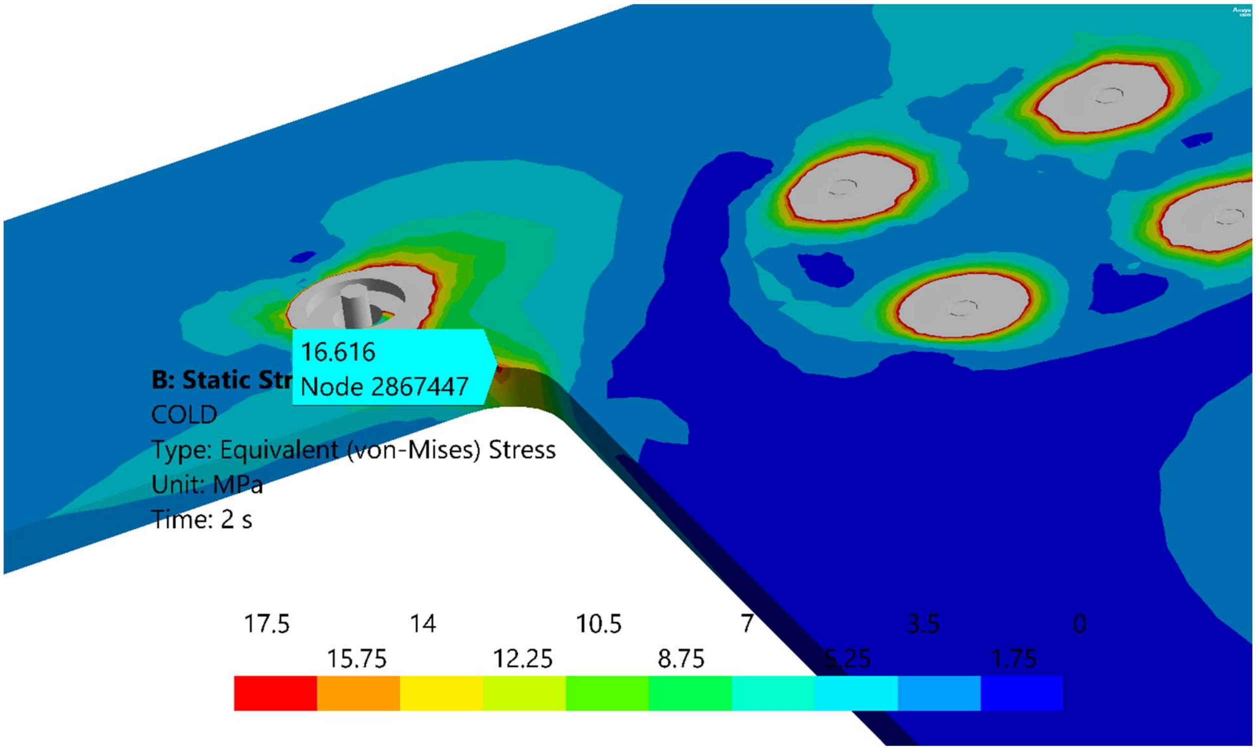

Figure 74: Detailed view of the location of maximum stress on the adapter plate when the CRU is cooled but not submerged.

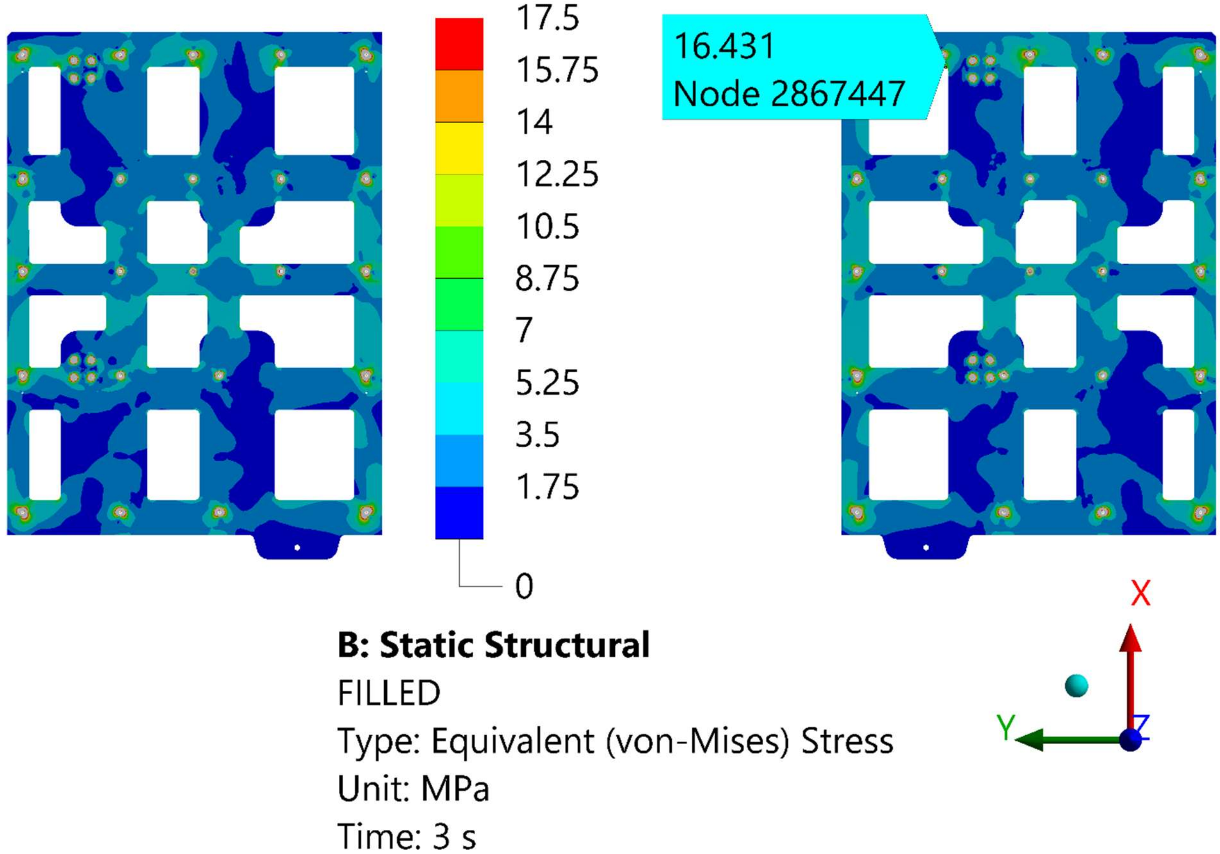

Figure 75: Stress plot of the adapter plates when the CRU is submerged in liquid argon.

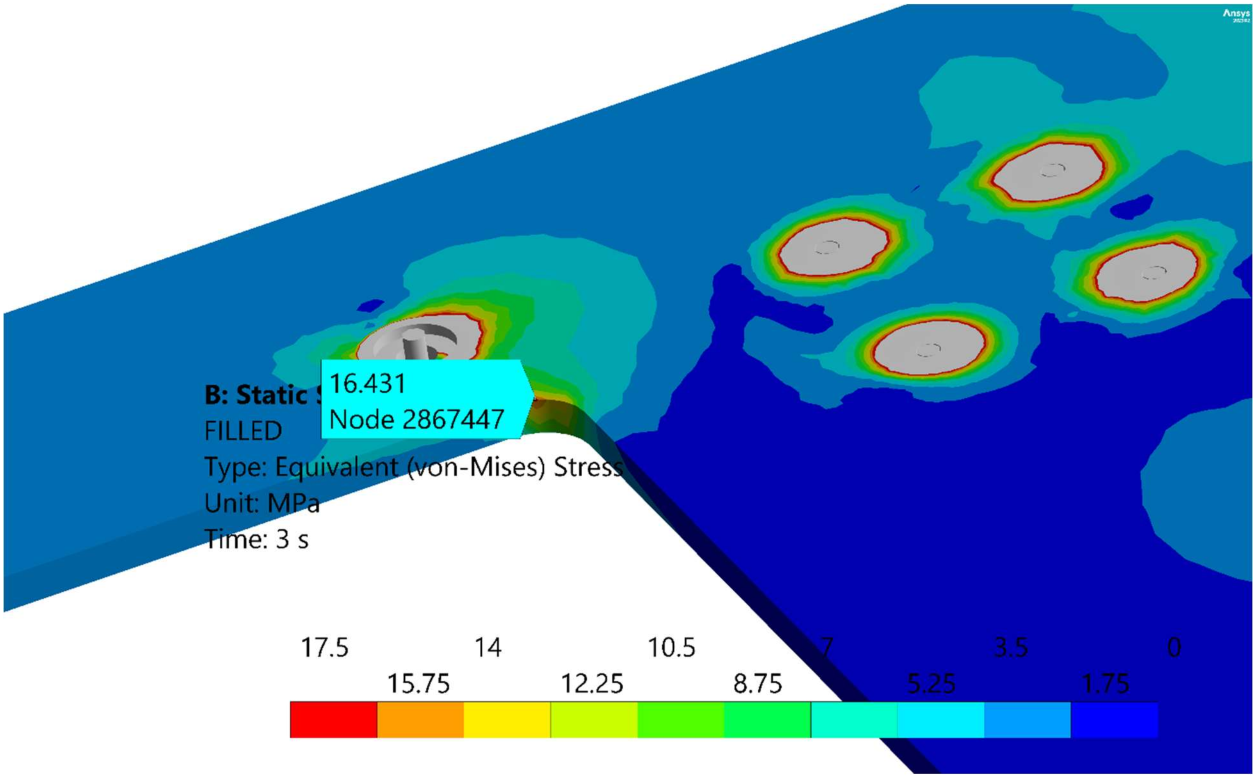

Figure 76: Detailed view of the location of maximum stress within the adapter plate when the CRU is submerged.

3.4.9. Stress Result Summary

After analyzing the results of the FE model, all components of the CRU meet the DUNE Compliance Office requirements. Therefore, it is possible to install the bottom layer of the vertical drift detector as 160 CRUs resting on the membrane floor, with the contraction of the CRUs guided by controlling the coefficient of friction of the support-floor interface without damaging the CRU. This study also validates the design of the adapter plates proposed by UW to attach these supports to the CRU. A table summarizing the results, load factors, strength factors, and the safety factor on compliance is below.

Table 5: Summary of Finite Element Model Results

Analysis	Component	von Mises Stress [MPa]	Load Factor [-]	Yield Strength [MPa]	Strength Factor [-]	Allowable Stress [MPa]	Safety Factor
Install Position Prior to Fill (293 K, 1G)	Composite Skin	8.1	1.4	205.0	0.245	50.2	4.4
	G-10 Adapter Plate	3.5	1.4	250.0	0.245	61.3	12.5
	Composite Beams	5.3	1.4	250.0	0.245	61.3	8.3
	Anodes	1.6	1.4	440.0	0.245	107.8	48.3
	Anode Spacers	7.3	1.4	90.9	0.245	22.3	2.2
	BDE	4.2	1.4	440.0	0.245	107.8	18.5
Install Position During Cooldown (87 K, 1G)	Composite Skin	23.95	1.4	205.0	0.245	50.2	1.5
	G-10 Adapter Plate	16.62	1.4	250.0	0.245	61.3	2.6
	Composite Beams	12.68	1.4	250.0	0.245	61.3	3.5
	Anodes	21.21	1.4	440.0	0.245	107.8	3.6
	Anode Spacers	13.43	1.4	90.9	0.245	22.3	1.2
	BDE	28.82	1.4	440.0	0.245	107.8	2.7
Submerged Install Position (87 K, Buoyant)	Composite Skin	25.13	1.4	205.0	0.215	44.1	1.3
	G-10 Adapter Plate	16.43	1.4	250.0	0.215	53.8	2.3
	Composite Beams	12.82	1.4	250.0	0.215	53.8	3.0
	Anodes	21.19	1.4	440.0	0.215	94.6	3.2
	Anode Spacers	13.27	1.4	90.9	0.215	19.5	1.1
	BDE	28.81	1.4	440.0	0.215	94.6	2.3

4. Conclusions

This thesis analyzed two different approaches of installing the lower detection plane of the Vertical Drift far detector for the Deep Underground Neutrino Experiment. The first approach is to combine two Charge Readout Units together into Charge Readout Planes and then install these resting on the membrane floor of the cryostat. This creates 80 installation sites for installation of 200-260 kg components. The work performed for this installation method was designing custom tooling consisting of an Installation Truss, and Pneumatic Truss Retrieval System. Both systems were fully developed but had significant drawbacks. Each truss and retrieval system were expensive and required additional effort to set-up and dismantle between CRP installations. The process required at least two people for truss set-up and four to five people for retrieval system operation and disassembly. This system also never eliminated the requirement for a human to be working directly underneath a CRP, instead only provided a rigid structure to hold it in place while this work was performed. Ultimately, after presenting this system to the DUNE collaboration, it was decided to investigate the feasibility of installing individual CRUs instead of CRPs.

The CRUs and many components attached to the CRU were designed around the original plan of installing CRPs into the detector. Additionally, installing CRUs into the cryostat requires double the amount of CRU bottom supports. This created a drive to reduce the cost of the bottom supports and led to a new sliding design. Additionally, the adapter plate had to become larger to accommodate more bottom support positions. This increase in size led to increased costs and concerns with impeding argon flow through and around the CRUs. Both of these issues were addressed by switching to CNC machined pockets instead of drilled holes. These design changes, and the fact that the CRUs were designed to be installed as part of a CRU meant that the design needed to be validated. This validation was performed by creating a finite element model of a CRU and the loads that the CRU would be exposed to when resting on the floor in the cryostat. The analysis included the CRU at room temperature, with no argon contact, the CRU being cooled by argon vapor as the cryostat begins to fill, and the CRU being completely submerged in the cryostat. The results of the model showed that the CRU would not be damaged during use in these conditions. Therefore, it is feasible to create the bottom plane of the vertical drift detector using CRUs.

5. References

[1] "Neutrino Oscillations Nab Nobel Prize." Accessed: Jan. 15, 2024. [Online]. Available: http://www.aps.org/publications/apsnews/201511/nobel.cfm

[2] "Neutrino beam," DUNE at LBNF. Accessed: Sep. 12, 2023. [Online]. Available: https://lbnf-dune.fnal.gov/how-it-works/neutrino-beam

[3] L. Biron, "How do you make the world's most powerful neutrino beam?," symmetry magazine. Accessed: Sep. 12, 2023. [Online]. Available: https://www.symmetrymagazine.org/article/how-do-you-make-the-worlds-most-powerful-neutrino-beam?language_content_entity=und

[4] "Detectors and computing," DUNE at LBNF. Accessed: Aug. 30, 2024. [Online]. Available: https://lbnf-dune.fnal.gov/how-it-works/detectors-and-computing

[5] "BNL | Deep Underground Neutrino Experiment (DUNE)." Accessed: Sep. 12, 2023. [Online]. Available: https://www.bnl.gov/science/dune.php

[6] "Cryostats and cryogenics," DUNE at LBNF. Accessed: Aug. 22, 2024. [Online]. Available: https://lbnf-dune.fnal.gov/how-it-works/cryostats-and-cryogenics

[7] ModTruss Inc, "Aluminmum ModTruss Load Tables," ModTruss. Accessed: Aug. 30, 2024. [Online]. Available: https://www.modtruss.com/wp-content/uploads/2021/12/2.-6-Aluminmum-Truss-Load-Tables_ModTruss.pdf

[8] "Theory | C5.1 Euler's Buckling Formula | Solid Mechanics II." Accessed: Jan. 29, 2025. [Online]. Available: http://www.engineeringcorecourses.com/solidmechanics2/C5-buckling/C5.1-eulers-buckling-formula/theory/

[9] F. Xu, K. Yoshimura, and H. Mizuta, "Experimental Study on Friction Properties of Rubber Material: Influence of Surface Roughness on Sliding Friction," *Procedia Eng.*, vol. 68, pp. 19–23, Jan. 2013, doi: 10.1016/j.proeng.2013.12.141.

[10] E. Edge and E. E. LLC, “Aluminum Channel Table Aluminum Association Standard.” Accessed: Dec. 04, 2023. [Online]. Available: https://www.engineersedge.com/materials/aluminum_channel_table_13661.htm

[11] King Plastic Corporation, “King-KPC-HDPE-Literature.pdf,” King Plastic Corporation. Accessed: Feb. 20, 2024. [Online]. Available: https://www.kingplastic.com/wp-content/uploads/2014/05/King-KPC-HDPE-Literature.pdf

[12] Plastics Pipe Institute, *Chapter 2 - Materials_Final_B.pdf*. Accessed: Nov. 12, 2024. [Online]. Available: https://plasticpipe.org/common/Uploaded%20files/1-PPI/Manuals-Design%20Guides/Drainage%20Handbook/1st%20Edition/Chapter%202%20-%20Materials_Final_B.pdf

[13] “Aluminum 6061-T6; 6061-T651.” Accessed: Oct. 09, 2023. [Online]. Available: https://www.matweb.com/search/DataSheet.aspx?MatGUID=b8d536e0b9b54bd7b69e4124d8f1d20a

[14] J. Truchon, “Testing of CRP Supports for the Deep Underground Neutrino Experiment,” University of Wisconsin - Madison, Madison, WI, 2023.

[15] S. Canva, “FEM validation – Bottom CRP.” Sep. 30, 2024.

[16] “Cryogenics Material Properties.” Accessed: Feb. 13, 2025. [Online]. Available: https://trc.nist.gov/cryogenics/materials/materialproperties.htm

[17] “cryogenic material properties G-10 CR (Fiberglass Epoxy).” Accessed: Nov. 08, 2024. [Online]. Available: https://trc.nist.gov/cryogenics/materials/G-10%20CR%20Fiberglass%20Epoxy/G10CRFiberglassEpoxy_rev.htm

[18] “cryogenic material properties 316 Stainless.” Accessed: Nov. 08, 2024. [Online]. Available: https://trc.nist.gov/cryogenics/materials/316Stainless/316Stainless_rev.htm

[19] “cryogenic material properties OFHC Copper.” Accessed: Feb. 18, 2025. [Online]. Available: https://trc.nist.gov/cryogenics/materials/OFHC%20Copper/OFHC_Copper_rev1.htm

[20] "Oxygen-free Electronic Copper (OFE), UNS C10100, H00 Temper, flat products." Accessed: Mar. 14, 2025. [Online]. Available: https://www.matweb.com/search/DataSheet.aspx?MatGUID=f128a589e6db41028e611ae1eab803b7

[21] Inc. ANSYS and Granta Design, "Copper, C10100, hard (oxygen-free electronic h.c. copper), wrought (hc-Cu-OFE (h); C101)." 2025.

[22] Z. Zhang and G. Hartwig, "Low-temperature viscoelastic behavior of unidirectional carbon composites," *Cryogenics*, vol. 38, no. 4, pp. 401–405, Apr. 1998, doi: 10.1016/S0011-2275(98)00022-8.

[23] R. Juvinall and K. Marshek, *Fundamentals of Machine Componet Design*, Seventh. Wiley, 2020.

[24] "Metric Stainless Steel Bolt Strength Chart, Class 50, 70, 80 and 100," Monster Bolts. Accessed: Mar. 11, 2025. [Online]. Available: https://monsterbolts.com/pages/stainless-steel-grades

[25] N. P. Mastricola and R. Singh, "Nonlinear load-deflection and stiffness characteristics of coned springs in four primary configurations," *Mech. Mach. Theory*, vol. 116, pp. 513–528, Oct. 2017, doi: 10.1016/j.mechmachtheory.2017.06.006.

[26] "304 Stainless Steel." Accessed: Mar. 11, 2025. [Online]. Available: https://www.matweb.com/search/DataSheet.aspx?MatGUID=abc4415b0f8b490387e3c922237098da&ckck=1

[27] "316 Stainless Steel, annealed sheet." Accessed: Mar. 11, 2025. [Online]. Available: https://www.matweb.com/search/DataSheet.aspx?MatGUID=50f320bd1daf4fa7965448c30d3114ad

6. Appendix A:

Long Baseline Neutrino Facility, DUNE & CERN Neutrino Platform		https://edms.cern.ch/document/2823005	
Document EDMS identifier: **282xxxx**	Fermilab LBNF DocDB:	Created: 24/02/2023	
		Last Modified: 09/03/2023	Rev. No.: **2.0**

CRP INSTALATION TRUSS ASSEMBLY PROCEDURE AND LOAD ANALYSIS

Prepared by:	Checked by:	To be approved by:
I. Jentz Y. Pandiscas		

Distribution List

History of Changes

Date	***Version***	***Changes/Comments***	***Authors***
07/03/2023	*1*	*First draft*	*YP*
30/06/2023	*2*	*Second Draft Revised with Truss Stability*	*YP*

Table of Contents

Table of Contents

Introduction

This procedure describes the assembly of the CRP Installation Truss and its use. This document will provide clear instructions with visuals to safely handle and install the truss system, and then move it into position under the CRP. Additionally, all relevant force analysis on load bearing members of the truss is provided. The document will first show all components and discuss terminology through CAD diagrams. The procedure for assembly of the installation truss follows, and the document concludes with the force analysis.

The CRP Installation Truss is designed to support the CRP so that a technician can safely work underneath the CRP as comfortabey as possible. The CRP is desinged to be assembled in a cryostat without the use of any tools, and all hardware remains captive to the system. This design makes assembly easier, safer, and faster while minimizing the risk of damaging the cryostat floor by dropping tools and hardware.

General Component Diagrams

Figure 1 shows a computer-generated drawing of the complete truss assembly with each component numbered. This assembly has one of the longer F-sections mounted as high up as possible to maximize clearance for a person to work underneath the CRP. Each number is entered in Table 1 with a part name and a brief description.

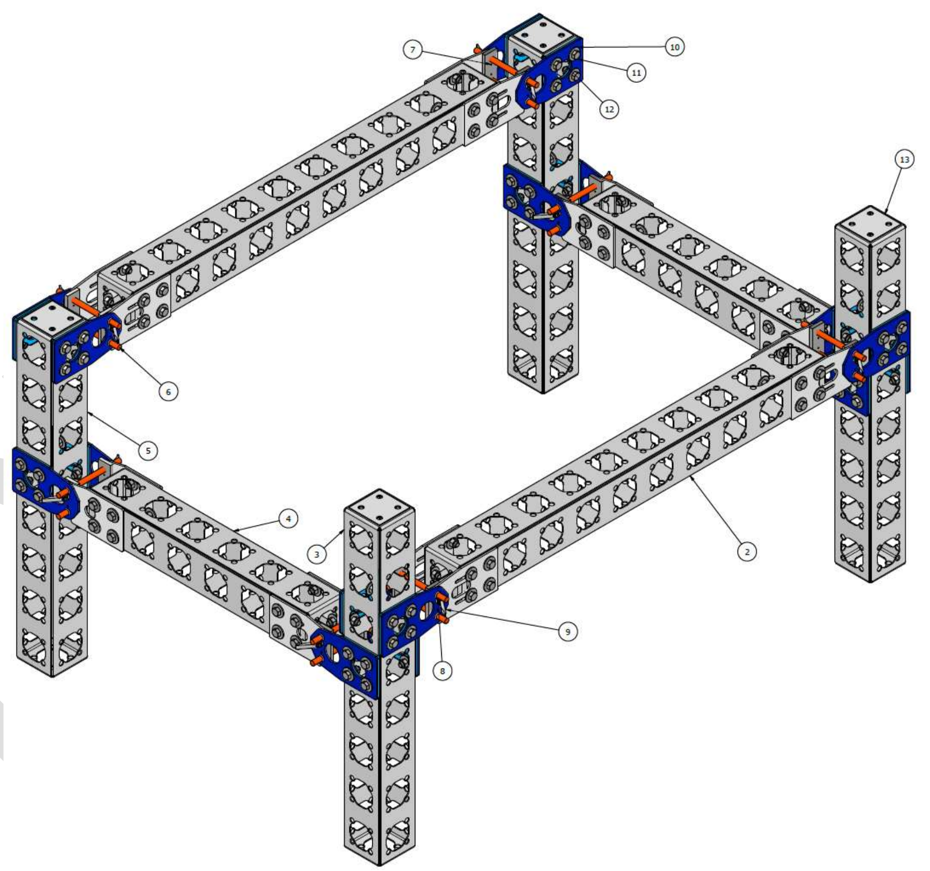

Figure 77 - CAD drawing of full Installation Truss for Module 0 with component balloons for clarity.

Table 6: Numbered items in assembly drawing from Figure 1 with descriptions and names that will be used in this document.

ITE M	QTY	PART NAME	DESCRIPTION

1	1	H section D	2 Columns and 1 D beam assembled.
2	2	F-Section	Beam F, longest beam length needed for FAR detector, with hook plates to interface with aluminium bar.
3	1	Column Corner-MIR	Corner Column, includes bars and mounts, supports CRP.
4	1	D-Section	Beam D, shortest beam length needed for FAR detector, with hook plates to interface with aluminium bar.
5	1	Column End	Column without corner mounts in case fourth high beam is cumbersome. Supports CRP.
6	2	Drop Lock Bars	5/8 in annular aluminium bars secured by snap rings into aluminium plates attached to columns.
7	4	Rod Plate	1/2 in steel plate for cam handle thread.
8	12	Camlock Washer	Cam Handle Component.
9	12	Camlock	Cam Handle Component.
10	16	ANSI B18.22.1 - 5/8 - wide - Type A	Plain Washer (Inch) Type A and B
11	8	ANSI/ASME B18.2.1 - 5/8-11 UNC - 1.75, HBI	Hex Bolt - UNC (Regular Thread - Inch)
12	8	ANSI B18.2.2 - 5/8 - 11, HNI	Hex Nuts (Inch Series) Hex Nut
13	4	Base Plate	Used to show where feet for CRP go. Actual feet are omitted for visibility in this drawing

The above was intended to provide a brief overview of the entire truss that will be used for Module 0 testing. Figure 2 shows a diagram of column side of the joint between the beam sections and the columns; Table 2 contains details about the numbered components in Figure 2.

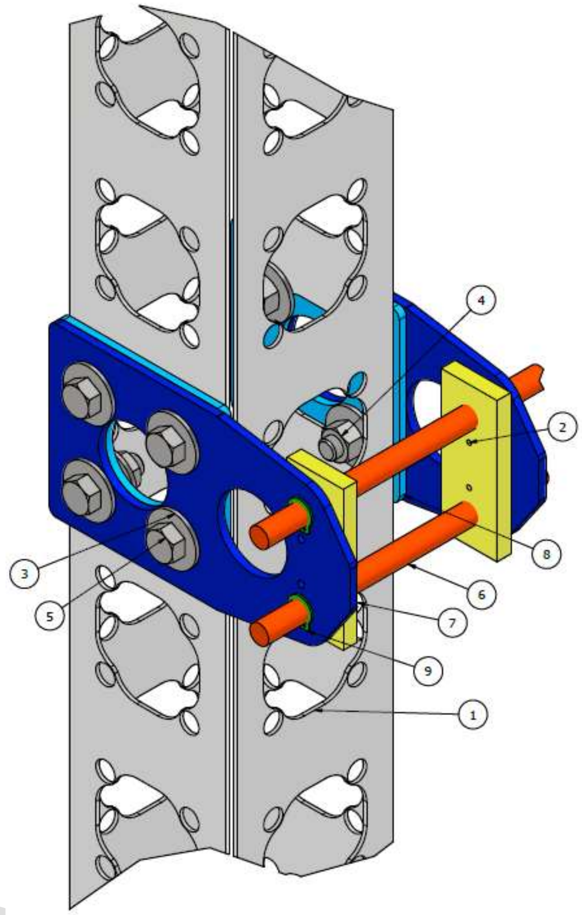

Figure 78 – Detailed drawing of the column side of the beam to column joint.

Table 7 – Description of numbered components in Figure 2.

ITEM	QTY	PART NUMBER	DESCRIPTION
1	1	MT-TR-06-06-48	1.22 m column purchased from ModTruss.
2	2	Rod Plate	Steel plate that is threaded for cam handle threads.
3	16	ANSI B18.22.1 - 5/8 - wide - Type A	Plain Washer (Inch) Type A and B
4	8	ANSI B18.2.2 - 5/8 - 11, HNI	Hex Nuts (Inch Series) Hex Nut
5	8	ANSI/ASME B18.2.1 - 5/8-11 UNC - 1.75, HBI	Hex Bolt - UNC (Regular Thread - Inch)
6	2	Hanger Bar	1.5875 cm aluminium bar that section hook plates interface with.
7	2	Drop Lock Plate Bars	Plate mounted to the column to hold the Hanger Bar
8	2	Drop Lock Plate Spacer	Spacer plate between column and bar plates to create clearance for the section hook plates.
9	4	90341A119_Self-Locking External Retaining Rings	Snap rings that retain the Hanger Bars to the Drop Lock Plate Bars.

Lastly the joint between the cross beams and the columns from the beam side is shown in Figure 3, and the numbered parts are described in Table 3. The cross beams are of different lenghts and have bespoke hook plates for each beam length to match the spans required in the Far Detector due to the corrugated cryostat floor.

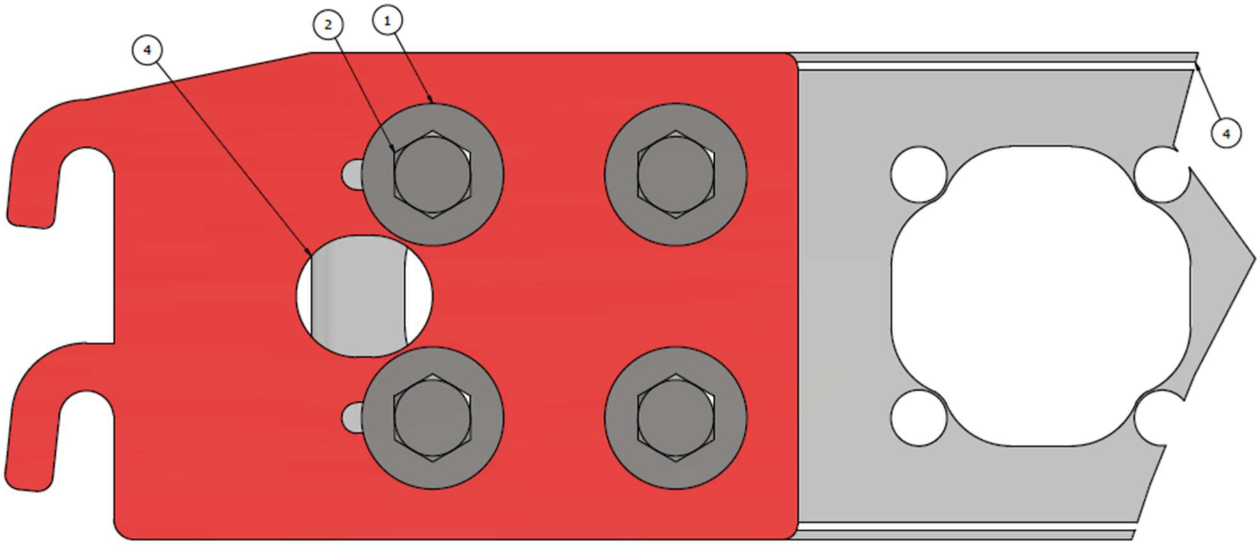

Figure 79 – Diagram of the side view of a cross beam. Note that the red hook plate is one of 3 geometries depending on the beam span needed.

Table 8 – List and description of parts in Figure 3.

ITEM	QTY	PART NUMBER	DESCRIPTION
1	32	ANSI B18.22.1 - 5/8 - wide - Type A	Plain Washer (Inch) Type A and B
2	16	ANSI/ASME B18.2.1 - 5/8-11 UNC - 1.5, HBI	Hex Bolt - UNC (Regular Thread - Inch)
3	16	ANSI B18.2.2 - 5/8 - 11, HNI	Hex Nuts (Inch Series) Hex Nut
4	1	MT-TR-06-06-36	0.914 m beam section from ModTruss.
5	4	Drop Lock Plate Hooks-D	Hook plate bespoke for this span.

Truss Assembly Procedure

This section of the document provides instructions for assembling the CRP Instalation Truss system. While the components are designed to minimize mass, they are still large and difficult to handle by a single person. Therefore <u>assembly requires a minimum of two people.</u>

1. Place two columns approximately 1.36 m apart. Ensure that the two columns are oriented in the direction that you want the long cross beams. Note that two of the columns have the Drop Lock Bar assembly at the highest setting. When placing the two columns in this step, one column should be of the high configuration, and the other should be of the low configuration.

Figure 80 – Columns placed in relative position. Note the two different configurations. Take care to include one of each configuration.

2. Have one person insert the Drop Lock Hook Plates into the column joint, while the other person supports the free end of the beam. The hooks fit between the Drop Lock Bar Plates and the steel Rod Plates. It is imperative that the hooks engage with bars fully and that the Rod Plate can provide clamping pressure to the Hook Plates.

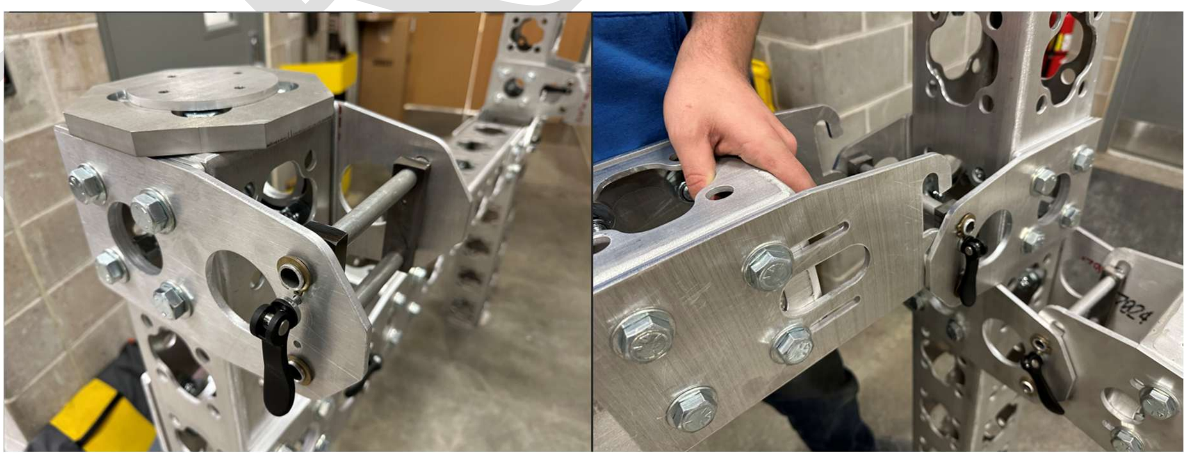

Figure 81 – The column joint during the assembly process. Note that the Hook Plates insert between the Rod Plate and the Bar Plates.

3. Perform a similar process on the other side of the beam with the other column. One person should insert the Drop Lock Hooks into the column joint, while the other holds the truss system steady. At the end of this step one has an H-section with none of the cam handles in the locked position yet.

Figure 82 – Two people completing step 3. Note that as one person is inserting the hooks the other is stabilizing the system.

4. Tighten the camlock mechanisms by turning the thread and folding the camlock handle towards the beam.

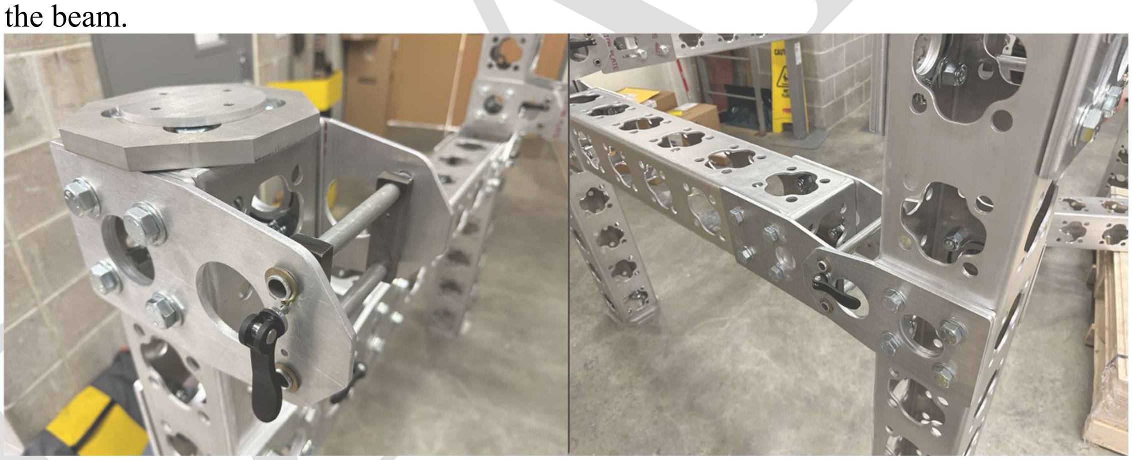

Figure 83 – The camlock mechanism on the left is in the unlocked position, while the camlock mechanism on the right is in the locked position.

5. Repeat steps 1 through 4 to build another indentical H-section.
6. The next step is to install the two F-section cross beams. The installation process is much like installing the D-sections. The F-sections are significantly longer at 2.04 m. Two people, one at each end are necessary to maneuver the beam into position. Just like with the D-section, one

person should insert the Drop Lock Hooks into the joint, ensuring full engagement with the bars, while the other supports the other end of the beam.

7.

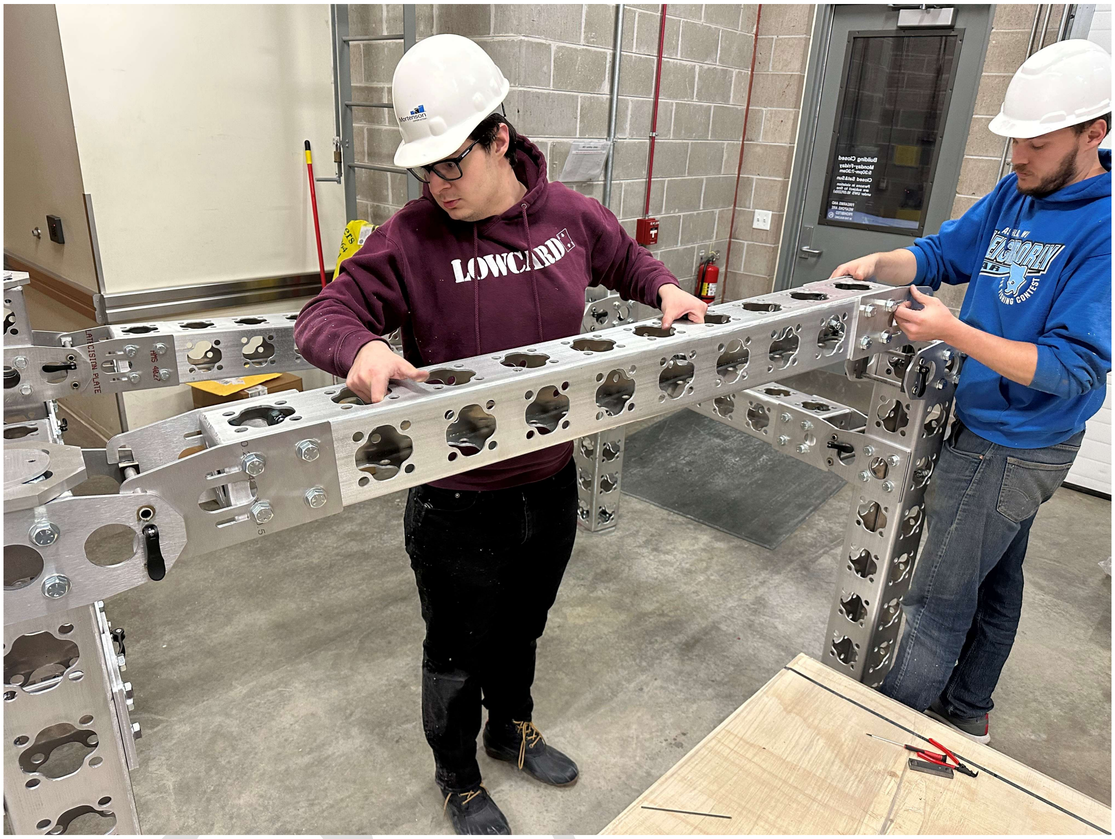

Figure 84 – Installing the final F-section. Note that one person is stabilizing while the other inserts the hook plates into one joint.

Disassembly of the Installation Truss is the reverse of assembly. Thus, follow steps 1-7 in reverse order, and unlocking camlocks when appropriate. <u>Two people are required for disassembly.</u>

Truss Load Analysis

Only the columns support the load of the CRP, with the cross beams providing stability for the system. For a slender column, the primary mode of failure is buckling, which happens much sooner than plastic yielding for metals. Thus for this analysis, only column buckling will be analyzed.

For this analysis the mass of the CRP was coservatively estimated to be 300 kg. The center of gravity of the CRP is is in the center of the truss lifting device, so each of the four columns supports one quarter of the total load from the CRP, or 75 kg.

Figure 85 – Example of truss loading with mock CRP with mass 310 kg.

The truss section manufacturer rates a column with a length of 3.04 m as being able to support 5,633 kg. The table below is from the manufacturer and states the capacities and their underlying assumptions.

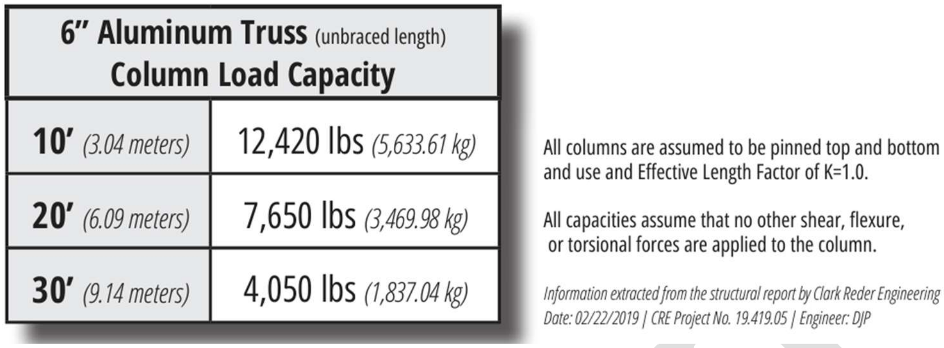

6" Aluminum Truss (unbraced length) Column Load Capacity	
10' (3.04 meters)	12,420 lbs (5,633.61 kg)
20' (6.09 meters)	7,650 lbs (3,469.98 kg)
30' (9.14 meters)	4,050 lbs (1,837.04 kg)

All columns are assumed to be pinned top and bottom and use and Effective Length Factor of K=1.0.

All capacities assume that no other shear, flexure, or torsional forces are applied to the column.

Information extracted from the structural report by Clark Reder Engineering Date: 02/22/2019 | CRE Project No. 19.419.05 | Engineer: DJP

Figure 86 – ModTruss Column Load Rating table

As the column is only 1.22 m tall it can support a higher load as seen in Euler's beam buckling equation below. Our implementation of the column can be assumed to be a fixed, free condition. Requiring an the effective length factor to take the value of 2. Thus the rated values should be divided by 2 as the scaling is linear with values of K, as seen in equation 1. Thus the maximum buckling load for a 3.04m column with fixed-free boundary conditions is 2816 kg.

Equation 1 – Euler Beam Buckling Equation

$$P_{cr} = \frac{E * I * \pi^2}{KL^2}$$

Symbol	Parameter
E	Material Modulus of Elasticity
I	Minimum Second Moment of Area
L	Column Length
K	Column Effective Length Factor
P_{cr}	Critical Buckling Load

Thus, the buckling load for a shorter length column can be related to the the buckling load for the longer column with equation 2 since the modulus of elasticity and minum mass moment of area are the same for the two lengths.

Equation 2 – Critical Buckling Load Relation

$$P_{cr,S} = P_{cr,L} * \frac{L_L^2}{L_S^2}$$

Symbol	Parameter
$P_{cr,S}$	Critcal Buckling Load for Short Column
$P_{cr,L}$	Critical Buckling Load for the Long Column
L_L^2	Length of the Long Column
L_S^2	Length of the Short Column

Performing the calculation, the critical buckling load of the 1.22 m column is 6.25 times that of the 3.04 m column. Using the relevant values leads to a critcal buckling load of 17,605 kg for the 1.22 m column, which is several orders of magnitude larger than the designed load.

Truss Stability Analysis

Another safety requirement of the truss is that it must be stable so that it is safe to work under and around. To perform the calculations, the most conservative load case was considered. This being the lightest and narrowest truss configuration possible to assemble with the designed components. This truss would be a DDDD configuration, which would have a total mass of 113.9 kg. CAD software was used to compute the location of the center of gravity which is pictured in Figure 11. The CG is the point denoted by a yellow sphere in the figure.

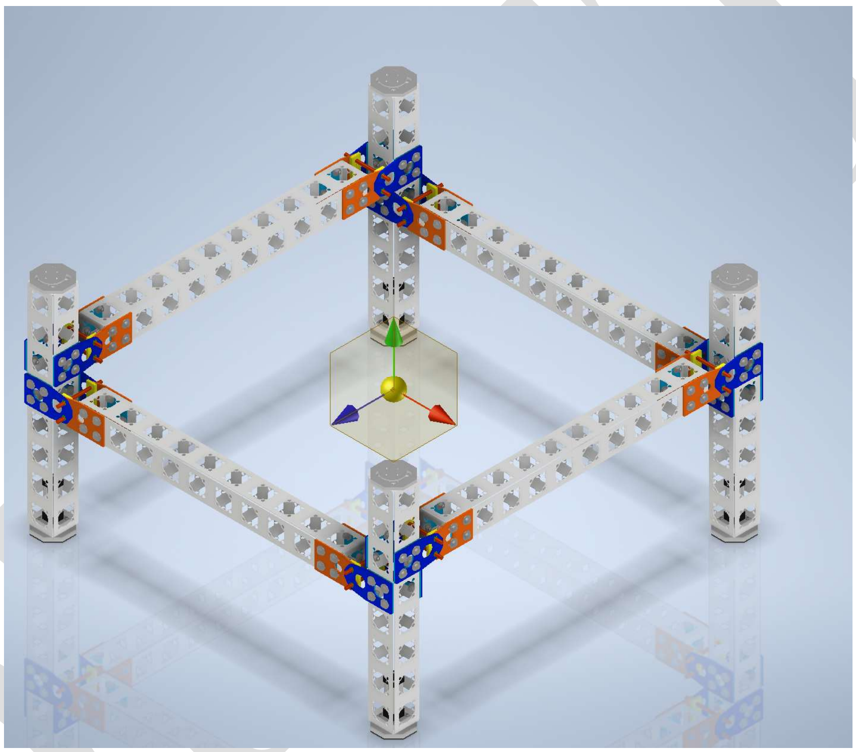

Figure 87- Location of CG for the DDDD truss configuration

Figure 12 shows a diagram which describes the loading considered for the rest of this stability analysis. In this loading we consider a load applied to the top of the truss, which is at 1.2m in along the y-axis, and applied to the farthest location beam at 2.16m in the x-axis. The CG of the truss is located at 1.08m in the x-axis. Per the design of the truss, the CG of the CRP is aligned with the CG of the truss. And thus the total weight of the system acts along the CG of the truss pictured. Moments are to be summed around the point at the bottom left, indicated by a blue dot. The vector F is the force applied, and the vector f is the friction force.

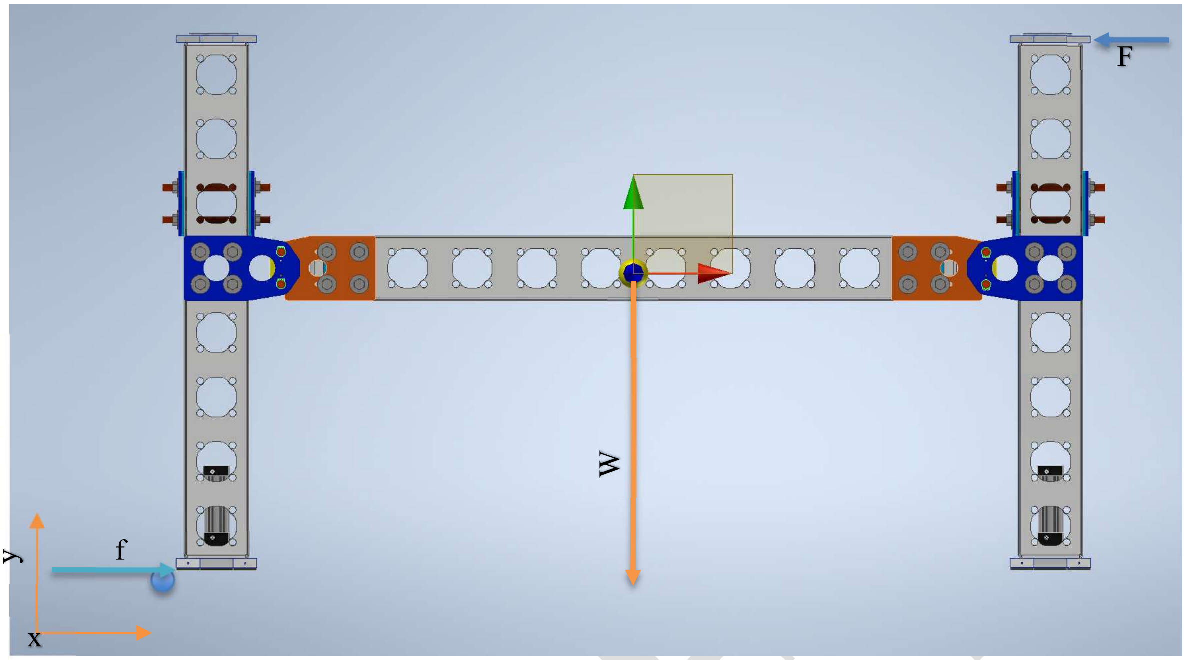

Figure 88 - Free Body Diagram of Truss

The truss can move in one of two ways, firslty it can translate. This occurs when the force applied exceeds the maximum static friciton reaction. The static friction reaction can be caluclated as the normal force multiplied by a coefficient of friction. To resolve for the normal force we assume that each column supports exaclty one-quarter of the total load of the CRP and the truss. For the truss and CRP to translate, all four of the CRP feet must break free. Thus the total force applied must be four times the friction reaction of one column. The feet of the truss are coated with a neoprene rubber to prevent damage to the floor and provide greater grip. The coefficient of friction used is the published value for rubber on stainless steel which is 0.64.

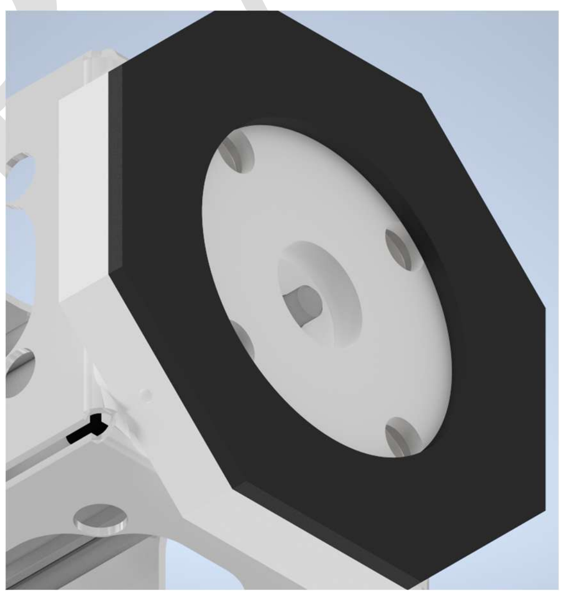

Figure 89 - Truss Rubber Foot

Equation 3 – Calculation of Normal Reaction Force

$$F_N = \frac{W_{CRP} + W_{truss}}{4}$$

Symbol	Parameter
W_{CRP}	Weight of the CRP
W_{truss}	Weight of the Truss
F_N	Normal Reaction Force

It then follows that the friction reaction force is calculated as:

Equation 4 - Calculation of Friction Reaction Force

$$F_f = 4\mu F_N$$

Symbol	Parameter
μ	Coefficient of Friction
F_f	Friction Reaction Force.
F_N	Normal Reaction Force

Performing the calculations with the appropriate values, we find that the total force applied to cause the truss to translate is 2315N.

The other possibility is that the truss overturns. For this to happen the CG of the truss must be moved so that it is over the point that moments are acting about. To investigate whether this is likely, we calculate the required force applied to the same location as in Figure 12 for any of the truss to begin lifitng off the ground. This is down by summing moments about the point in Figure 12. The truss and CRP have a self correcting moment which is equal to the weight of the system multiplied by the distance in x of the CG. The applied force has a moment which is equal to the magnitude of the force multiplied by 1.2m. Solving the balance about the point results in the required force being 3256N to begin overcoming the self-correcting moment. We find that overturning of the truss and CRP system would require significantly more than this.

7. Appendix B:

Long Baseline Neutrino Facility, DUNE & CERN Neutrino Platform	https://edms.cern.ch/document/2823005		
Document EDMS identifier: **282xxxx**	Fermilab LBNF DocDB:	Created: 02/05/2024	
		Last Modified: 02/05/2024	Rev. No.: **1.0**

CRP INSTALLATION TRUSS RETRIEVAL SYSTEM LOAD ANALYSIS

Prepared by:	Checked by:	To be approved by:
Y. Pandiscas		

Distribution List

History of Changes

Date	*Version*	*Changes/Comments*	*Authors*
02/05/2024	*1*	*First draft*	*YP*

Table of Contents

Table of Contents

Introduction

This document details the components of the CRP Installation Truss Retrieval System and provides relevant load, stress, and deformation analysis. This document is not intended to provide a load analysis to be fed back into the design. The geometry of the design is set by the clearances required by the cryostat, available components, and the pneumatics. The Retrieval System is intended to allow the Installation Truss to be removed from underneath the CRP without placing personnel under a suspended load. The equipment in this system and document is not designed to protect a technician from a lifted load. The system instead relies on placing personnel fully outside the perimeter of the CRP. In addition, the system is not designed to support the CRP in any position. For this system to operate correctly, the CRP must be lifted and off the Installation Truss. This document does not cover the Installation Truss in detail, and only covers information that is essential to understanding the Retrieval System. For information about the Installation Truss see its own document under EDMS.

Brief Overview of Retrieval System Components

The retrieval system can be described as a larger system comprised of several subsystems. One of which is the Pneumatic sub-system attached to the truss and an auxiliary cart that has an air supply and controls for the pneumatic sub-system as well as the CRP lifting device. The next sub-system is the rail system which will support the weight of the Installation Truss and retrieval train cars and allow the Installation Truss to roll back to the false floor while keeping it captive in other directions. Lastly, the retrieval trains are what the installation truss will interface with to allow it to roll on the tracks.

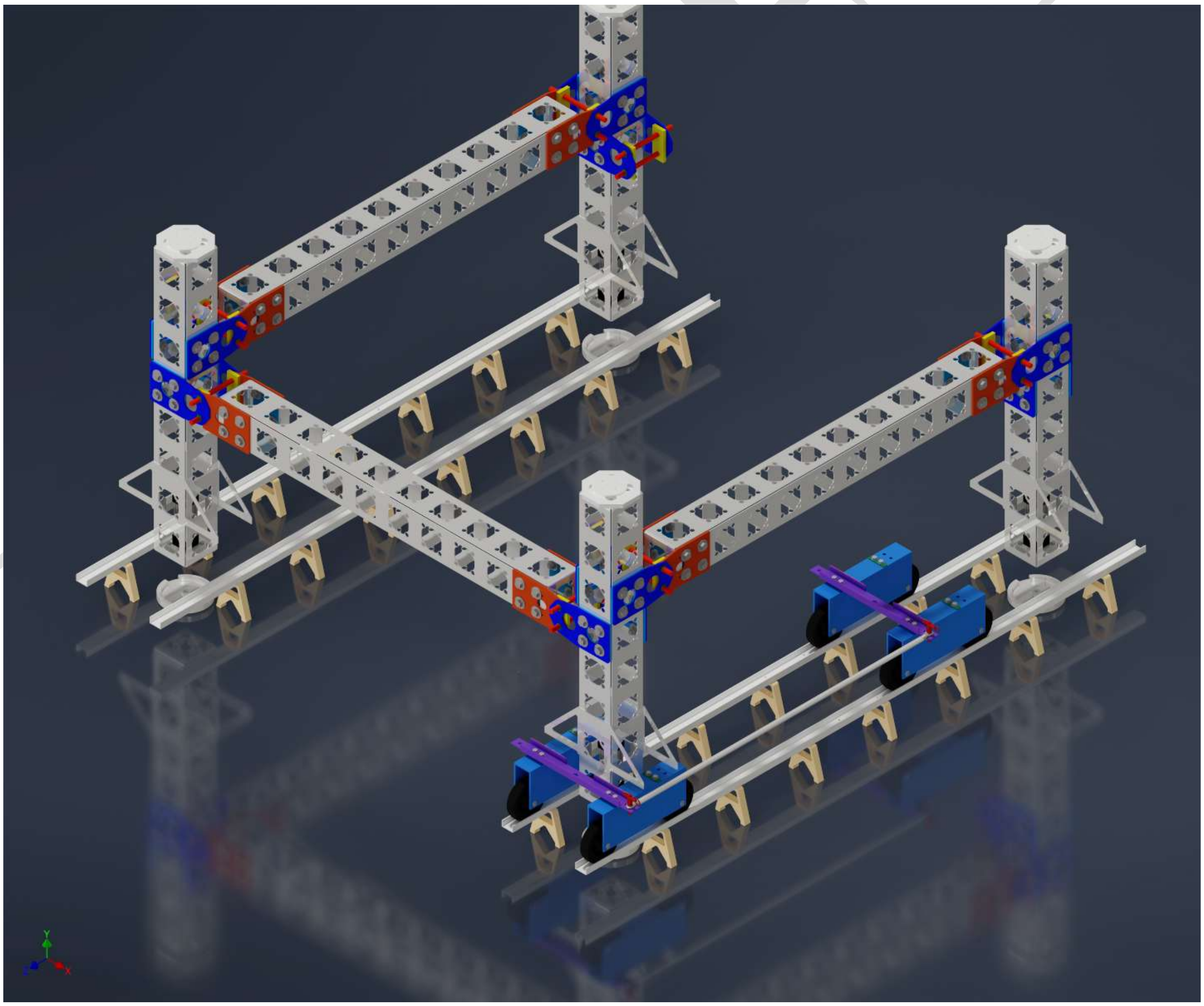

The pneumatic sub-system is responsible for moving the Installation Truss up and down. The system is comprised of several components; pneumatic cylinders rigidly attached to Installation Truss with mechanical fasteners, a pressure regulator which controls the pressure in the sub-system, a flow valve which controls the flow rate and therefore actuation rate, a directional control valve which controls the direction of the pneumatic cylinder piston and therefore the position of the truss, and all associated plumbing.

The rail system is composed of an aluminum channel with designation 2 x 0.577 by the Aluminum Association. Fixed to this with countersunk M4 fasteners are custom designed and manufactured spacer blocks that align the track with the corrugations in the cryostat membrane floor. These blocks are made from High-Density Poly Ethelyne (HDPE) from the King Plastic Corporation. The contact surfaces between the spacer blocks and the membrane floor have compressive foam attached with an acrylic adhesive. The spacer blocks will ultimately support a portion of the load of the truss and retrieval cars.

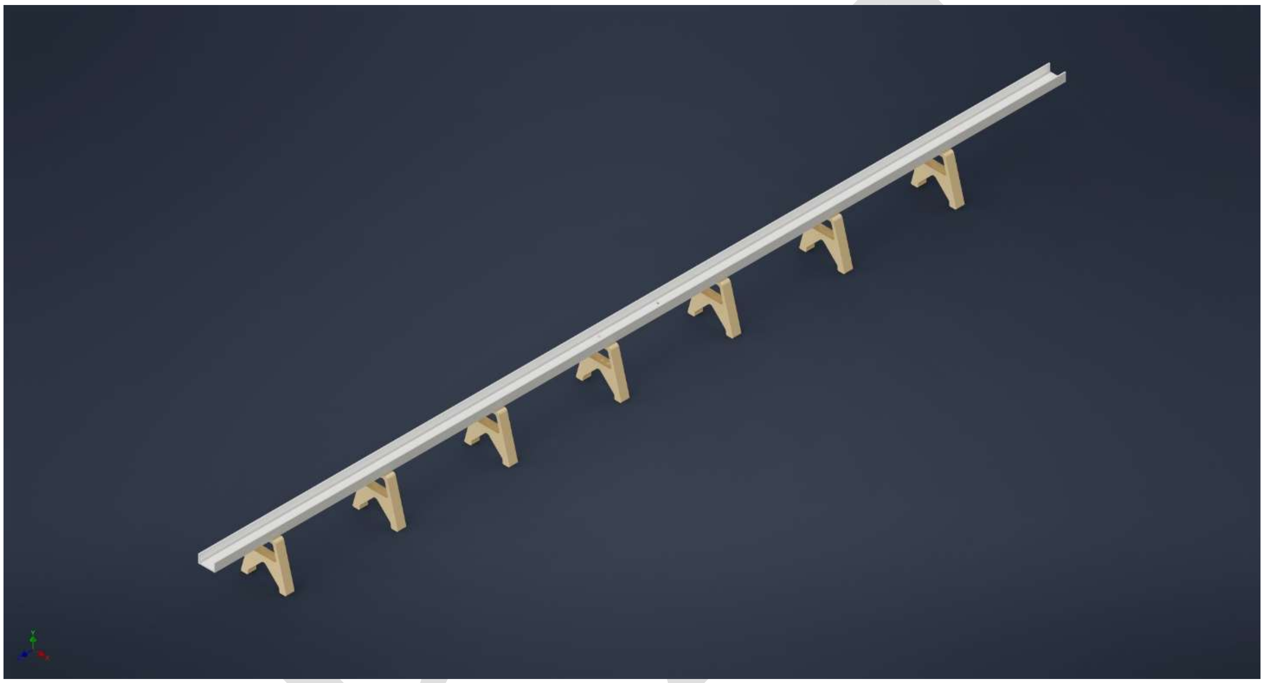

Figure 90: 3D render of a section of one of the truss retrieval rails.

The retrieval trains are composed of several cars linked together using clevis rods that are pinned together using captive quick release pins. Each train also has a spherical joint that allows a technician to pull on the train with a rigid manipulator rod from nearly any angle remotely. Each car is composed of two semi pneumatic wheels on axles, that are held together using a section of rectangular aluminum tube. The tube has laser cut acrylic pieces to captivate the gusset plate mounted to the Installation Truss once the cars contact the Truss. The top face of the carts interface with the bottom face of the gusset plates, with an intermediate layer of rubber to prevent any metal-to-metal contact.

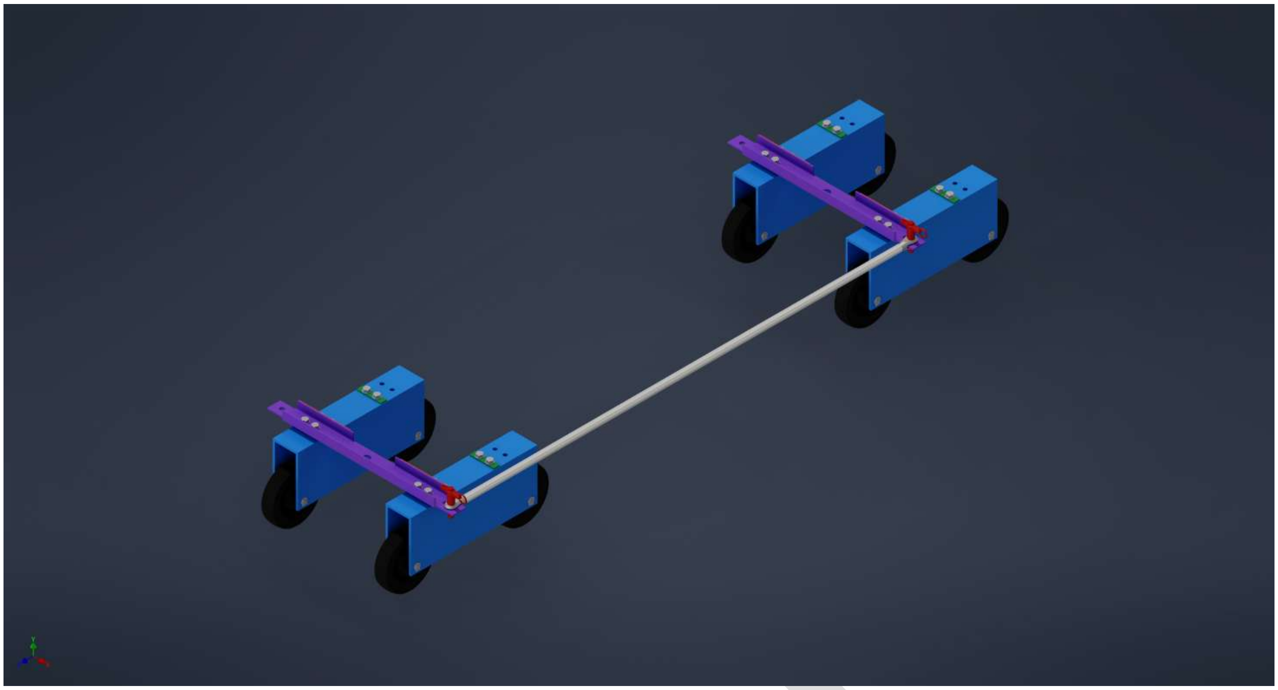

Figure 91: 3D Render of the retrieval trains without the manipulator rod.

Design of Truss Retrieval Components and Purpose of this Document

The design and overall geometry/size of the components were driven by two main factors. The first of these factors is the height of the false floor at the far detector. From several drawings in EDMS this height is 128.3mm. Therefore, the bottom face of the rails must lie at this height. This drives the minimum height of the rail spacer blocks. The truss column has a uniform spacing of bolts which the gusset plates must attach to. Several of the bottom sections of the column cannot be used for this purpose due to the pneumatic cylinders consuming most of the space. These dimensions drive the requirement for the position of the top face of the truss retrieval carts. In addition, the gusset plate width is driven by the spacing of the corrugations within the cryostat membrane floor, which is 34cm.

The other major driving factor in fixing the design is the availability and cost of off-the-shelf components while still minimizing the mass of the system. Maximizing the use of purchased components saves cost in the form of engineering design work and machining work. This is how we landed on using 6” x 3” x 0.1875” aluminum extrusion to make the carts. The gusset plate is 1/8” thick aluminum as it is easy to laser cut and allows us to effectively remove as much material as possible quickly.

Therefore, the dimensions of this system are largely set by the criteria mentioned above. We have already designed the smallest practical components possible to be used in this design. Further, the purpose of this document and the analysis contained within is not to perform topology optimization or to further select lighter stock. The analysis is to confirm that the designed system meets its functional requirements safely, with enough safety factors to be confident using the system at the far detector site. When safety factors are described, and they are large, the only way to remove mass would be to machine the components which adds complexity, time to manufacture, and ultimately cost.

Pneumatic Sub-system Analysis

Introduction and Pneumatic Cylinder Selection

As mentioned in the introduction of this document, the pneumatic sub-system controls the vertical position of the truss. It does this by pressurizing different sections of 4 double-acting pneumatic cylinders. The pneumatic cylinder chosen was a Parker-Hannifin 4MA unit customized for this application. The piston bore was chosen to be 50.8mm as this was the smallest size offered in a double acting configuration.

The throw of the cylinder is 165.1mm which was chosen to ensure that the system could be raised to the false floor height of 128.3mm while accommodating the rails with appropriate clearance.

Pressure and Pressure Regulator

The mass of the smallest configuration of the Installation Truss with Retrieval System equipment installed is estimated to be no more than 91kg. The largest configuration was estimated to be no more than 113.4kg. This allows us to calculate the pressure needed to maintain static equilibrium at a given position of the cylinder. Knowing that the CRP is estimated to have mass of 255kg allows us to check what pressure would be needed to lift the lightest truss with a CRP on top of it. Note that because there are 4 pneumatic cylinders, this cancels with the division by 4 in calculating the area. The mass supported is the mass of the heaviest installation truss when determining the minimum required operating pressure, and the mass of the CRP with the lightest installation truss when determining the maximum allowable pressure.

$$P_{operating} = \frac{m_{truss,max}\,g}{\pi D^2} \tag{1}$$

$$P_{allowable} = \frac{\left(m_{truss,min} + m_{CRP}\right)g}{\pi D^2} \tag{2}$$

Solving the equations above provides a minimum operating gauge pressure of 1.37 bar, and a maximum allowable pressure of 4.18 bar. To meet these requirements a pressure regulator with a maximum allowable pressure of less than 4.3 bar was chosen. The unit chosen is the Parker-Hannifin 06E22A11AC, which has a maximum allowable pressure of 4.14 bar. The unit is also convenient as it provides filtering and lubricating properties which aid in the operation of the pneumatic cylinders.

Controlling Flow Direction

To control the direction of flow a manually actuated directional control valve with 5 ports and 2 positions was chosen. The valve lever has a detent spring which keeps the valve position to the rod retracted position until an operator moves it. When the operator releases the lever, the spring returns the lever and valve to the default position again. One of the 5 ports is the single pressure feed to the system and is connected to the outlet of the pressure regulator. Two of the ports are connected to one chamber of the cylinder each. The order of the connections is crucial as reversing these will cause the cylinder to behave in a manner opposite to the design intent, the correct orientation is in figure ___ below. The final two ports are used as exhaust to ambient, which allows the chambers of the pneumatic cylinder to vent to atmosphere. Diagrams of the two different valve positions are shown in *Figure 92* and *Figure 93* below. In the diagrams the red lines represent pneumatic lines that are at gauge pressure by design, whereas the blue lines represent lines which are at ambient pressure by design. The first diagram shows the top chamber of the pneumatic cylinder being pressurized, while the bottom chamber is vented to atmosphere, which extends the cylinder rod. The second diagram depicts the reverse, where the bottom chamber is pressurized, and the top chamber is in communication with the ambient pressure. This configuration retracts the rod.

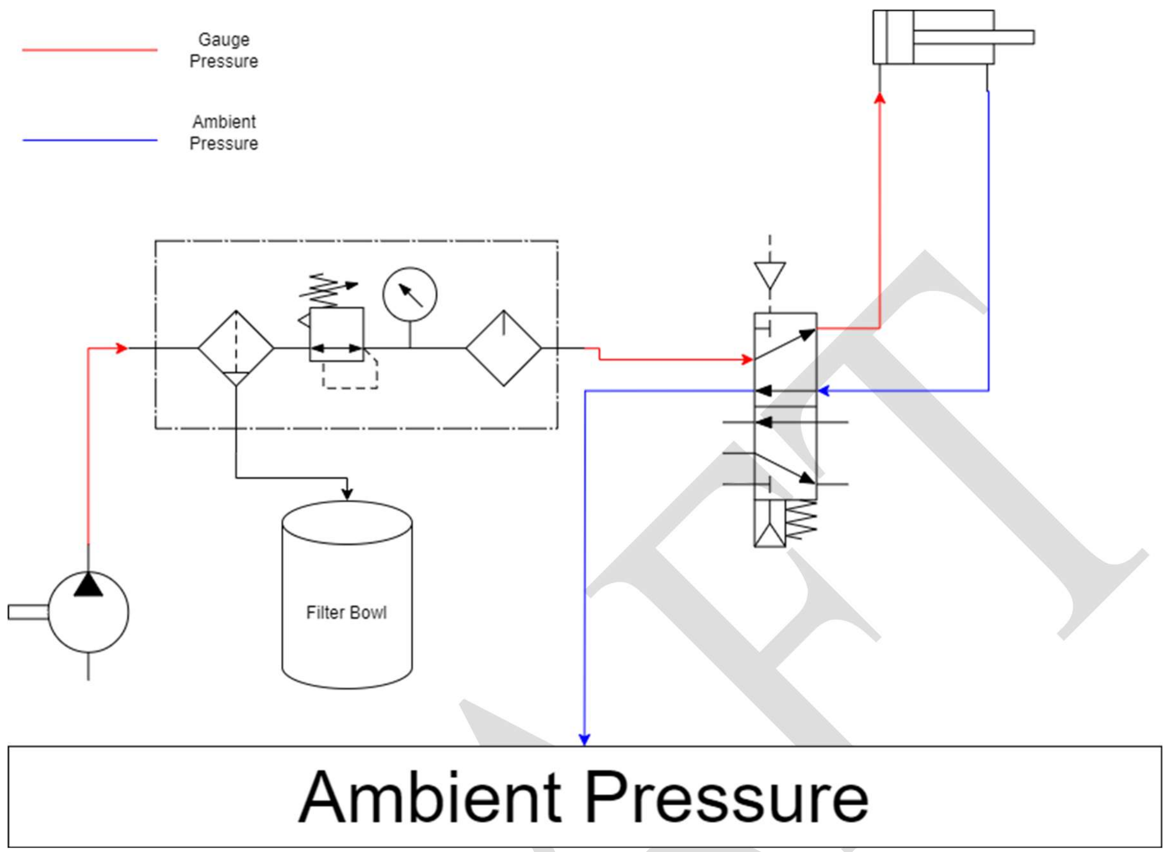

Figure 92: P&ID diagram of the extension position of the truss retrieval system pneumatics showing the path from the compressor to the Filter Regulator and Lubricator (FRL), the directional control valve, and finally the cylinders. Note that the FRL relieves pressure that is above its set point. Also note that the directional control valve is lever actuated with a detent spring.

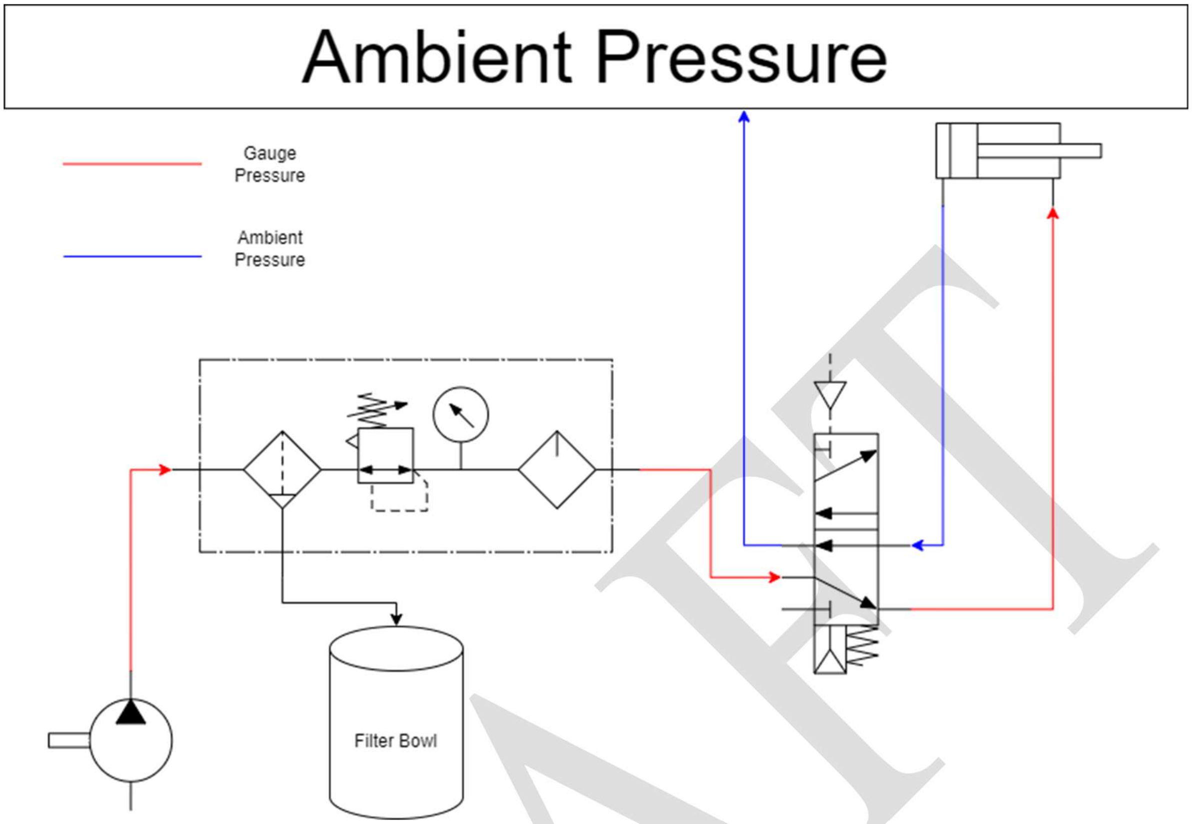

Figure 93: P&ID diagram of the retraction position of the truss retrieval system pneumatics showing the path from the compressor to the Filter Regulator and Lubricator (FRL), the directional control valve, and finally the cylinders. Note that the FRL relieves pressure that is above its set point. Also note that the directional control valve is lever actuated with a detent spring.

Pneumatic System Safety Features

The pneumatic system has several features to ensure safe and reliable operation. The first of which has mentioned before is a pressure regulator which automatically vents any pressure that exceeds the set point, regardless of flow direction. This ensures that even if there is a spike in pressure anywhere in the system for any reason, it will immediately be vented to ambient. Additionally, the regulator cannot be set above 4.14 bar so that the CRP cannot be raised with the pneumatic system. The next safety feature is the directional control valve's detent spring system which returns the valve to the pneumatic cylinder rod's retracted position. This ensures that the default configuration when supported by the floor is the lower position. This also allows for the feet to remain retracted by default without human action when the truss is being moved along the rails. Trip hazards are avoided by containing all lines that connect cylinder together 'loops' within the existing truss members. The only lines which are not contained within the truss members are the lines from the DCV to the upper and lower loops, and the line from the compressor through to the DCV. These are to be covered with a cable raceway to minimize trips and falls.

Pneumatics Failure Modes

Situations where the line pressure is interrupted were also considered during the design of the system. Pressure can be lost at any of three locations. Pressure can be lost at the feed to the 5/2 valve, where in this situation neither chamber of the cylinders can receive pressure. Pressure can be lost in the top loop, where the top chambers of the cylinders can no longer receive pressure. Lastly pressure can be lost in the bottom loop, where the bottom chambers would no longer receive pressure. This can happen when the system is supported on the floor or by the gusset plates, or when the system is being raised/lowered and extended/retracted. Each possibility was tested, and the results are summarized in

Table 9 below. In the table, feed is used to describe pressure coming from the compressor, and bot is used as an abbreviation for the word bottom.

Table 9: Table summarizing the test results of cylinder behavior during a pressure line failure.

Test Scenario Number	**1**	**2**	**3**	**4**	**5**	**6**	**7**	**8**	**9**	**10**	**11**	**12**
Line Interrupt	Feed	Top	Bot.	Feed	Top	Bot	Feed	Top	Bot.	Feed	Top	Bot.
Support	Floor	Floor	Floor	Floor	Floor	Floor	Gusset	Gusset	Gusset	Gusset	Gusset	Gusset
Requested Action	Raise	Raise	Raise	Lower	Lower	Lower	Retract	Retract	Retract	Extend	Extend	Extend
Result	Floor	Floor	Raised No Retract	Floor, No Lift	Floor, No Lift	Floor, Can Lift, No Retract	Foot Drop	Retract	Foot Drop	Extend No Retract	Extend	Extend No Retract

From the observations in the table above, there are conditions that would cause the Installation Truss bottom feet to drop to the level of the membrane floor corrugations. There is not a way to eliminate the possibility of a loss of pressure, or to positively retain the foot without adding significant complexity and bulk that would hinder the usability of the system. Therefore, the bottom of the feet has a nitrile rubber covering applied to them, and the edges are beveled to eliminate sharp edges. This significantly reduces the risk of damaging the floor.

Rail System Analysis

Spacer Block Introduction

The spacer blocks ultimately support the load of the truss and retrieval carts riding on the rails. Due to being mounted to the rails which will need to be manipulated by personnel, reducing mass is also an important target. Thus, pockets are machined out of the structure to reduce mass. The blocks are made from HDPE due to its light weight, low cost, machinability, and its inability to generate conductive particulate. The angled surfaces at the bottom of the block are designed to reference the block's position with respect to the corrugations in the membrane floor. Foam is applied to these surfaces to achieve the best fit. A 3D model of the spacer block with the foam adhered to the contact surfaces is shown in *Figure 94* below.

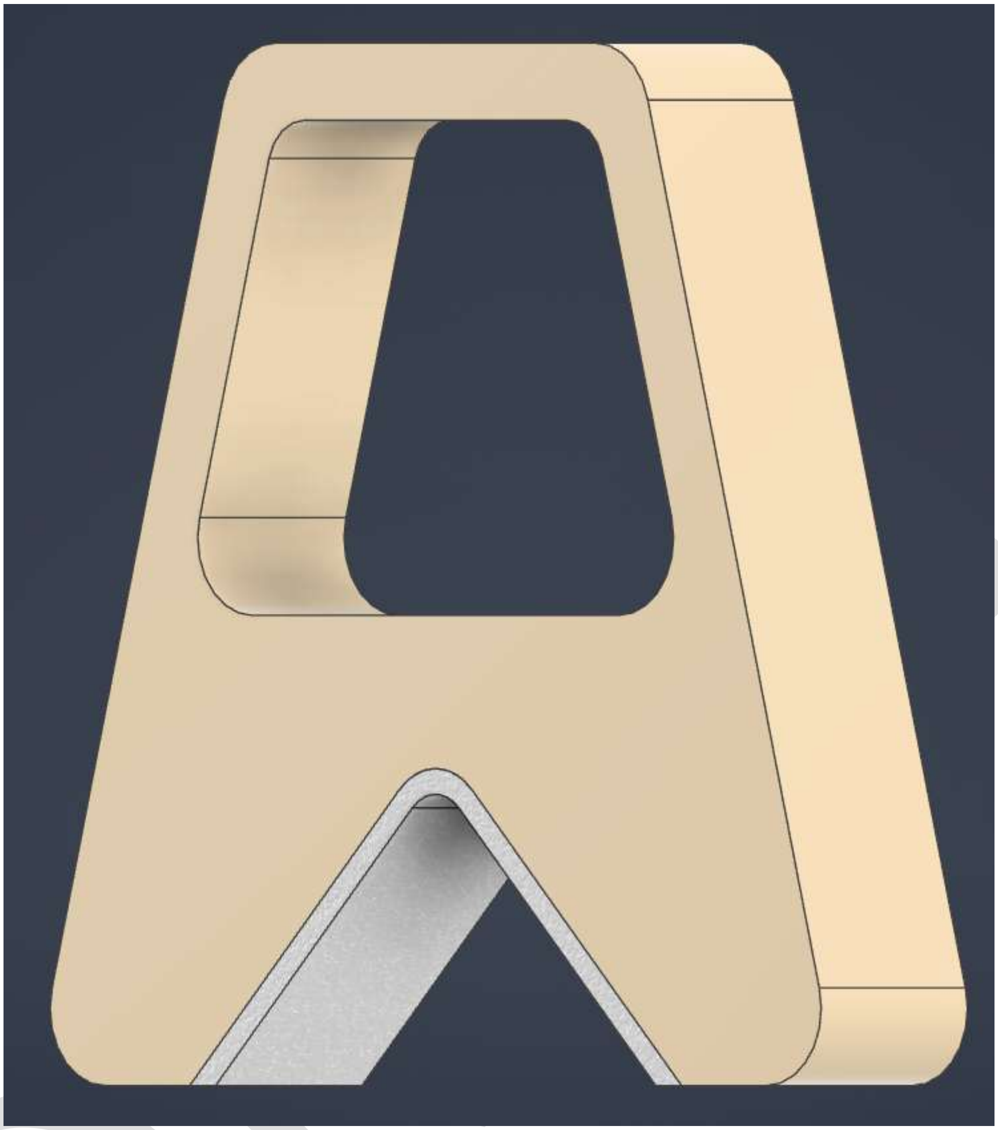

Figure 94: 3D Render of the Spacer Block with the foam applied to the contact surfaces shown in white.

Spacer Block Load and Stress Analysis

The force supported by the spacer blocks was modelled as supporting 1/8 of the mass of a 100kg Installation Truss, which was treated as a 12.5kg load on the block, plus 5kg to represent ¼ of the retrieval cart system. This results in a load of 17.5kg being analyzed. Due to the complex geometry of the blocks, there is no easy analytical calculation that can be performed to accurately describe the state of stress experienced by the block. Therefore, simulation tools were used to analyze the spacer block design before performing material testing.

ANSYS Mechanical APDL was the simulation tool chosen to perform this stress analysis. The model was created by importing the geometry from an external CAD package as an IGES file and creating a volume with the imported geometry. The clearance holes for the fasteners were omitted to simplify the model. The model was constrained in the y and z directions along the inner edges of the block as seen in *Figure 95* below. Additionally, a node along the line of symmetry of the block was constrained in the x direction to enforce symmetry. The load was applied as a uniform pressure loading on the top area by taking the force of gravity on the supported mass and dividing by the top area, again see *Figure 95* for a graphical representation of the loading. Note that the units of the ANSYS model are in the U.S customary system of inches, lbf, psi, etc. in all the images shown of the results. The values reported in the text and tables of the report are in the SI unit system.

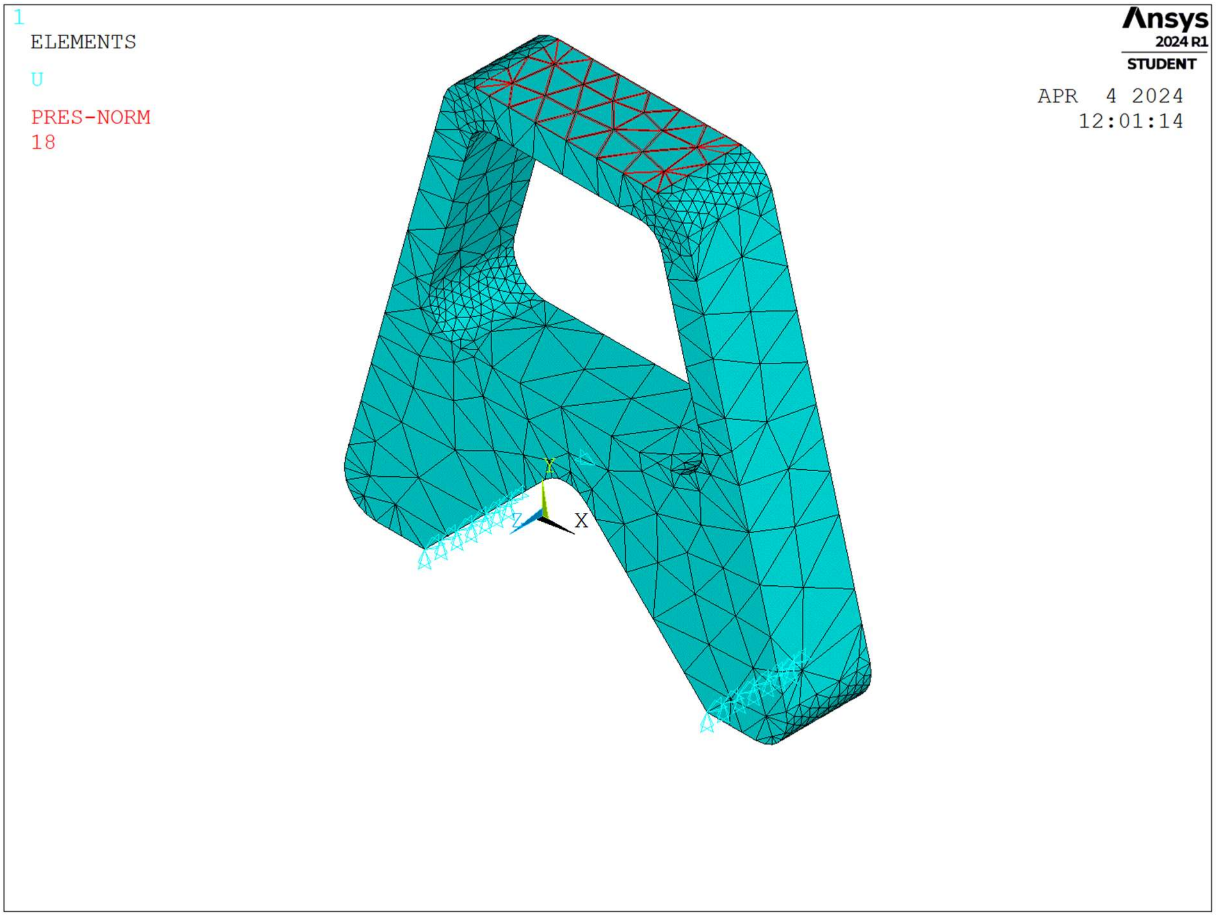

Figure 95: Spacer block mechanical simulation parameters. Note the displacement constraints at the edges of the angled contact surfaces and along the line of symmetry. Observe the pressure load of 18psi applied to the top area. This is equivalent to the block supporting 17.77kg.

The model was meshed using ANSYS's built in meshing tools as the finest autogenerated free mesh (no user defined mapping) of SOLID187 elements. These elements are 10 node tetrahedral 3D elements which are capable of quadratic and linear deformation. This results in a mesh of 4748 elements corresponding to about 45000 nodes. The material was modelled as a homogeneous, isotropic, and elastic material with a Young's Modulus 1.758 GPa and a Poisson's ratio of 0.45. The elastic modulus corresponds to a manufacturer claim of the tensile modulus. While the manufacturer does not provide a Poisson's ratio, HDPE ranges from 0.4 to 0.45. I chose 0.45 as the conservative value, as the increased strain due to the material expanding would increase von Mises stresses. The model parameters are shown in *Table 10* below.

Table 10: Summary of ANSYS structural model parameters in SI units.

Quantity	Value	Unit
Elements	4748	N/A
Nodes	8419	N/A
Young's Modulus	1.758	GPa
Poisson's Ratio	0.45	Unitless

Yield Stress	28.27	MPa

The model's validity is checked within the model by verifying the reaction solution is correct. There are no loads applied in the x or z direction, and therefore there should be negligible reaction forces in both of these directions. Inspecting the reaction solution within ANSYS shows that the model does in fact solve for reaction forces that are essentially zero in both directions. The pressure load of 124.1 kPa applied in the negative y direction on the top face of the block corresponds to a total of 174.3N of force applied in the negative y-direction. Checking the y component of the reaction forces within ANSYS shows that the model correctly solved for this value. These values are listed below in *Figure 96*. As the model corresponds well to these analytical values, we can have confidence that the following stress and deformations are likely correct.

```
THE FOLLOWING X,Y,Z SOLUTIONS ARE IN THE GLOBAL COORDINATE SYSTEM

 NODE       FX            FY          FZ
   23                   1.0546     0.82014
   24                   1.4110    -0.87141
   29                   1.0804     0.76907
   30                   1.5909     -1.0974
  442                   3.5175     0.50747
  443                   2.3513     0.30473
  444                   3.8213    -0.28258
  445                   2.5566     0.13615
  446                   4.8809    -0.61450
  533                   3.3969     0.48075
  534                   2.0478     0.27888
  535                   4.3364    -0.77651E-001
  536                   2.3591    -0.64472E-001
  537                   4.7817    -0.28921
 2299  0.15405E-009

TOTAL VALUES
VALUE   0.15405E-009   39.186      -0.46787E-010
```

Figure 96: ANSYS printout of reaction force values in the US Customary unit System, where the forces are listed in lbf. Note that the y direction reaction solution is highlighted, and that the others are essentially zero.

Having established confidence in the model by verifying the reaction solution with analytical calculations, we move on to studying the stress and deformation solutions of the model. Before we begin analyzing the degree of freedom and stress solutions it is important to understand the failure criteria. As the spacer blocks are intended to be reused, yielding will be considered a failure as it compromises the dimensional stability of the system. The von Mises stress will be used to determine when yielding occurs as it is a commonly accepted failure model that predicts yielding. The yield stress provided by the plastic supplier is 28.27 MPa or 4100 psi.

Figure 97, below is a plot of the simulated stresses within the spacer block, with units in psi. The maximum stresses occur on the top surface of the block, at the corners of the surface. This makes sense, as the squared corners act as stress risers, but make machining easier. The maximum of these stresses is 2.45 MPa or 355.419 psi. Taking the yield stress and dividing it by the maximum von Mises stress, as in equation ___, gives the factor of safety against yield. This value is 11.54, which is a very large safety factor, which provides confidence that this design will be more than sufficient for its purpose despite slight differences in the modelled load case from the real use case.

$$SF = \frac{\sigma_{yield}}{\sigma_{max}} \tag{3}$$

Symbol	Definition

SF	Safety Factor or Factor of Safety
σ_{yield}	Yield stress of the material
σ_{max}	Maximum predicted stress

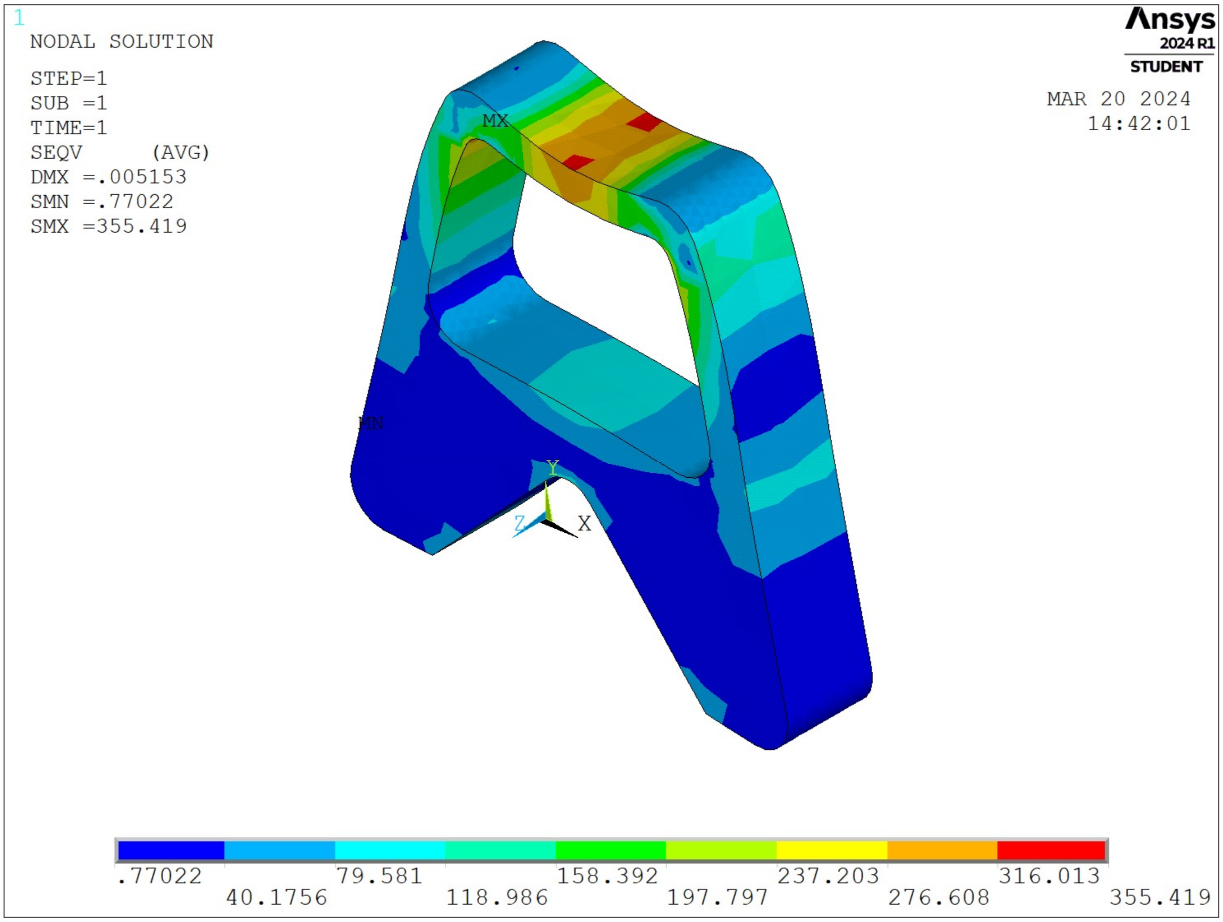

Figure 97: Contour Plot of von Mises stresses predicted by ANSYS in psi.

Additionally of importance are the deformations of the block in its loaded condition. Firstly, the y displacement is important to ensure that the retrieval cars can roll back to on top of the false floor, without having to overcome a large grade. Second, the displacement of the angled contact surfaces is of interest, as they ensure that the system is aligned properly. The nodal y displacements are shown in a contour plot which is *Figure 98* below, and there is a contour plot of the nodal vector sum of displacements shown in the subsequent figure. The plots from ANSYS are once again in the US unit system, and the values are shown in inches.

The largest y displacement occurs on the thin top section of the block that supports the load of the Installation Truss and retrieval cars. Material was removed underneath this section to minimize the mass of the blocks. This is logical and agrees with simple beam theory. The magnitude of this displacement is 0.1306mm, or 0.005144 inches. This value is sufficiently small enough to not impact the function of the system and is well within the designed clearances.

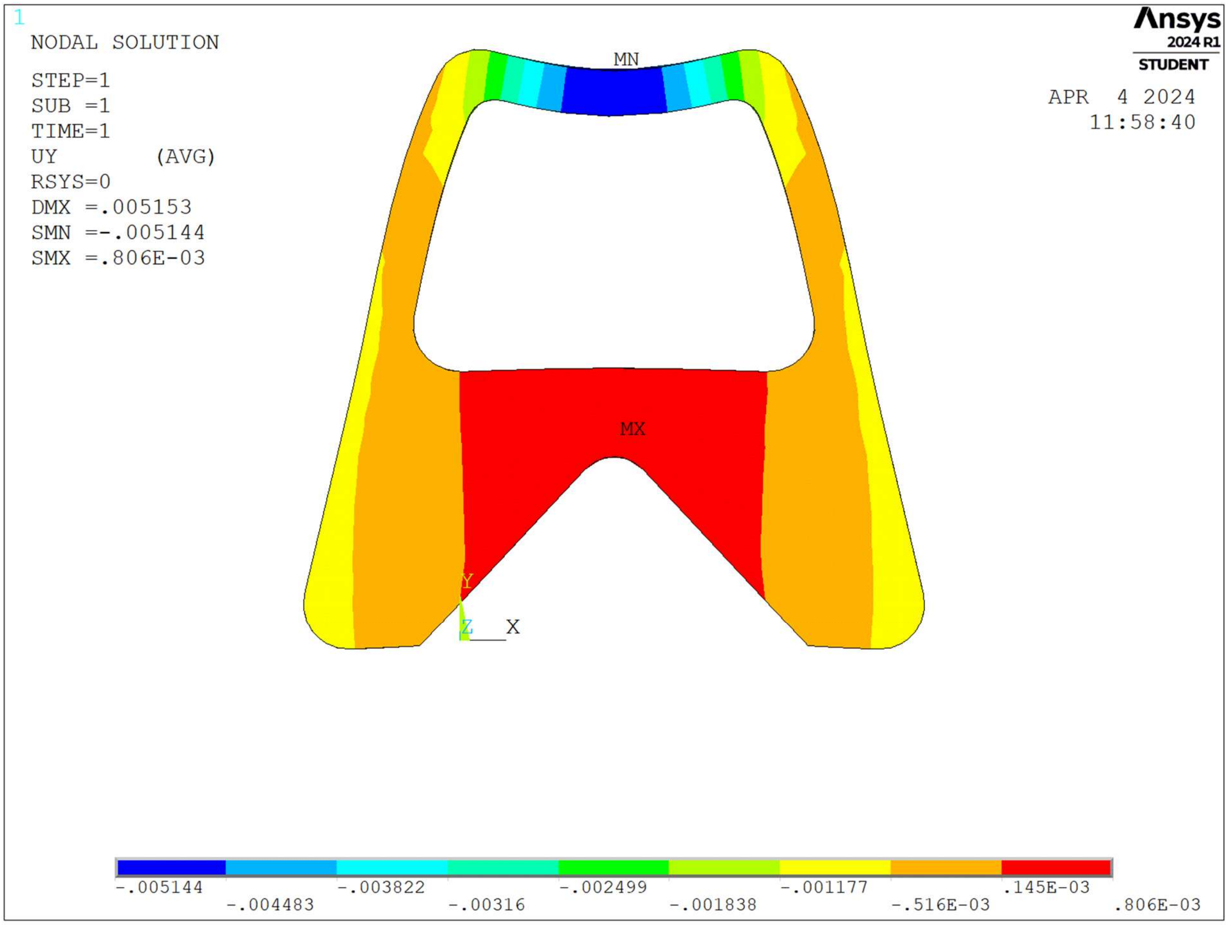

Figure 98: Contour plot of y-displacement in the ANSYS model of the block. Note that the values are signed and in inches. A negative y-displacement indicates movement downward. The largest displacement occurs in the thin top section.

Following the y displacement, the largest vector sum of displacement occurs at the same point, with the vast majority of this being the y component. The vector sum of displacement is plotted as a contour plot in *Figure 99* below. Once again, all the values in the figure are displacement in <u>inches</u>. The vector sum plot allows us to assess the displacement of the contact surfaces. From the plot the contact surfaces are displaced by 0.0314mm at the most. This is allowable as the foam can accommodate this extra movement, and because the consistency of the corrugated profile has been demonstrated to be variable even within the same section.

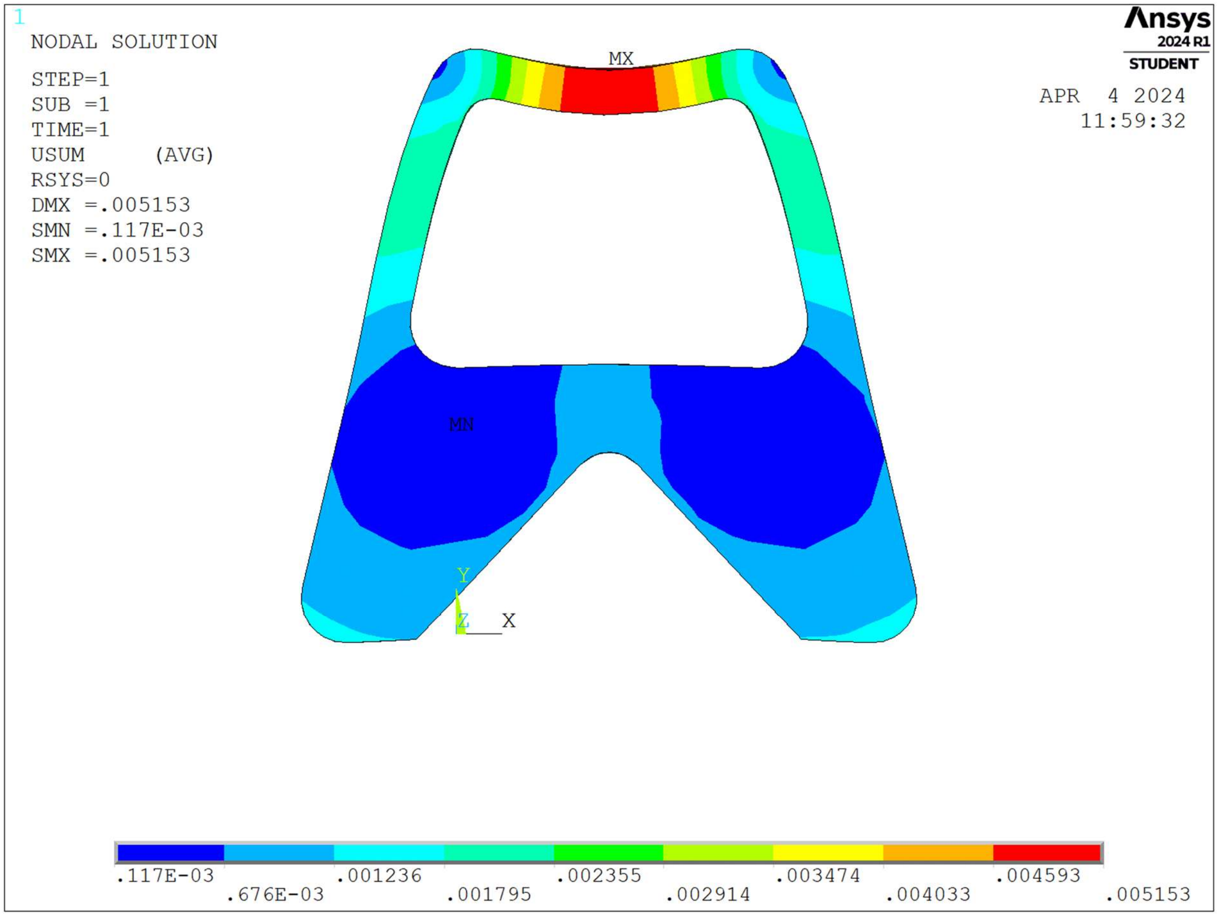

Figure 99: Contour plot of the vector sum of displacement magnitude in <u>inches</u>. Note that the angled contact surfaces displace by 0.0314mm, which is acceptable as the foam which is placed on these surfaces can expand and contract by more than this amount.

With these results from the finite element model, we have a level of confidence that the blocks will be more than sufficient for their design task. Summarizing the pertinent model results, the safety factor is 11.54, the maximum y displacement occurs at the load bearing thin section and is 0.1306mm downwards, and the angled contact surfaces displace by 0.0314mm. The values are tabulated in *Table 11* below. With this model and its results, we can validate with a simple real-world test, which is covered in the succeeding section of this report.

Table 11: Summary of key values from the Finite Element Model of the Spacer Blocks

Quantity	Value	Unit
Safety Factor	11.54	Unitless
Maximum y displacement	-0.1306	mm
Displacement of Contact Surfaces	0.0314	mm
Maximum von Mises Stress	2.45	MPa

Compression Test Procedure and Results

To validate the results of the model, we performed controlled testing on 3 samples machined from a sheet of the same HDPE as will be used in full scale production using the same manufacturing techniques and equipment as full-scale production. The testing was a simple compression test where the sample was placed onto a machined plate which is part of the testing machine, and a compression platen was installed onto the testing apparatus. The crosshead travelled at a constant velocity of 0.084673mm/s. A load cell then measured the applied force to the sample. The data collected was the crosshead displacement, the applied force, and the time, which was all sampled simultaneously at 10 Hz. *Figure 100* below shows the experiment setup.

Figure 100: Compression testing apparatus showing a spacer block with the crosshead in the starting position.

Below in *Figure 101* is a plot with the applied load in lbs. on the y-axis and the crosshead displacement in inches on the x-axis of a single sample. On the plot, the blue line represents the raw data from the test. The orange line is a linear extrapolation of data from a linear region of the material's response, which was extrapolated from the data points lying between 200lb and 400lb where the data appeared the most linear. This line represents the hypothetical case that the material was perfectly linearly elastic, which allows us to visualize and calculate when the elastic region of the material ends. This is helpful in determining when the material begins to yield. We chose this method for two reasons, firstly maximum load the block can withstand prior to yielding is what is of most relevance to the design of the spacer block, rather than the relationship between stress and strain. Second, the state of stress of the material is complex and not purely axial or flexural, therefore there is no obvious characteristic length with which to calculate the strain with as in equation 4.

$$\varepsilon = \frac{\Delta}{L_{char}} \tag{4}$$

Symbol	Quantity	Unit
ε	Strain	Unitless
Δ	Change in Characteristic Length	m
L_{char}	Characteristic Length	m

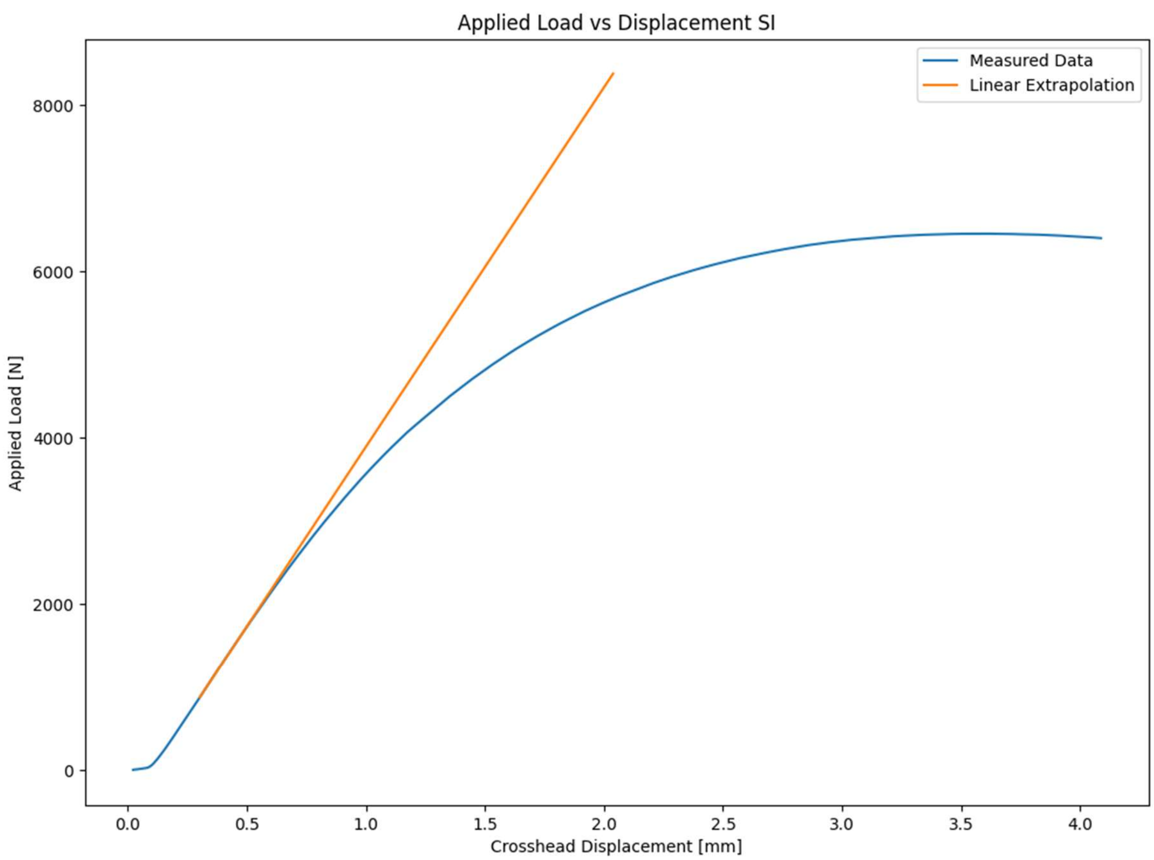

Figure 101: Plot of load supported by the spacer block test sample vs crosshead displacement. The blue line is directly measured data from the MTS machine. The orange line is a linear extrapolation of the most linear portion of the raw data, out to 2mm of crosshead displacement. Linear extrapolation is used

to aid us in determining the onset of yielding in the material. Notice that yielding begins between 2000N and 2400N, and the ultimate strength of 6450N.

From the plot we can qualitatively observe that there begins to be some noticeable deviation from the linear regime at a value between 2000N and 2400N, implying that the onset of yielding lies between these two values. We also see that the material continues to deform long past this point of yielding, which is characteristic of plastics above their glass transition temperature. The block continues to support load up until its ultimate strength of 6450N. Taking an average of the ultimate strengths of all three tested samples gives an ultimate strength of 6437.87N.

To aid in determining the onset of yielding, we follow equation 5 by subtracting the linearly extrapolated load value from the measured load value, then divide by the extrapolated value to get a non-dimensional difference. Then take the absolute value and multiply by 100 to provide a percentage. We do this for every data point up until a crosshead displacement of 0.08 inches. *Figure 102* below is a plot of this percent deviation vs the applied load at that point on the x-axis. From the plot we can see that the test samples load behavior deviates from the linear regime by more than 2% at 2260N. At this point we may consider that the material is at the onset of yielding. While only one sample is shown for clarity, the same behavior occurs in the other tested samples, and we assign a load rating of 2000N or 450lb to the blocks.

$$\delta = \left| \frac{(P_{observed} - P_{linear})}{P_{linear}} \right| * 100 \tag{5}$$

Symbol	Quantity	Units
$P_{observed}$	Observed Supported Load	lb.
P_{linear}	Hypothetical Supported Load if Material is Perfectly Elastic	lb.
δ	Percent Deviation from Linear Behavior	%

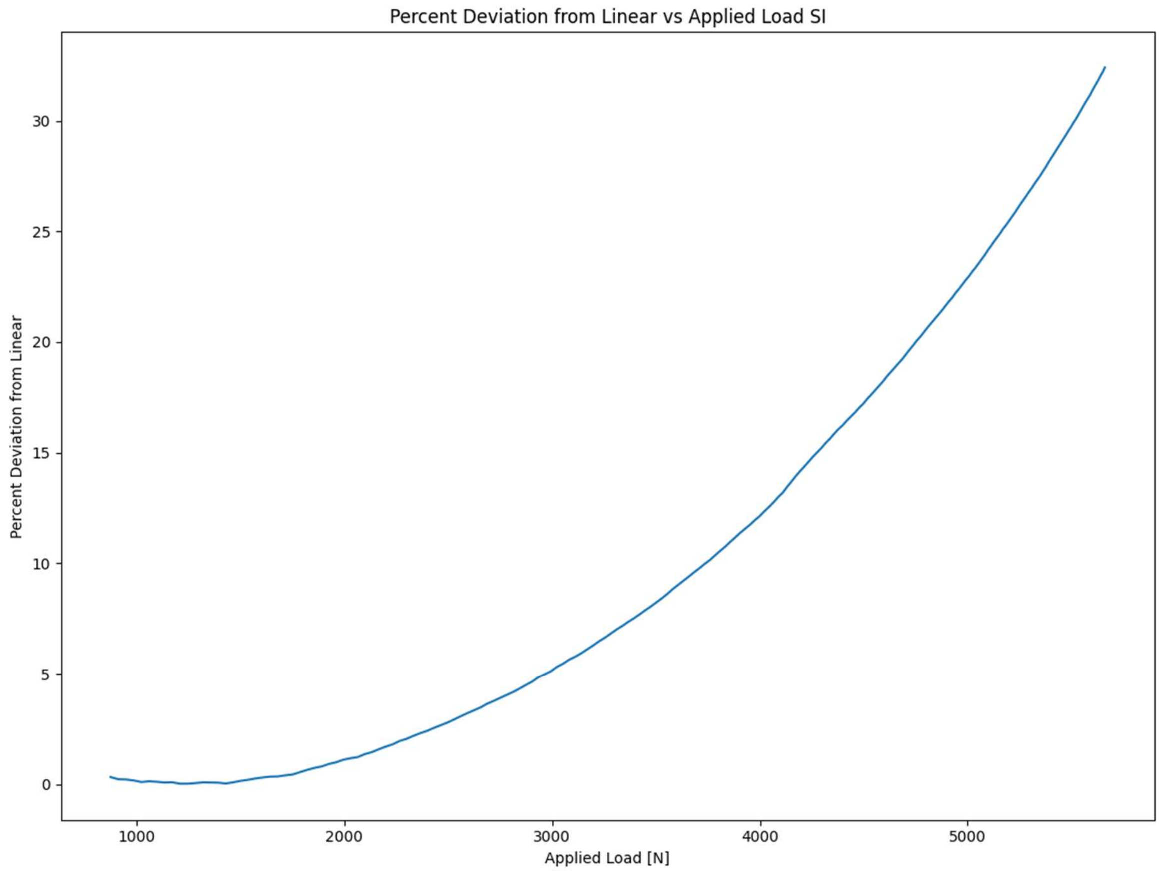

Figure 102: Plot of Percent Deviation from Linear Behavior vs applied load. Notice that 2% deviation occurs at 2260 N of force. We use 2% deviation as an approximation of the 0.02% offset rule that is common practice.

As mentioned earlier, the y displacement of the top surface is also of interest to ensure that the block meets its design function. Using the acquired data, we can find the displacement at approximately 172N. Averaging the crosshead displacement of the three samples at the nearest measured value to 172N provides a value of 0.135 mm.

Model Correlation with Observed Data

We can compare the values from simulation to observed values from the compression testing of our samples to validate the simulation and achieve a more complete understanding of the mechanics. Beginning with some qualitative observations, we see that the deformed shape of the object between the simulation and observation is nearly identical. *Figure 103* below is a comparison of the simulation output and an image of the spacer block near its ultimate strength.

Figure 103: The image to the left is an image taken of the spacer block prior to its ultimate strength. The image to right is an ANSYS simulation of the deformed shape with deformations scaled to be noticeable. Notice the agreement between the simulation and testing. This shows that the simulation has captured the relevant mechanics and geometry to accurately predict the behavior of the component.

Another indication that both the model and the test agree with one another is the deflections at 175N. From picking the data point nearest to this applied load and reading the crosshead displacement, we can measure the amount of y-deflection at the top surface. Doing this for all three test samples and averaging gives a y-displacement of 0.135mm for the tested samples. From *Figure 99* above, we see that ANSYS predicted a displacement of 0.1302mm. These two values are within less than 4% of each other.

Fatigue Loading and Reusability of the Spacer Blocks

While we have established that the spacer blocks meet the static loading conditions without yielding, which satisfies one part of the reuse, which is that they will be dimensionally stable. This section investigates the potential for fatigue failure due to the cyclic loading of the spacer blocks. We start by setting a target number of cycles for the component. As there are 80 CRP, the design number of cycles must be at least this. We choose 100 to provide some margin, and due to the ease of reading the stress value at this point on the S-N (also called a Wöhler) curve, as it would be represented as 10^2. To understand the fatigue behavior of HDPE we turn to scientific literature and specifically “Statistical analysis of HDPE fatigue lifetime” by Khelif, Chaoui, and Chateauneuf. The study used machined flat dog-bone samples and subjected them to a sinusoidal load at 5Hz of 600, 550, 500, 450, 400, and 300N depending on the sample, to achieve stress targets. The authors then took the results and applied various statistical models to generate the data and curves shown in *Figure 104* below. The two parameter Weibull curve is the most conservative, and we will compare our loads to this curve. Note that the 100 cycles point is not shown on the plot, so we will compare it with 1000 cycles. The two parameter Weibull curve predicts failure at a maximum internal stress of 21 MPa. From our ANSYS model our maximum internal stress is 2.45 MPa, or nearly an order of magnitude lower. In fact, the Weibull 2P curve predicts that failure would not occur even after a million cycles. Thus, fatigue is not a concern at the designed load conditions.

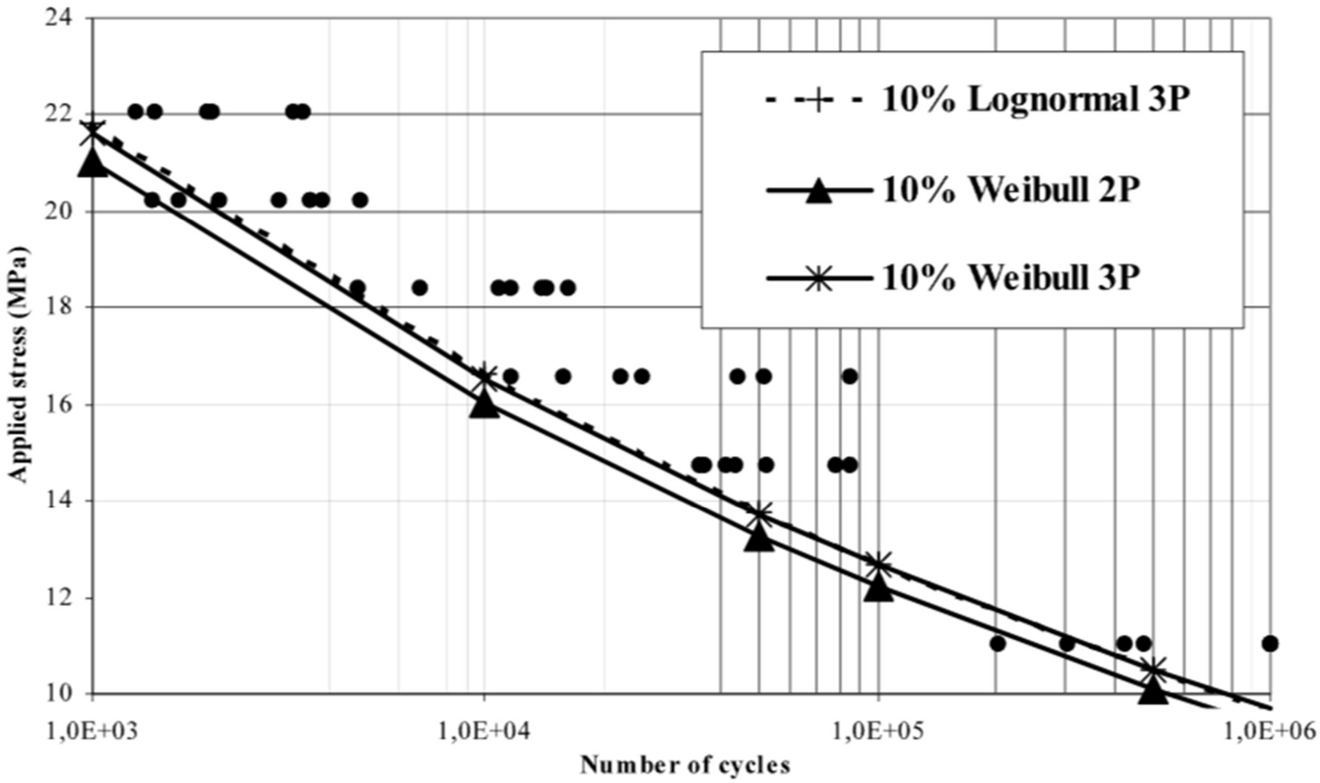

Figure 104: S-N curve of HDPE. Note the 2 Parameter Weibull fit is the most conservative, thus is the one used for comparison in this report. K. Chaoui and A. Chateauneuf, "Statistical analysis of HDPE fatigue lifetime," Meccanica, Jan. 2008, Accessed: Mar. 18, 2024. [Online]. Available: https://www.academia.edu/3220654/Statistical_analysis_of_HDPE_fatigue_lifetime

Gusset Plate Analysis

The gusset plates mounted to the truss support the mass of the truss while it rests on the cart. The gusset plates are made from 6.35mm thick 6061-T6 aluminum alloy. We analyzed the stresses and deformations of these plates to assess their performance. To do so a finite element model was created within ANSYS 2024R1. The material was modelled as a linear, elastic, and isotropic material with an elastic modulus of 68.95 GPa, yield stress of 275.79 MPa, and a Poisson's ratio of 0.33 as retrieved from the Matweb database. The SOLID 187 element type was chosen to mesh the model. To speed up computation the model took advantage of the half symmetry of the geometry. Nodes along the plane of symmetry were constrained to have zero displacements to enforce this condition. The resulting model had 17,534 nodes which comprised 8,319 elements. A summary of these parameters is in *Table 12* below.

Table 12: Summary of Gusset Plate FE Model Parameters

Quantity	Value	Unit
Elements	8,319	N/A
Nodes	17,534	N/A
Young's Modulus	68.95	GPa

Poisson's Ratio	0.33	Unitless
Yield Stress	275.79	MPa

The boundary conditions of the model are that the nodes along the plane of symmetry have zero displacement in any direction, which enforces the symmetry of the problem. The load was modelled as uniformly applied pressure over the area of contact between the gusset plates and the truss retrieval carts. The load supported by each gusset plate is one eighth the mass of the Installation Truss which we estimate as 12.5kg. This is then applied to an area of 241.935mm^2 which gives a pressure of 0.506MPa. The model was constructed using U.S customary units, therefore all values shown in the plots below are in units of inches and psi, which are equivalent to the SI values reported in the main body and tables of this report. See *Figure 105* below for a visual description of the model, with the mesh, loads, and boundary conditions shown graphically.

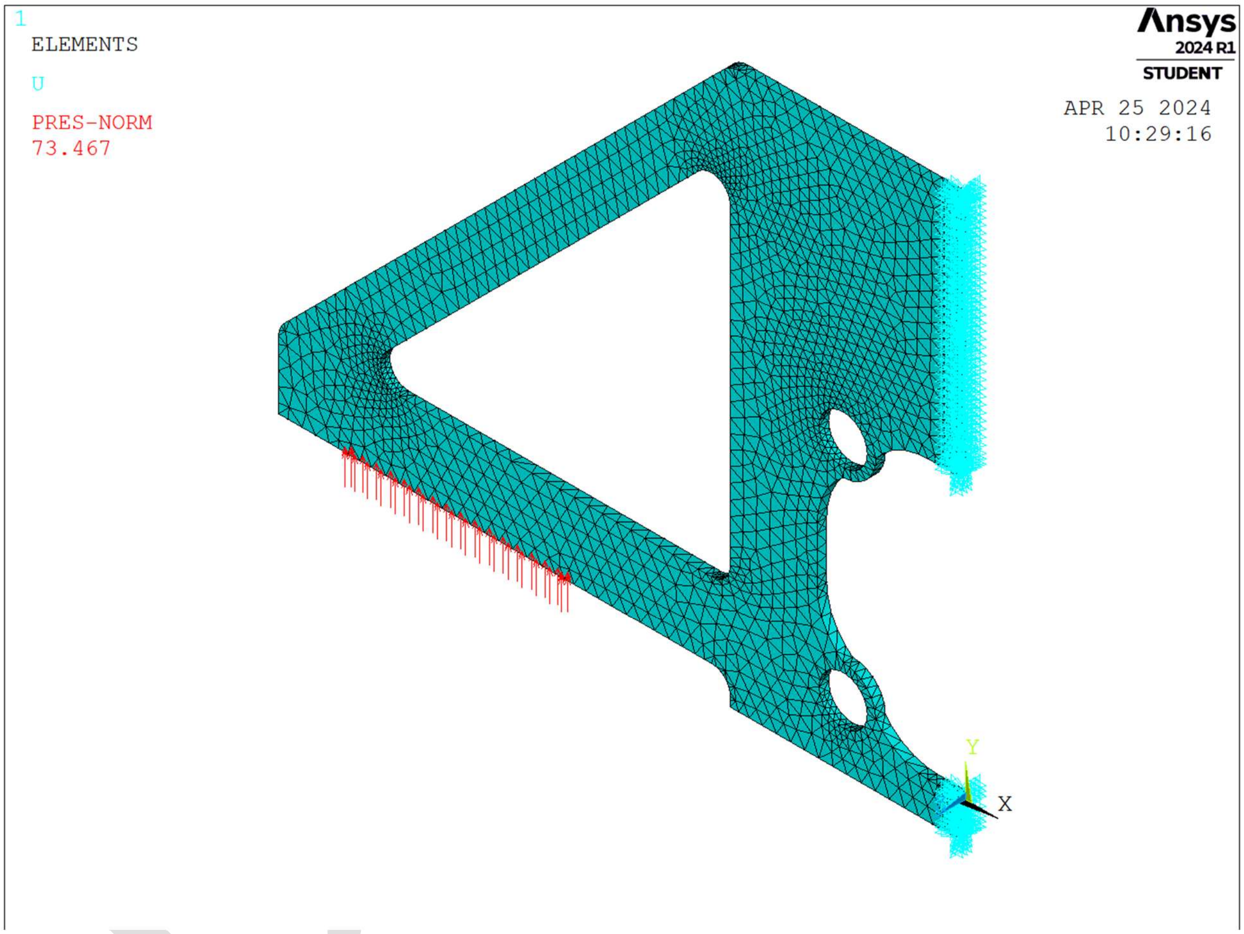

Figure 105: Plot of the Finite Element model including the mesh, loads, and boundary conditions.

Beginning with the stress analysis, we use the von Mises failure model, as we consider material yielding as failure, and the von Mises model accurately predicts yielding. The yield stress of 6061-T6 aluminum alloy at room temperature is 275.79 MPa, or 40,000 psi. The model predicts a maximum von Mises stress of 10.051 MPa or 1457.87 psi, as shown by *Figure 106*.This gives a safety factor against yielding of 27.43, which is much more than sufficient under the static design condition. This maximum stress occurs along the radius of the root of the arm which rests on the truss retrieval cart which makes sense. Another check that the model is reasonable is that the calculated reaction force is 122.544 N or 27.549lbf which is 0.0036% lower than the reaction forces predicted by hand. This is well within the tolerance of any valid numerical method.

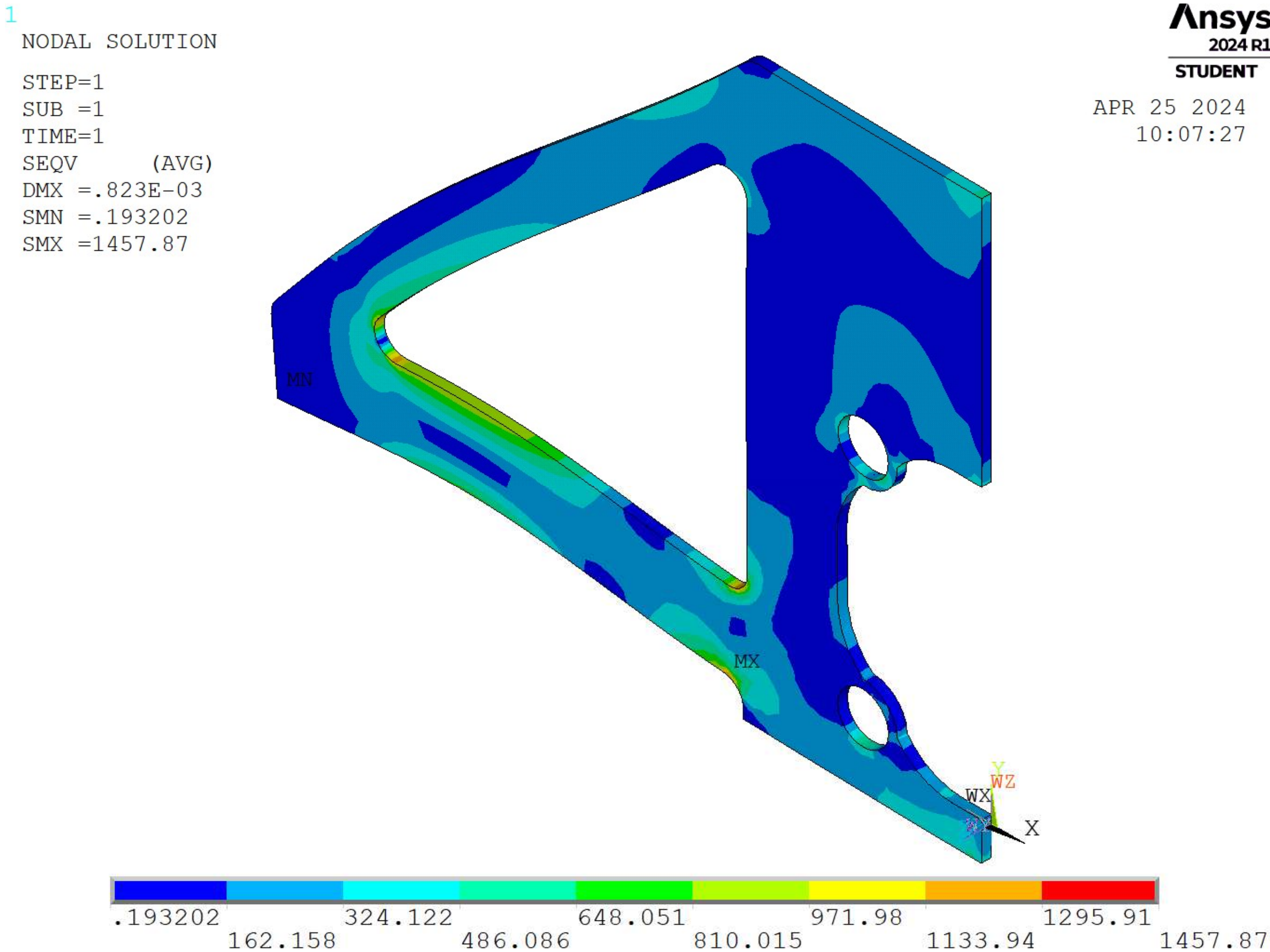

Figure 106: Plot of von Mises stresses within the gusset plate in U.S units. Note that the maximum is 10.05 MPa compared to the 275.9 MPa yield stress of the material at room temperature, therefore the safety factor is 27.43.

Next, we look at the displacement results of the FE model. Those of most interest are those displacements in the y-direction around the contact area. We want these displacements to be minimal so that there is a nice flat interface surface between the gusset plate and the truss retrieval carts. This reduces stress and is the condition in which this model is valid. Therefore, if the displacements are too large this model would be invalid, and a more complex analysis would be required. From the plot in *Figure 107*, the magnitude of the maximum displacement in y is 20.8 microns upwards, at the centroid of the contact area between the gusset plate and truss retrieval carts. This displacement is considered sufficiently small to make the uniform pressure distribution accurate.

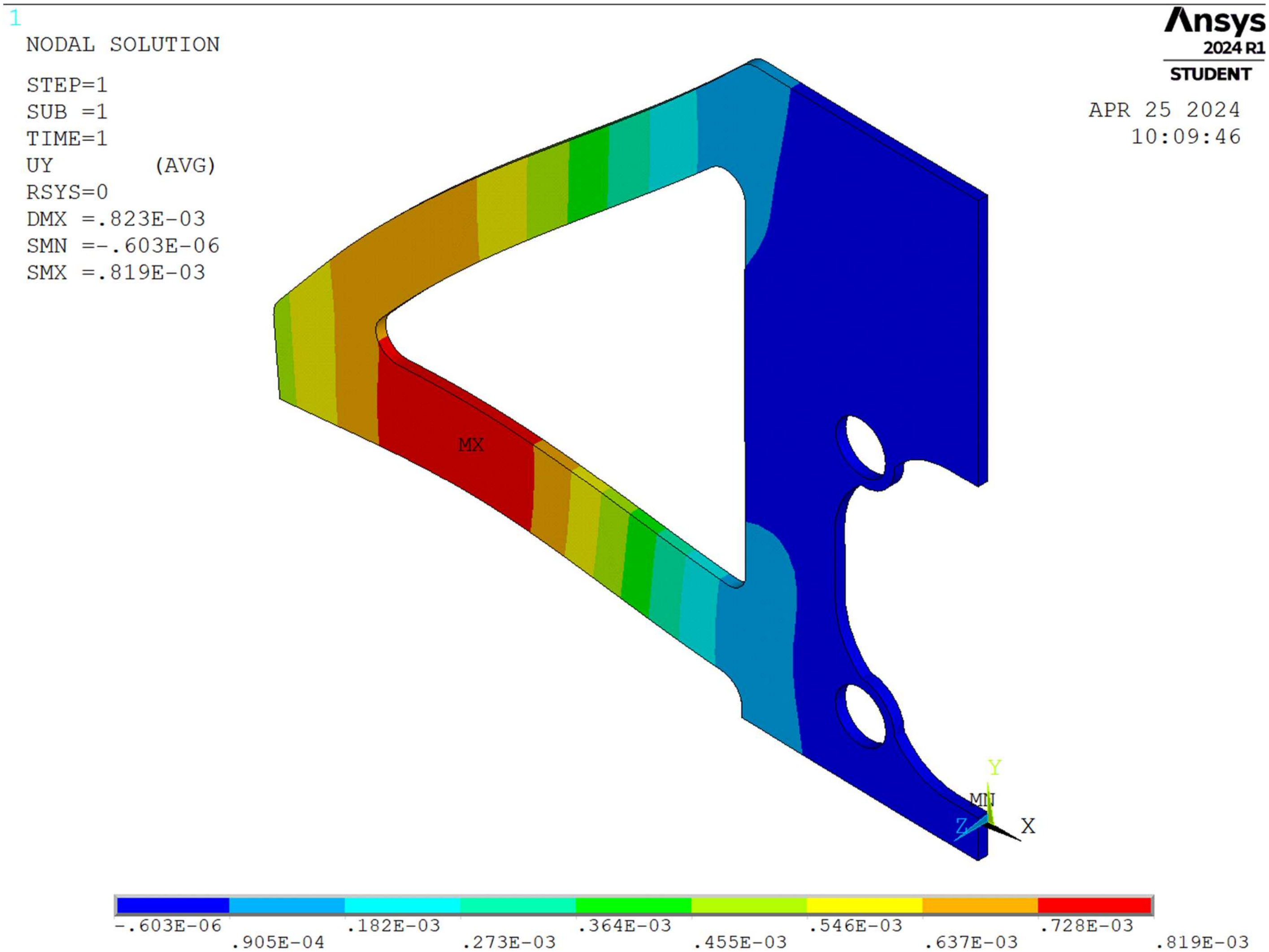

Figure 107: Plot of displacements in the y-direction of the gusset plate. Note the maximum above the centroid of the contact areas, and that its magnitude is 20.8 microns.

In summary the gusset plate design fulfils its design function, showing negligible displacements at the contact surface between the gusset plate and the truss retrieval carts. The value of this displacement is 20.8 microns. It does this without yielding and with a high safety factor of 27.43, with a maximum von Mises stress of 10.05 MPa. These results are summarized in *Table 13* below.

Table 13: Summary of results from FE analysis of the gusset plate.

Quantity	Value	Units
Maximum von Mises Stress	10.05	MPa
Yield Stress	275.9	MPa
Safety Factor	27.43	Unitless
Displacement of Contact Surface	20.8	micron

Truss Retrieval Cart Analysis

This section of the document analyses the truss retrieval carts structural components, being the aluminum frame, and the rotary shaft axle on which the wheels spin. The frame is a standard 6” x 3” x 0.1875” rectangular tube extrusion that is post machined to install axles and provide clearance for the wheels, the retaining hardware for the gusset plates, and hardware to link the carts together. The load that the carts will be subjected to is the same as the load placed on the gusset plate above, but in the opposite direction. This load is 0.506 MPa applied to an area of 241.935 mm^2, as we are modelling the entire geometry rather than a half-symmetry model, this load is applied to two areas which are equidistant to the centerline.

We begin by analyzing the aluminum cart frame to determine the stresses and deformations of the supporting frame. We do this to determine if a coupled model with the axle is necessary. If the deformations in the shaft hole are sufficiently small, a simple bending stress hand calculation would be sufficient to determine the stresses in the axle. If we find significant deformation from the cart frame model, we will perform a coupled contact analysis.

Beginning with the basic description of the model, we model the whole geometry as mentioned above. The model is free meshed using SOLID 187 elements, this results in a model with ___ elements corresponding to ___ nodes. The material was modelled using a simple linear elastic, isotropic model with a Young’s modulus of 68.96 GPa and a Poisson’s ratio of 0.33, which were selected based on 6061-T6 properties retrieved from Matweb. The model and material parameters are summarized in *Table 14*.

Table 14: Model and material parameters for the truss retrieval cart.

Quantity	Value	Unit
Elements		N/A
Nodes		N/A
Young’s Modulus	68.95	GPa
Poisson’s Ratio	0.33	Unitless
Yield Stress	275.79	MPa

The boundary conditions for the model are that the nodes lying on the x-axis are constrained to have zero x displacement, similarly the nodes on the z-axis are constrained to have zero z displacement. For the y-direction the top semicircle areas of the axle holes are constrained to have zero y-displacements, as this is where the axle will make contact under load. *Figure 108* below shows the model geometry, mesh, loads, and boundary conditions.

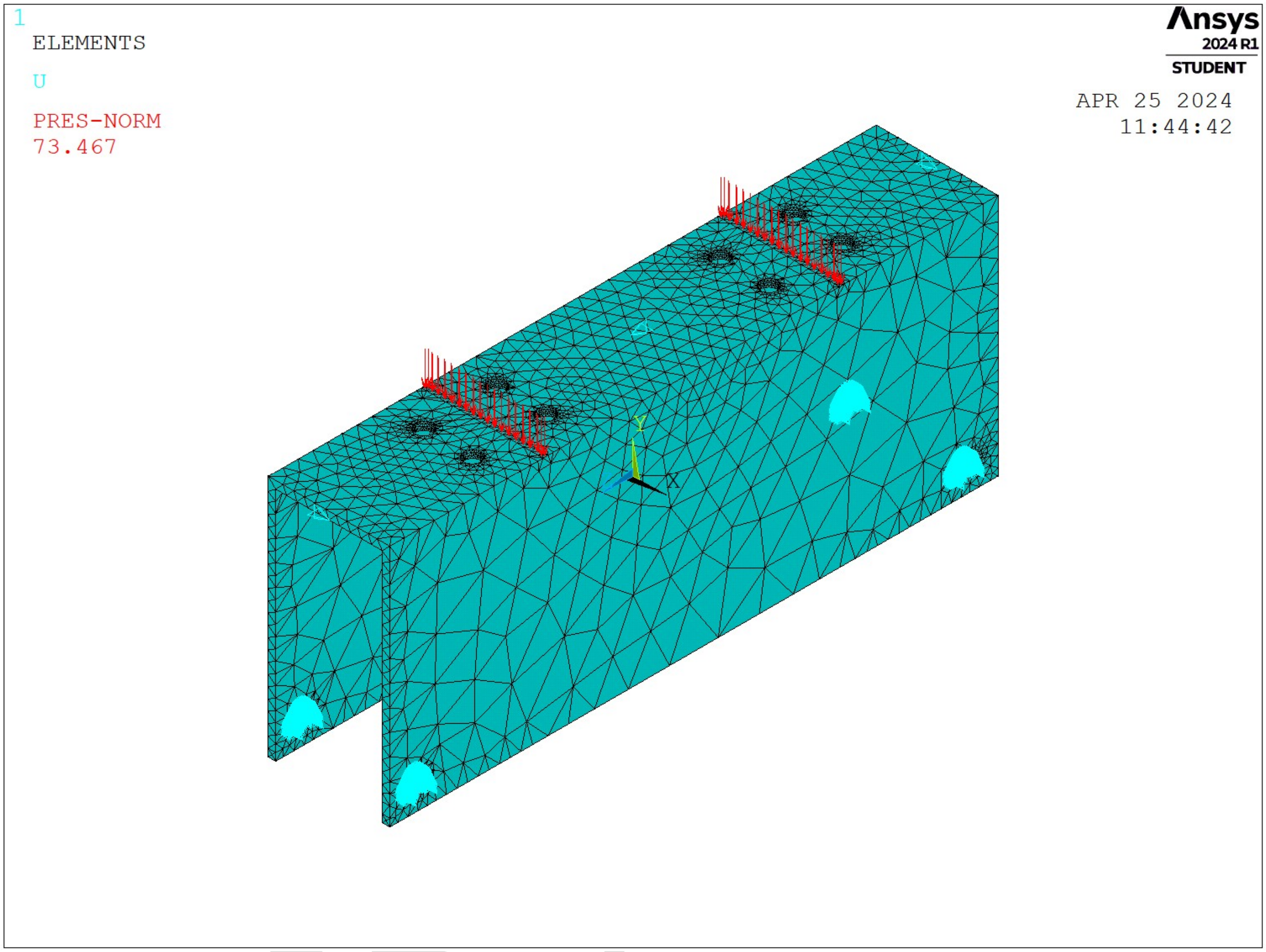

Figure 108: Truss retrieval cart model geometry, loading, boundary conditions, and mesh.

Beginning with the stress analysis of the cart, we see a maximum von Mises stress of 4.48 MPa (649.705 psi) at a point along the contact surface between the shaft and the cart frame. This makes sense and is well below the yield limit of 6061-T6 which is 275.79 MPa. This gives a safety factor of 61.57, however despite this high safety factor there is no way to reduce the cost of the system due to the height requirements of the system due to the false floor. Additionally, reducing the mass would significantly increase the time and cost of manufacturing the components as it would require more machining.

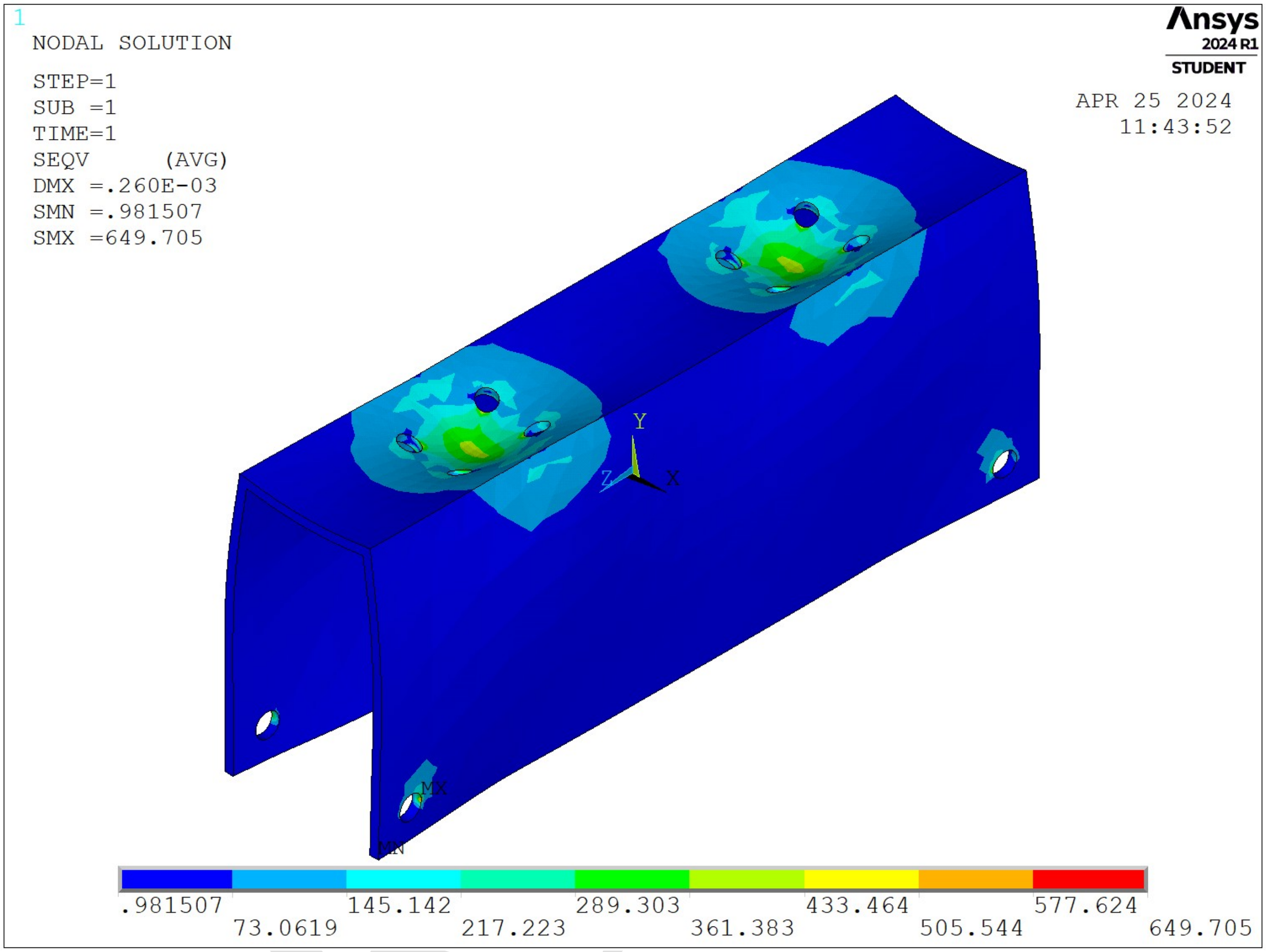

Figure 109: Plot of von Mises stresses within the truss retrieval carts. Note the maximum stress is 4.48 MPa at a location within the axle and cart contact surface. This is well below the yield limit of 275.79 MPa, with a safety factor of 61.57.

As the stress within the material is within acceptable limits, we move on to deformations. Remember that the deformations near the axle are of interest, as they determine the fit of the axle. If the deformations can be considered small, then we can treat the cart frame as a rigid load path, and then perform a simple bending stress hand calculation for the axle stress. The maximum displacement occurs at the centroid of the pressure loads, with a vector sum of displacement 6.604 microns. The vector sum plot is *Figure 110*. The vector sum of displacement near the axle is in the range of 1.5 to 2.25 micron. Looking at the specific directional displacements around the shaft holes we see that the displacement in each direction is on the same order of magnitude, which is less than 2.54 microns. Therefore, we can consider that the axle is rigidly supported at both ends.

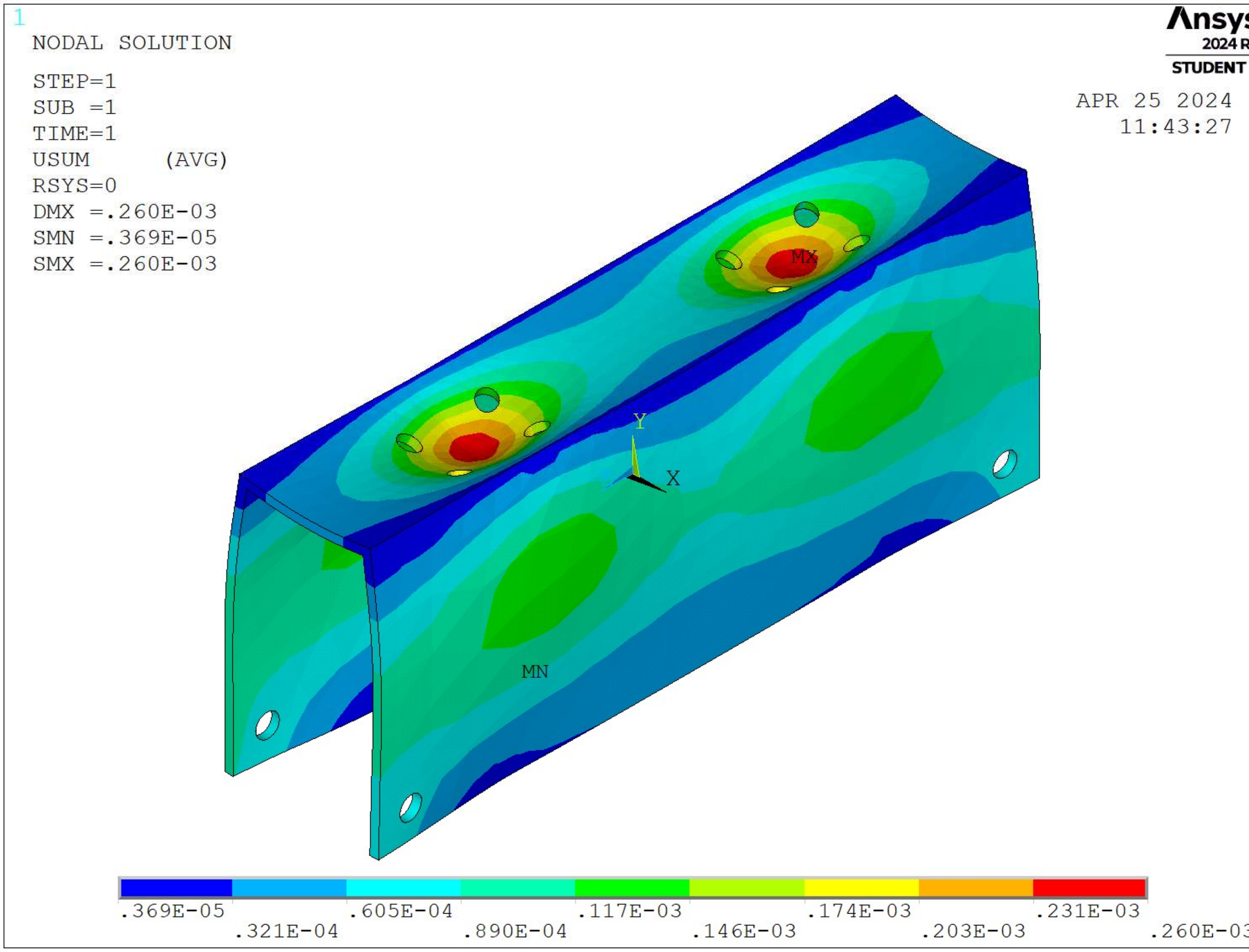

Figure 110: Plot of the vector sum of displacement of the truss retrieval carts. Note that the maximum occurs at the centroids of the applied pressure load, which is as we would expect. Also note that the deformation around the axle shafts is less than 2.5 microns. We can verify that this is true in all directions in the following figures which feature displacements in each direction individually.

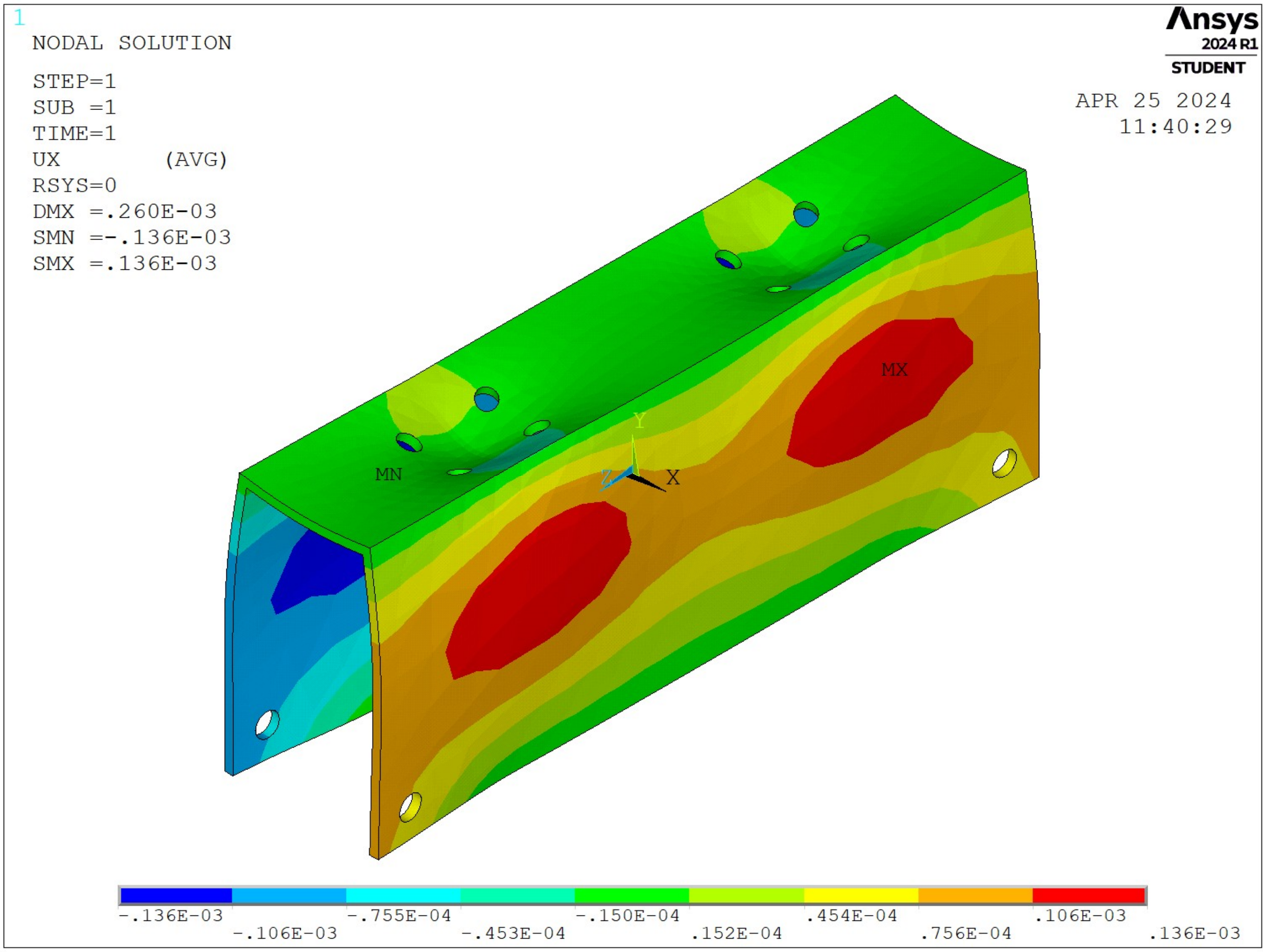

Figure 111: A plot of the x displacements of the nodes in the truss retrieval cart model. Notice that the displacement in the supporting axle geometry is smaller than 0.0001" or 2.54 microns.

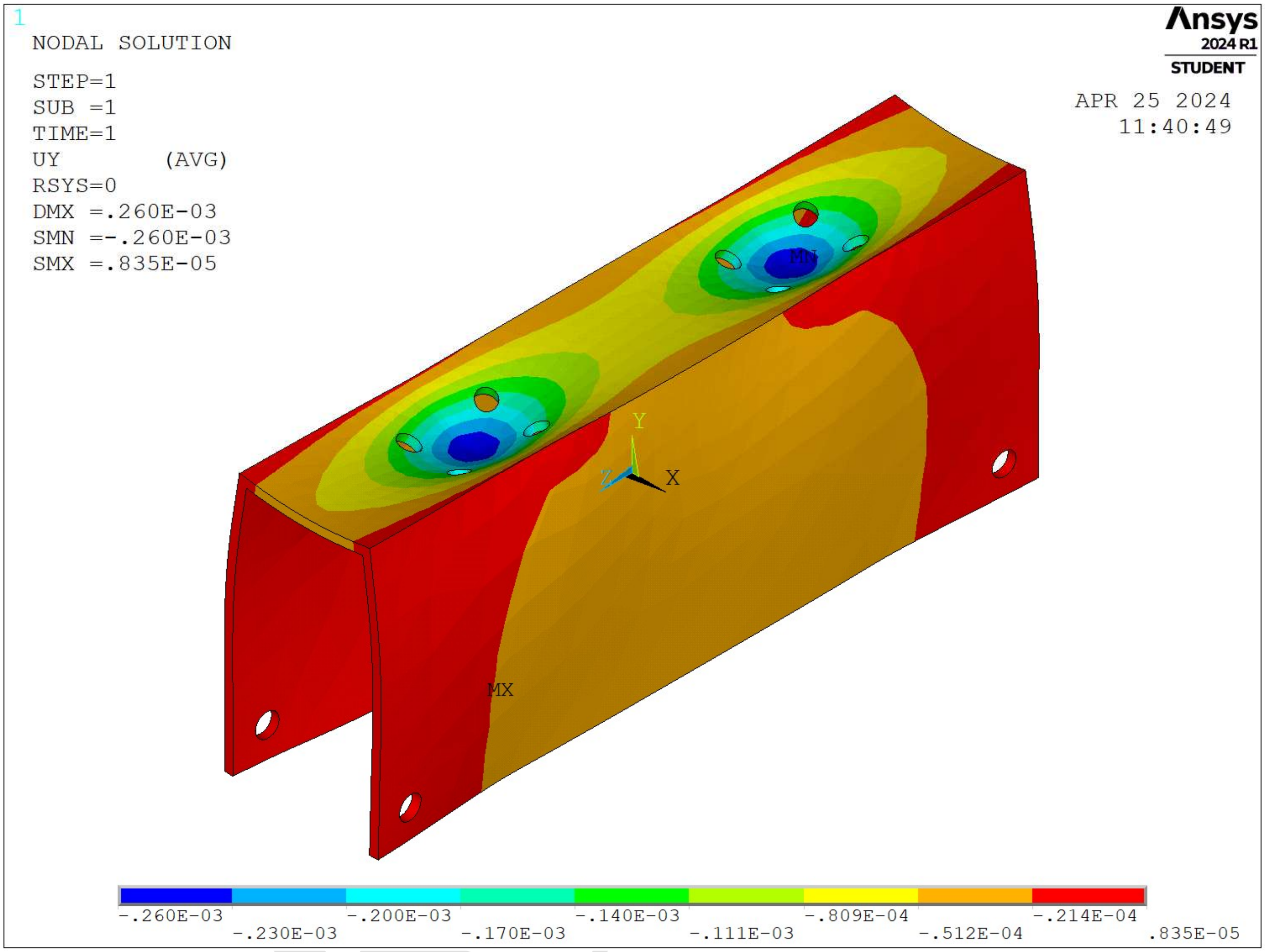

Figure 112: A plot of the nodal y displacements of the truss retrieval cart. Notice that the displacements of the nodes supporting the axles are less than 2.54 microns.

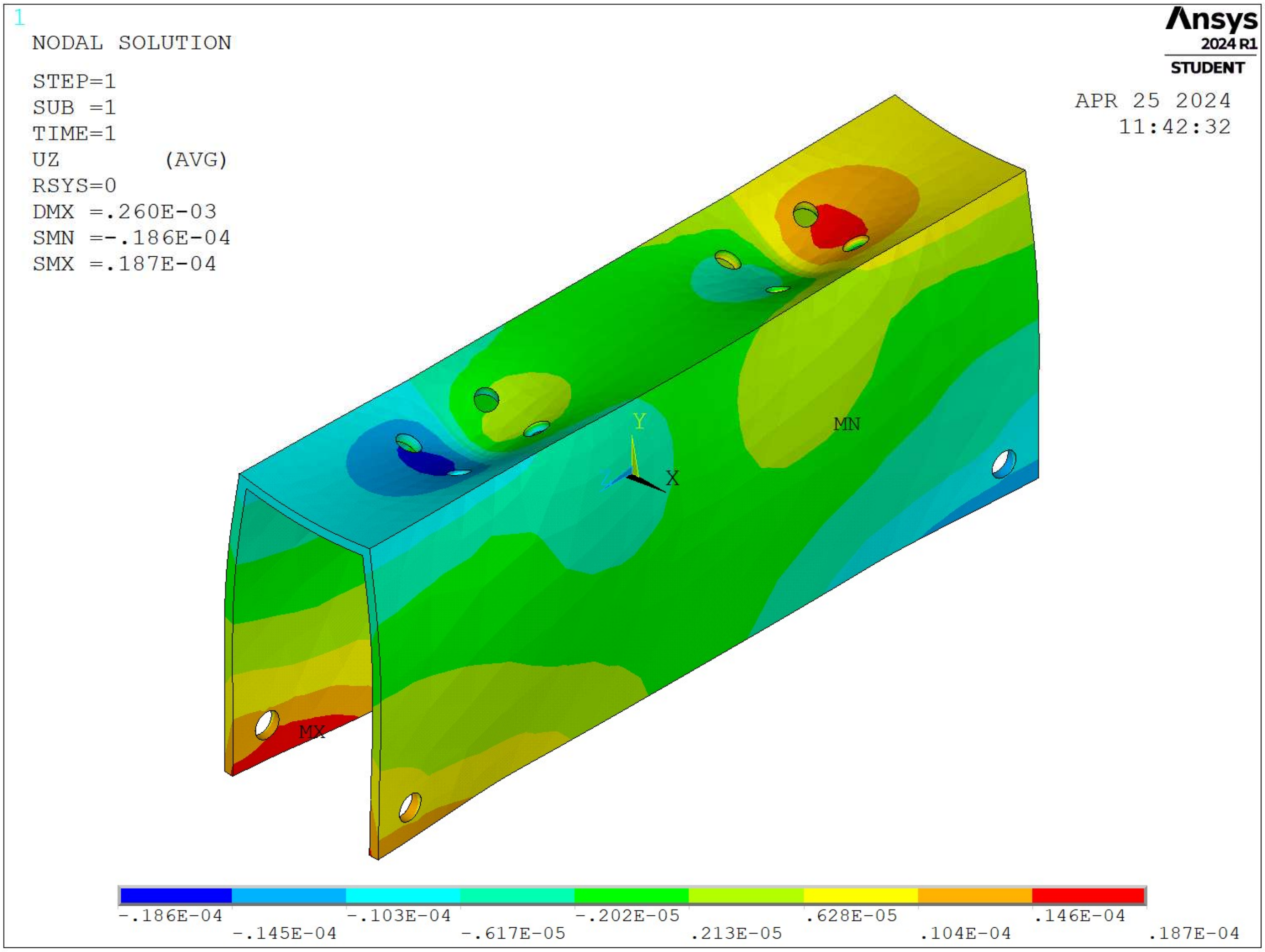

Figure 113: Plot of the nodal z displacements of the truss retrieval cart. Once again, the nodes that support the axle experience less than 2.54 microns of displacement.

As seen in the figures, the deformation of the cart near the shaft interfaces is negligible. Therefore, we can assume that the load path to axle is rigid, and the load transferred to the axle is the weight supported by the cart. Each cart supports one eighth the mass of the truss, and the axle is supported on two ends. We assume that exactly half of the force is applied to each supported end. *Figure 114* shows the free body diagram for this analysis with the coordinate system we define. We define the y-axis to be centered on the neutral axis of the shaft, that is line along the shaft where the shaft neither shortens nor lengthens. The analyzed element of the shaft is shown in red.

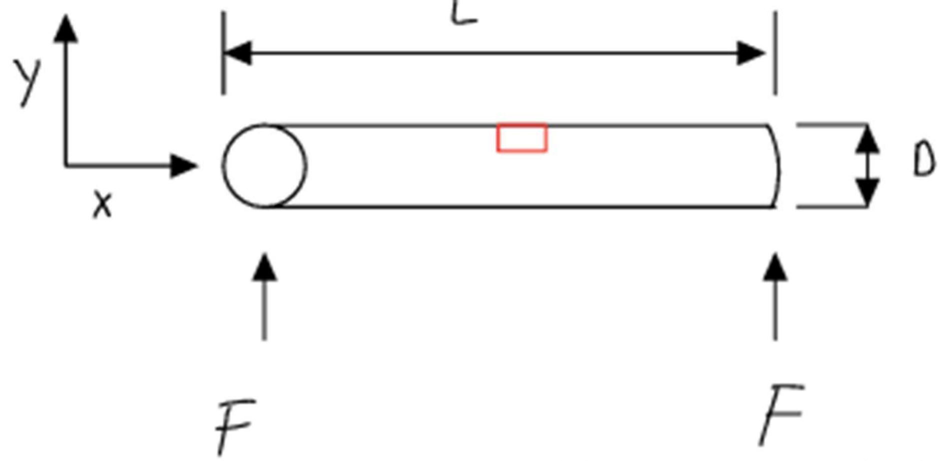

Figure 114: Free body diagram showing the element of the shaft being analyzed, the loading, relevant dimensions, and the coordinate system being used.

Knowing that the diameter of the axle is 12.7 mm, and the length of the axle is 76.2 mm, we can calculate the moment about the centerline of the shaft from each force. We then use the area moment of inertia, and the radius of the shaft to calculate the stresses following equation 6 below. Constituent equations are also shown below. As the forces placed on the shaft tend to bend the shaft in the same direction, the stress from each applied force adds together to describe the force along the centerline. Performing the calculations we find the maximum stress to be 15.48 MPa. As the shaft is made from case hardened AISI 1045, so we use values for yield stress from Matweb for quenched and tempered 1045 steel which is 842 MPa, giving a safety factor of 54.39.

$$\sigma_{bend} = -\frac{My}{I} \tag{6}$$

$$I = \frac{\pi D^4}{64} \tag{7}$$

$$y = \frac{D}{2} \tag{9}$$

$$M = F\frac{L}{2} \tag{10}$$

Symbol	Value	Units
σ_{bend}	Stress induced by Bending	Pa
I	Area moment of Inertia	m^4
y	Distance from the Neutral Axis	m
F	Applied Force	N
D	Shaft Diameter	m

References

[1]

"AISI 1045 Steel, Quenched and Tempered to 390 HB." Accessed: May 02, 2024. [Online]. Available: https://www.matweb.com/search/DataSheet.aspx?MatGUID=507031d65a684d96b1d6ee4d6d5d5cf3

[2]

King Plastic Corporation, "King-KPC-HDPE-Literature.pdf," King Plastic Corporation. Accessed: Feb. 20, 2024. [Online]. Available: https://www.kingplastic.com/wp-content/uploads/2014/05/King-KPC-HDPE-Literature.pdf

[3]

K. Chaoui and A. Chateauneuf, "Statistical analysis of HDPE fatigue lifetime," *Meccanica*, Jan. 2008, Accessed: Mar. 18, 2024. [Online]. Available: https://www.academia.edu/3220654/Statistical_analysis_of_HDPE_fatigue_lifetime

[4]

D20 Committee, "Specification for Polyethylene Plastics Extrusion Materials for Wire and Cable," ASTM International. doi: 10.1520/D1248-16.

[5]

D20 Committee, "Specification for Polyethylene Plastics Molding and Extrusion Materials," ASTM International. doi: 10.1520/D4976-12AR20.